Detection and Quantification of Damage from ASR Gels Using Multiphysical Nondestructive Evaluation

BY

Viet Le
Bachelor of Science in Civil and Environmental Engineering
University of Massachusetts Lowell (2015)

SUBMITTED IN PARTIAL FULFILLMENT OF THE REQUIREMENTS
FOR THE DEGREE OF MASTER OF SCIENCE
DEPARTMENT OF CIVIL AND ENVIRONMENTAL ENGINEERING
UNIVERSITY OF MASSACHUSETTS LOWELL

Signature of the Author ....
Department of Civil and Environmental Engineering
April, 2016

Signature of Thesis Supervisor ....
Associate Professor Tzuyang Yu
Department of Civil and Environmental Engineering

Committee Member Signature..
Professor Susan Faraji
Department of Civil and Environmental Engineering

Committee Member Signature..
Nathan Tregger
Grace Construction & Packaging (GCP) Applied Technologies Inc.

Detection and Quantification of Damage from ASR Gels Using Multiphysical Nondestructive Evaluation

BY

Viet Le
Bachelor of Science in Civil and Environmental Engineering
University of Massachusetts Lowell (2015)

ABSTRACT OF A THESIS SUBMITTED TO THE FACULTY OF THE
DEPARTMENT OF CIVIL AND ENVIRONMENTAL ENGINEERING
IN PARTIAL FULFILLMENT OF THE REQUIREMENTS
FOR THE DEGREE OF
MASTER OF SCIENCE
UNIVERSITY OF MASSACHUSETTS LOWELL
2016

Thesis Supervisor: Tzuyang Yu
Title: Associate Professor

Abstract

With its discovery in 1940, alkali-silica reaction (ASR) has been recognized as a debilitating plague to concrete structures. Due to the production of ASR gels that swell by imbibing water from the surroundings, an expansive pressure is exerted within a concrete or mortar matrix, resulting in damages such as map cracking, spalling, deformations, and reductions in mechanical strength. Unfortunately, structural health monitoring (SHM) of civil infrastructure for major issues like ASR require an immense amount of manpower far greater than the current supply of civil engineering professionals in today's society. However, a potential solution lies in the developments for nondestructive evaluation (NDE) of civil infrastructures which has proven to be an effective approach for collecting information on the condition of a material, a component, or a system. Changes in the material properties of a structure afflicted with ASR can be quickly and harmlessly determined by using noninvasive measurement technologies and in-depth analytic techniques.

In this study, mortar bars afflicted with ASR gels were differentiated from a control group through the use of multiple NDE sensors: a microwave imaging radar, an ultrasonic testing instrument, and an open-ended coaxial dielectric probe. The microwave imaging radar was utilized for synthetic aperture radar (SAR) imaging; whereas ultrasound pulse velocity and the probe were used for determination of mechanical and dielectric properties, respectively. Detection and quantification of the damages due ASR gels was carried out by observing the differences between mortar bars made from aggregates susceptible to ASR and a control group made from a nonreactive aggregate. In addition, the evolution of ASR with time and its effect on these sensors was studied. Through multiphysical nondestructive means, the study correlated the mechanical and electromagnetic in mortar bars with various levels of ASR swelling.

Acknowledgments

Foremost, I would like to express my utmost gratitude to my advisor, Professor Tzuyang Yu. His guidance and counsel were an invaluable component to the completion of my work and my transformation into a capable researcher. Without him, I would not be the person I am today. Besides my advisor, I would like to thank the rest of my thesis committee: Nathan Tregger from Grace Construction & Packaging (GCP) Applied Technologies Inc. (Cambridge, MA) and Professor Susan Faraji for their insightful comments. In addition, I greatly appreciate Nathan's assistance for providing two of the three aggregates used in the casting of cement mortar bars for this study.

My sincere thanks also go to my friends and fellow labmates: Jones Owusu Twumasi, Qixiang Tang, and Nicolas D'Amico. I am glad to have great companions accompany me through my research endeavors. In addition, I will always appreciate the assistance from Thet Myat Noe Sein, RenyYohana LendeMere, and Zixiang Huang for helping me conduct my experiments.

Last but not least, I would like to thank my mother, a shining gem in my life, for always showering me with love, my brother, my second half, for being my best friend in life, and my father, my motivation from above, for guiding me in all my endeavors.

Many thanks go to the United States Department of Energy (DOE) for their financial support through the Integrated University Program Fellowship.

Contents

List of Figures

List of Tables

Chapter 1

Introduction

The sustainability of civil infrastructures is constantly being undermined by various forms of deterioration. A lack of complete understanding of these ailments has impeded the use of many inspection and monitoring technologies on a practical level. Research on the deterioration of a infrastructures and systems like bridges, towers, and roads is essential to extending their service life. This knowledge, coupled with advancements in technologies for diagnosis of the potential sources of damages through nondestructive evaluation (NDE) techniques, can expedite the process of structural health monitoring (SHM) and maintenance of a structure.

One form of deterioration in concrete structures is alkali-silica reaction (ASR). Through the monumental work of Stanton in 1940, it has been recognized as a major cause of damage in concrete structures due to the production of gels that expand upon the absorption of water [9]. An example of the extensive damage caused by ASR gels is shown in Fig. 1-1.

These micro- and macro-cracks develop into severe damages such as spalling

(a) Exudation of ASR gels from cracks (b) Severe cracking of bridge column

Figure 1-1: Examples of damage caused by ASR gels [1].

and reductions in the strength of the concrete. Concern for ASR has even caught the attention of national entities in the U.S. In 2010, ASR was confirmed to be the cause of concrete degradation at a nuclear power plant in Seabrook, NH owned by NextEra Energy Resources [10]. Due to groundwater leakages into below grade structures and the reactive aggregate that was unknowingly used in the mix design for the concrete, ASR was able to occur and damage numerous locations around the power plant. Incidents involving the deterioration of concrete structures through this reaction have raised the concern for early prediction of the formation of ASR gels through NDE techniques.

Research conducted on ASR mostly pertains to the prediction of its effects and mechanisms, its detection and quantification, and its mitigation. These areas of study have contributed to the development of NDE techniques that civil engineering professionals can use to uncover vulnerable locations on a structure that have or will be plagued by the reaction, to quantify the potential effects due to ASR gel expansion, and to take the necessary steps to alleviate or prevent damages that have or will occur. By determining the properties of a material, component, or system in a non-invasive manner, NDE can be highly valuable in saving both time and money in the condition assessment of a concrete structure for damages from ASR gels and other forms of deterioration.

Emerging technologies using electromagnetic (EM) waves within the microwave frequency band in the field of NDE enable the distant and rapid damage detection on civil structures. EM sensors using synthetic aperture radar (SAR) imaging algorithms have been developed detection of damages on a test subject, sensing of subsurface objects, and identification of a specimen's material properties [11, 12, 13, 14]. Combining SAR imaging with other sensors like ultrasonic testing and dielectric measurement provide multiphysical and in-depth condition assessment of structures. For this reason, application of these techniques to the study of damage from ASR gels is a prime research opportunity to gain the upper hand in battling this form of deterioration in concrete structures.

1.1 Research Objective

ASR introduces additional components and changes to a cementitious composite that affect the measuring parameters of NDE techniques and make characterization of the damage from the gels within a specimen difficult. As a result, an in-depth understanding of the damages from ASR gels is needed. The primary contribution of this study is to provide multiphysical detection and quantification of the damage from the expansion of ASR gels that swell within a cement mortar bar using a continuous wave imaging radar, an ultrasonic pulse velocity test instrument, and an open-ended coaxial probe for dielectric measurement.

1.2 Thesis Approach

This study presents a methodology using a series of multiphysical NDE methods to detect and quantify damages in Portland cement mortar bars due to ASR gels. Three NDE methods are considered: a continuous wave imaging radar (CWIR), an ultrasonic pulse velocity test instrument, and an open-ended coaxial probe for dielectric measurement. ASTM C1260 "Standard Test Method for Potential Alkali Reactivity of Aggregates (Mortar-Bar Method)" was followed in the casting of mortar bars from three aggregates: two of which were reactive to ASR and one that was nonreactive to ASR. The feasibility of these measurements in detecting and quantifying the damages from ASR gels was investigated by analyzing the data from these tests. The multiphysical aspects of this study will provide further knowledge of the electromagnetic and mechanical effects of damage from ASR gels.

1.3 Organization of the Thesis

The organization of this thesis is as specified below.

Chapter 2 reviews the past work done on detecting and quantifying damage from ASR gels. A background of each of the three NDE methods used in this study is also provided.

Chapter 3 introduces the methodology for specimen preparation and the equipment for the NDE measurements conducted in this study.

Chapter 4 provides the resulting data from each NDE equipment used in the study and their interpretation for detection and quantification of damages from ASR gels.

Chapter 5 summarizes research findings and contributions. Suggestions are made for future endeavors in this research application.

Appendix provides additional figures that support the findings developed in this study.

Chapter 2

Literature Review

Alkali-silica reaction (ASR) is the most common of three kinds of alkali-aggregate reactions, the other two being alkali-carbonate reaction and alkali-silicate reaction. ASR is the result of a multi-stage chemical reaction between hydroxyl ions (OH^-) of the alkalis from hydraulic cement (Na^+, K^+)and reactive silica content (SiO_2) from aggregates such as opal and chert. The culmination of the various stages of ASR results in symptoms such as deformations and disturbances of internal stress in the afflicted concrete structure. The details behind the reaction's chemistry, which will not be covered in this thesis, have been heavily studied by others such as Chatterji [15] and Diamond *et al.* [16].

Three main components controlling the onset and degree of ASR are: alkalis (Na^+, K^+), reactive silica (SiO_2), and water (H_2O). Alkalis are basic, ionic salts of elements such as sodium and potassium that produce hydroxyl ions in solution. These hydroxyl ions initiate ASR through penetration of the concrete or mortar matrix which eventually leads to disruption of siloxane bridges. Portland cements typically have alkali contents between 0.3% and 1.3%. Alkali levels can be determined using Eq. (2.1) [17].

$$(Na_2O)_e = Na_2O + 0.658(K_2O) \tag{2.1}$$

where $(Na_2O)_e$ is equivalent sodium oxide, Na_2O is sodium oxide content and K_2O is potassium oxide content. Though the alkali content is predominantly present in cement, they can be supplied from external sources such as seawater, deicing salts, groundwater, and water from industrial processes. Reactive silica is the second component that controls ASR. Non-crystalline or amorphous forms of silica originate from the aggregates used in the concrete or mortar mix. Certain aggregates such as opal and chert yield greater amounts of reactive, non-crystalline silica which interact with the soluble alkali hydroxides to produce ASR gels. A multitude of factors such as chemical composition, level of crytalinity, and solubility of the silica in high-pH pore solutions govern the reactivity of an aggregate [18, 19]. One reason that knowledge of ASR is still limited is the difference in each aggregate's reaction in regards to cement hydration and the production of ASR gels. In addition, the varying material properties amongst each affects the resolution of NDE techniques. Lastly, water is the third component of ASR. Controlled by the water-to-cement (w/c) ratio, relative humidity (RH), and external sources, it provides mobility for the other two components to come together and cause ASR. Most importantly, it is the substance that ASR gels imbibe to swell within the concrete or mortar matrix, resulting in the damages associated with the reaction. Touma *et al.*, Fournier *et al.*, and Nilsson have extensively studied the effect of moisture on ASR [20, 21, 22]. A simplified visualization of the mechanism of the reaction and its resulting damages is shown in Fig. 2-1.

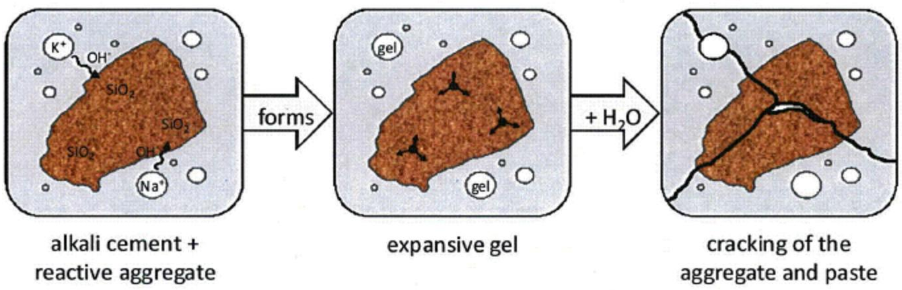

Figure 2-1: ASR Mechanism [2].

In general, these three components are in no particular order of importance. They are all needed at certain levels in order for ASR to occur, especially reactive silica content. Pessimum refers to the certain proportion of reactive siliceous aggregate needed to induce the most damaging scenario of ASR gel expansion. The amount of reactive silica content that yields the most expansion has been extensively studied in the literature [17, 23, 24]. The pessimum in a particular mix design must be avoided so that maximum expansion of the gels can be avoided.

2.1 Current Methods of Detection and Quantification of Damage from ASR Gels in Laboratory Specimens

With any means of inspection, a specimen to be examined is obviously a requirement. ASR-afflicted specimen can be obtained from concrete structures. However, this means of procurement for study of ASR is not effective due to the following reasons:

- Slow expansion rate of ASR which may take years to fully develop naturally
- Lack of control over mix design or curing/storage conditions of concrete structures
- Removal of samples damaging the concrete structure
- Potential coupling of other deterioration mechanisms such as freezing and thawing of water within the pores of concrete matrix an delayed ettringite formation (DEF)

As a result, many methods for accelerated manufacturing of ASR afflicted specimens in the laboratory have thus been created. These "recipes" allow researchers to cast a specimen damaged only by ASR gels within a few weeks or months, periods of time that are significantly shorter than the several years that natural means will require. In addition, researchers will have complete control curing conditions and mix designs of the cementitious composites. Two of the most common standard methods are ASTM C1260 "Standard Test Method for Potential Alkali Reactivity of Aggregates" and ASTM C1293 "Standard Test Method for Determination of Length Change of Concrete Due to Alkali-Silica Reaction" [8, 25]. Amongst the numerous laboratory methods of manufacturing ASR afflicted specimen, not one in particular is deemed perfect. The advantages and disadvantages due to time, cost, reliability, and severity of curing conditions vary from one to another. Nonetheless, researchers and professionals rely on these specimen manufactured in the laboratory in order to develop means to detect and quantify damage from ASR gel. At present, the use of acoustic waves and petrography are most dominant in this field. In this section, these methods used on laboratory specimens are discussed.

Petrography is frequently used for determining the presence of damages caused by ASR gels. It is not fully nondestructive because samples may need to be taken from a structure in order to be prepared for examination. These sections are examined for potentially ASR constituents or for quantification of cracks and reaction rims. ASTM C295 "Standard Guide for Petrographic Examination of Aggregates for Concrete" is the standard for petrographic examination of aggregates for concrete [26]. Researchers such as Rivard *et al.* and Sargolzahi *et al.* have utilized the Damage Rating Index (DRI) as a quantitative method of the internal deterioration caused by ASR [27, 28, 29]. With a microscope, an inspector focuses on an afflicted area and counts various symptoms of ASR such as aggregates with cracks, agggregates that have been debonded, and air voids lined with gels. Staining is also commonly used in conjunction with petrography. In the uranyl-acetate treatment procedure, reactive particles and ASR gels fluoresce with a bright yellow or green when the sample of concrete is sprayed with a solution of uranyl acetate and viewed under ultraviolet light [21]. On a smaller scale, high-resolution microscopic examination using laser scanning confocal microscopy (LSCM) and transmission soft X-ray microscopy have been reported [30, 31]. LSCM, in particular, has been capable of detecting damage from ASR gels in situ by producing 3D representations of ASR-afflicted specimens for nondestructive observation of defects like crack patterns, gel rings, reaction products, and debonding [31]. In the lab, these techniques provide the optical data needed to assess for ASR. However, certain restrictions such as the requirement of dry samples to prevent alteration of the specimen's composition from moisture limit the use of many of these microscopic techniques in the field.

Acoustic waves are also commonly used for detection and quantification of damage from ASR gels. For decades, techniques that have utilized such waves have been applied to determination of mechanical properties like modulus of elasticity, uniformity, strength, and durability [32, 33, 34, 35]. Conventional, linear acoustic parameters include pulse velocity and amplitude attenuation of compression waves through a material. Over the years, more sensitive methods utilizing nonlinear acoustic behaviors have been developed. These nonlinearities are exhibited in forms such as nonlinear cross modulation, higher harmonic generation, and resonance frequency shift [36]. In one example, Chen *et al.* evaluated the damages due to expansion of ASR gels in 25 x 25 x 285 mm mortar bars using the nonlinear effect of propagating ultrasonic waves. Their method, nonlinear wave modulation spectroscopy (NWMS), established a relationship between two defined acoustic energies and the buildup of damage from ASR gels [37]. Other nonlinear acoustic techniques are nonlinear impact resonance acoustic spectroscopy (NIRAS) developed by Leśnicki *et al.* and the time shift (TS) technique developed by Moradi-Marani *et al.* [38, 39].

As improvements are made with laboratory specimens, NDE for detection and quantification of concrete damage from ASR gels will eventually be widely adopted for in situ purposes. As of yet, no one technique has distinguished itself as the optimal, but innovative approaches continue advancing the technology further. The following sections 2.2, 2.3, and 2.4 will cover several NDE methods in depth, particularly, the ones utilized in this study. It is important to remember that mitigation and prevention of ASR is a necessary step after detection. Though not in the scope of this thesis, various measures taken to hinder and ameliorate ASR have been reported in the literature [40, 41, 42, 43, 44, 45, 46, 47].

2.2 Ultrasonic Testing

As mentioned in the previous section, many researchers have explored the abundance of acoustic methods for ASR detection. In particular, much study has been conducted on ultrasonic waves between 20 kHz and 25 MHz for NDE purposes. Here, the focus will be on ultrasonic testing of cementitious composites and the influence of damage from ASR gels.

The history of ultrasonic testing (UT) of concrete structures stretches as far back as the late 1940s [48, 49, 50]. The fundamental principle behind this approach to NDE is the measurement of wave attenuation and pulse velocity of compression waves within the ultrasound frequency range produced by an electro-acoustic transducer. As ultrasonic pulse travels through the thickness of a concrete specimen, it experiences multiple reflections at the boundaries and at the interfaces of material components. Subsequently, an assortment of body and surface waves are generated, and the travelling time of the pulse is measured. The introduction of open cracks from the swelling of ASR gels increases the travelling time path of these waves inside concrete. As a result, they lower ultrasonic pulse velocity (UPV) measurements and indicate signs of internal deterioration (higher UPV values above 3.5 km/s normally indicate a healthy concrete). The frequency of the transducers controls the size of the emitted ultrasonic waves, typically ranging from 20 kHz upwards to 25 MHz. Higher frequencies exhibit greater sensitivity to the detection of voids, cracks, or material defects but offer shorter penetration depths than those of the lower end. In the end, the measured parameters of UT are UPV and wave attenuation. These results are interpreted for mechanical properties such as modulus of elasticity, density, and compressive strength. In particular, pulse velocities of compression waves within the ultrasound frequency range are related to elastic properties and density in the following equation from ASTM C597 "Standard Test Method for Pulse Velocity Through Concrete" [5].

$$V = \sqrt{\frac{E(1-\mu)}{\rho(1+\mu)(1-2\mu)}} \tag{2.2}$$

UT is one of the most popular NDE methods to date and it has seen much use in attempts to detect and quantify damage from ASR gels. Hobbs showed a decreasing trend in the UPV of concrete as both acid soluble alkali content and expansion percentages increase over the course of two years [17]. Even with larger specimens, the effects of ASR gels lowered UPV. Through two years of monitoring, Swamy demonstrated how UPV values in ASR-afflicted reinforced concrete beams are lower and more varying than those of an intact, control concrete specimen [51]. In addition, both Hobbs' and Swamy's research works examined UPV trends in correlation to the properties of ASR-induced cracks (e.g. maximum crack widths and first signs of cracking) [17, 52]. Ahmed *et al.* were able to record the progression of ASR damage using UPV. They found that concrete specimen made from aggregates prone to the reaction could experience a stage of initial damage followed by a recovery stage due to hydration [3]. The UPV for ASR-reactive specimens decreased initially due to cracks from the swelling of ASR gels; however, they either, for a short period of time, stabilized or even increased as cement hydration products and additional gels strengthened the specimen by filling the pores or cracks. Fig. 2-2 shows this phenomenon.

Despite being one of the more trusted NDE techniques, UT is still being improved, especially for in situ use and for more complex analysis. Researchers such as Rivard and Saint-Pierre have attempted to correlate UPV of lab specimen to concrete cores taken from a 50-year old concrete structure known to have been damaged by ASR 20 years after construction [28]. Their study provided a sense of locations characterized by reductions in stiffness and compressive strength, albeit

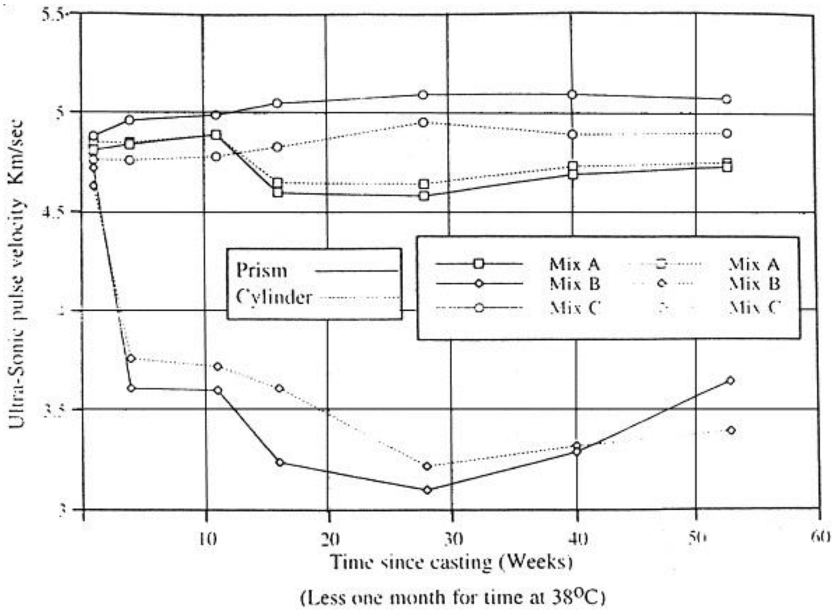

Figure 2-2: Variation of UPV of prisms (100 x 100 x 500 mm) and cylinders (150 x 300 mm) with time [3].

with a poor resolution since UPV varied from 3000 m/s to 5095 m/s while showing no consistent correlation with dynamic Young modulus which varied from 14.5 GPa to 36.4 GPa. Gong *et al.* expanded the analysis of UPV by using methods such as ultrasonic passband, attenuation spectrum, and stretching factor to detect and track ASR damage [35]. From these results, it is evident that UT is popular for the detection of damage from ASR gels.

2.3 Synthetic Aperture Radar Imaging

As an up and coming technology, electromagnetic (EM) methods within the microwave frequency range between 300 MHz to 30 GHz have been studied for NDE surface and subsurface sensing applications ranging from identification of material properties to detection of anomalies hidden inside a specimen [11, 12, 13, 14]. They have been applied in ground-penetrating radar (GPR), which uses a transmitting antenna to trigger radar signals (EM waves) and, typically, a second antenna to record their reflections from the material interfaces of the specimen [53]. These waves reflect off surfaces or attenuate as they pass through and around materials. The strength of these specular returns are governed by dielectric properties which, along with magnetic properties, are part of the electromagnetic properties of a material. Dielectric properties are determined by relative complex permittivity, ϵ_r^* which is comprised of a dielectric constant and a loss factor. Additional factors such as heterogeneous composition, defects, and geometries of a material may affect the strength of specular returns. Microwave imaging radars using synthetic aperture radar (SAR) algorithms also utilize reflection of radar signals. These SAR algorithms accommodate for the cumbersome size of large antennas. By using the motion of a small radar antenna around a specimen to mimic a larger antenna, images can be generated from the backscattered echos of transmitted radar signals that have longer wavelengths and that will not attenuate severely in lossy dielectrics. This study will explore the application of SAR imaging in detection and quantification of ASR gels and their effects on cementitious composite specimens. The novel use of this radar technology for this purpose has not been reported in literature.

In SAR imaging, several modes exist: spotlight, inverse, and stripmap [54, 55, 54]. A quick summary of the steps in deriving the SAR and backprojection algorithms is described as follows. Fig. 2-3 illustrates the monostatic radar operation of stripmap SAR imaging along a straight line flight path. The radar is located at $\bar{r}_s = (x_s, y_s, z_s)$ at a fixed height z_s and is moving at constant flight speed v. The incident wave is represented by a wave vector $\hat{k_i}$, the inclination angle with respect to the z axis is represented by θ_i, and the footprint domain is represented by G. Derivation of the time-independent SAR point response yields Eq. (2.3)

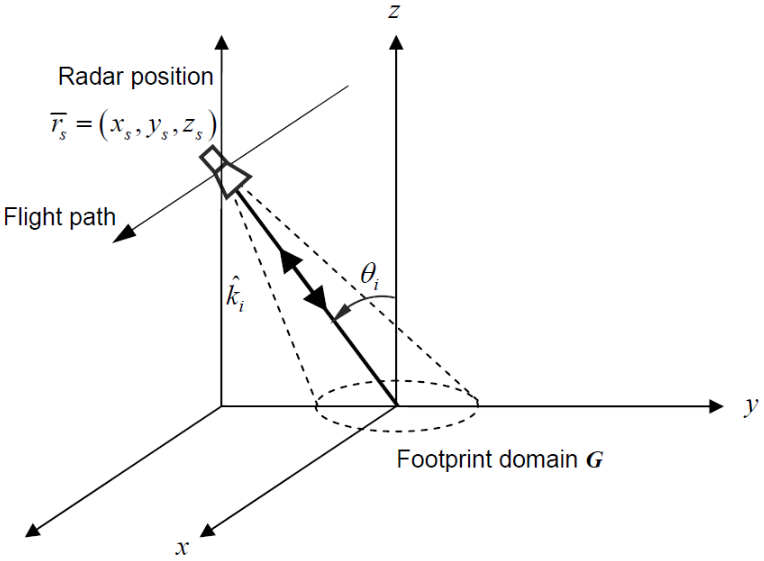

Figure 2-3: Stripmap synthetic aperture radar (SAR) travelling along a straight path aperture [4].

seen below [4]:

$$S(x, ysin\theta_i) = \text{sinc}\left(\frac{\pi ysin\theta_i}{\rho_r}\right)\text{sinc}\left(\frac{\pi x}{\rho_{xr}}\right) \tag{2.3}$$

where (x, y, z) are coordinates on the plane of radar inspection, ρ_r the range resolution of the radar (range is the distance from the radar system to the test subject), and ρ_{xr} the cross-range resolution of the radar (cross-range distance of the path of travel of the radar system). $\text{sinc}(x) = \dfrac{sin(x)}{x}$ is the sinc function. Rewriting the SAR point response in terms of time variable t and $\bar{r}_{s,j}$ results in the following:

$$S(\bar{r}_{s,j}, t) = \frac{1}{r_{s,j}^2} \int_{\omega_c - \pi B}^{\omega_c + \pi B} d\omega \cdot \exp\left[i\omega t\right] \tag{2.4}$$

where $\bar{r}_{s,j}$ is the difference between $\bar{r}_s - \bar{r}_j$, $\bar{r}_s$ the radar position vector, $\bar{r}_j$ the position vector of the j^{th} scatterer. $r_{s,j} = |\bar{r}_{s,j}|$ is the distance between the radar and the j^{th} scatterer, ω_c the radian center frequency, i the imaginary number, ω the radian frequency variable, and B the frequency bandwidth. The first step before deriving the backprojection algorithms involves integration and range compression on the SAR point response by shifting t to $\hat{t} = t - \frac{r_{s,j}}{c}$ where c is the speed of the radar signals. This shift allows the center of the reconstructed image to coincide with that of the scatterer. The backprojection processing is provided as follows in which $D(\xi, \hat{t})$ is the integration of all range-compressed focused radar signals at location ξ along the synthetic aperture and C_{BP} is the backprojection coefficient defined in order to yield an ideal bandpass transfer function.

$$B_{BP}\left(\xi, \hat{t}\right) = C_{BP} \cdot \frac{\partial D\left(\xi, \hat{t}\right)}{\partial \hat{t}} \tag{2.5}$$

The backprojected SAR image matrix, I, can be determined by:

$$I(\bar{r}, \phi) = \int_0^{r_s \theta_{int}} d\xi \cdot B_{BP}(\xi, \hat{t}) \tag{2.6}$$

where $(\bar{r}, \phi)$ are the polar coordinates of the SAR image on the range versus cross-range plane and $r_s\theta_{int}$ is the length of the synthetic aperture. $I(\bar{r}, \phi)$ is the two-dimensional, spatial image of the specimen. The elements of the SAR image matrix, I, are influenced by many factors affecting the strength of returned radar signals. Further theory and demonstration of the vast capabilities of SAR imaging in far-field airborne radar NDE and backprojection algorithms can be found in related literature [4, 13, 14, 56, 57].

2.4 Dielectric Property Measurement

In radar technologies, knowledge of dielectric properties (dielectric constant, loss factor) of a cementitious composite as a function of parameters such as density, water-to-cement ratio, sand-to-cement ratio, curing time, and aggregate size is essential to understanding its interaction with EM waves. The relative complex permittivity of a material has a significant role in the amount of reflection or attenuation of EM waves. Eq. (2.7) defines the complex permittivity ϵ^*.

$$\epsilon^* = \epsilon' - j\epsilon'' \tag{2.7}$$

where ϵ' is the real part, ϵ'' the imaginary part, and lastly, j the imaginary number ($\sqrt{-1}$). It is then divided by the electric permeability of free space ($\epsilon_0 = 8.854 \times 10^{-12}$ Farads/m) to yield relative complex permittivity, ϵ_r^*, shown in Eq. (2.8).

$$\epsilon_r^* = \epsilon_r' - j\epsilon_r'' \tag{2.8}$$

where ϵ_r' is the dielectric constant and ϵ_r'' is the loss factor. Knowing the dielectric properties can assist in characterizing the results of an output such as a SAR image or in simulating the response of EM wave propagation. For SAR imaging in particular, dielectric constant controls the magnitude of specular return of EM waves and their penetration, whereas loss factor determines the amount of EM wave absorption by the material. The study of the dielectric properties of cementitious composites will be focused in this brief review.

Dielectric property measurement and modeling for cementitious composites can be conducted through many means. Fig. 2-4 illustrates some examples of these methods and with the best situations for their usages in the dielectric property measurement of cementitious composites like concrete. One parameter that is of particular importance is moisture. The dielectric constant of water (78∼81) is much higher than those of cementitious composites (4∼20). Using a transmission line technique consisting of a vector network analyzer and an open-ended coaxial probe that measured the phase and amplitude of a reflected microwave signal within a wide frequency range from 0.1 to 20 GHz, Rhim and Büyüköztürk experimentally obtained the dielectric constants and loss factors of 28 day old concrete and mortar specimens with various moisture contents [58]. Their study showed an ascending trend in dielectric constant of a concrete specimen from an approximate range between 3.8 and 4 to an approximate range between 10.8 and 15 as moisture conditions change from oven-dried to wet with water on the surface. For a mortar specimen, the dielectric constant increased from an approximate range between 3.8 and 4 to an approximate range between 9.5 and 12.6.

Kharkovsky *et al.* conducted a similar study with a free space method utilizing a microwave oscillator with output power of 10 mW at X-band frequencies (8-12 GHz) and two horn antennas [59]. In addition, two water-to-cement, 0.4 and 0.7, were used in the mix design of a mortar specimen. Over the course of three months, they demonstrated that dielectric constant of the mortar specimen with water-to-cement ratio of 0.4 was approximately 8.9 as compared to 7.25 for the specimen with water-to-cement ratio of 0.7. The loss factor decreased from an approximate range between 0.54 and 0.63 for the specimen with water-to-cement ratio of 0.4 to an approximate range between 0.26 and 0.34 for the specimen with water-to-cement ratio of 0.7. These differences were due to the change in the dessication of water and in internal structures and densities from the two water-to-cement ratios. Similar investigations on the effects of moisture on cementitious

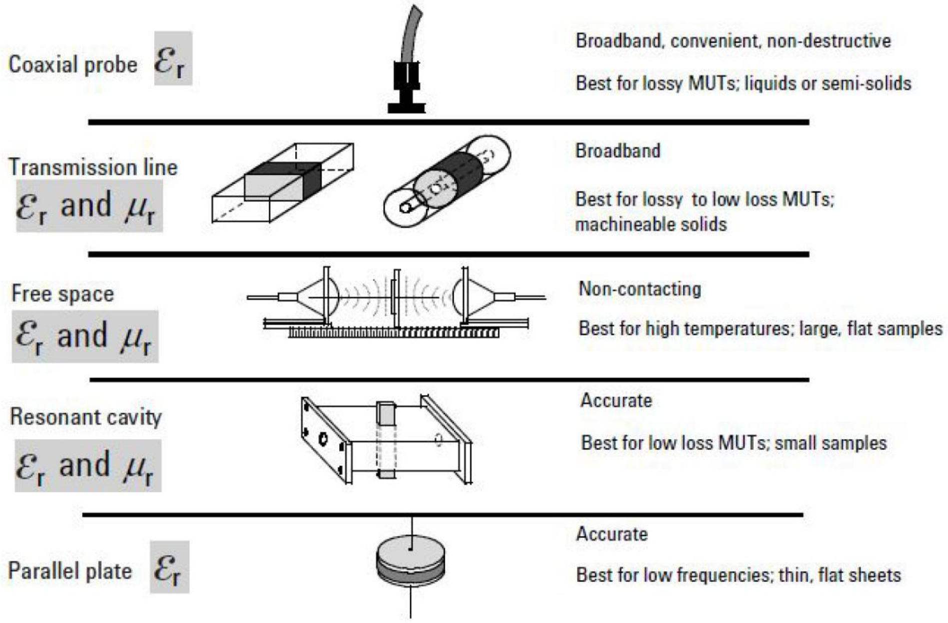

Figure 2-4: Various methods for dielectric property measurement (Source: Agilent® Technologies Inc.)

composite have been conducted [60, 61, 6, 62, 63]. These studies not only focused on obtaining experimental data but also on developing predictive models for dielectric properties with respect to parameters such as measurement frequency or moisture content. One that has been commonly used and modified is Debye's model of complex electric permittivity. Debye's frequency-dependent models for the real part (ϵ_r') and the imaginary part (ϵ_r'') of the relative complex permittivity is denoted below [64].

$$\epsilon_r'(\omega) = \epsilon_\infty + \frac{\epsilon_s - \epsilon_\infty}{1 + (\omega\tau)^2} \tag{2.9}$$

$$\epsilon_r''(\omega) = \frac{\omega\tau(\epsilon_s - \epsilon_\infty)}{1 + (\omega\tau)^2} \tag{2.10}$$

where ω is the angular frequency (rad/s) of the applied, alternating, external electric field, τ the characteristic relaxation time (s), ϵ_∞ the infinite permittivity (F/m) measured by the alternating current at frequency $\omega = \infty$ (infinite frequency), and ϵ_s the static permittivity (F/m) measured by the direct current field at frequency $\omega = 0$ (static frequency). The model assumes a homogeneous composition for the material and single polarization of molecules that does not change with temperature. In addition, it is best used for liquids and gases, in particular, dilute solutions. Nonetheless, its application has been extended to solid materials. Shown in Eq. (2.11) and Eq. (2.12), Twumasi and Yu used a modified version of this model for prediction of the dielectric constant and loss factor of oven-dried cement paste specimens in the frequency range of 1.02 GHz and 4.50 GHz [63].

$$\epsilon_r'(\omega) = \epsilon_\infty + \frac{\epsilon_s - \epsilon_\infty}{1 + (\omega\tau)^2} - \frac{\psi}{10} \tag{2.11}$$

$$\epsilon_r''(\omega) = \frac{\omega\tau(\epsilon_s - \epsilon_\infty)}{1 + (\omega\tau)^2 - C_2} - C_1 \tag{2.12}$$

where ψ is water-to-cement ratio and C_1 and C_2 are experimental constants determined by nonlinear best fitting. Other models have been reported through literature, some of which intricately incorporate the heterogeneous properties of cementitious composites. These dielectric mixing models will not be explored in this study.

For detection of damage from ASR gels in cementitious composites, studies using microwave technologies are relatively few. Donnell *et al.* demonstrated the detection of damage from ASR gels using a waveguide measurement technique in the S-band frequency range from 2.60 to 3.95 GHz [65]. Cement mortar specimens of dimensions 7.21 x 3.4 x 10 cm were cast from two different aggregates, one reactive to ASR and the other nonreactive. Measurements of the reflection and transmission coefficients indicated, with respect to time, the different rates of change in dielectric properties between the reactive and the non-reactive specimen. Through various cycles of drying and exposure to humid conditions, the dielectric constant and loss factor for the cement mortar specimens afflicted with ASR changed at a slower rate. The dielectric constant of the nonreactive specimen exhibited a maximum temporal change of ± 1, while the dielectric constant of the reactive specimen varied by a maximum of only ± 0.5. A similar pattern was likewise found for the loss factor. The loss factor of the nonreactive specimen changed by ± 0.8 but the maximum difference in loss factor of the reactive specimen was only ± 0.4. This was attributed to the lower rates of evaporation of free water from the pores due to absorption by ASR gels. In addition, at the same frequencies, the dieletric constant of the reactive specimen were lower than that of the nonreactive by almost 2 for each measurement ($\sim$9 as compared to $\sim$11). Physical mechanisms such as free water filling pores and cracks and chemical mechanisms such as the transformation of free water to bound water were proposed as reasons for this difference. Measurements with R-band (1.70-2.60 GHz) and X-band (8.2-12.4 GHz) frequencies, in combination with the S-band, were also investigated by Donnell *et al.* and Hashemi *et al.* [66, 67]. Their results indicated that measurements with the lower R-band and S-band frequencies would be more sensitive than those with the higher X-band frequency to changes in dielectric constant and loss factor due to damage from ASR gels and shifts in the ionic concentrations of the pore solution. Reactive and nonreactive cement mortar specimens showed twice as much temporal change in both dielectric properties when measured with the S-band frequency than the X-band frequency. Despite their work in wideband characterization of ASR gels in cement mortar specimens, Donnell *et al.* and Hashemi *et al.* did not investigate the use of measurement frequencies below 1.70 GHz. In addition, dielectric measurement of ASR gels outside the cement mortar matrix was not conducted. This would be helpful in dielectric mixing models in order to characterize the effect of ASR gels and absorption of free water. Further studies must be conducted in order to properly utilize microwaves in detection and quantification of damage from ASR gels. More detailed understanding of the various mechanisms that work together to influence electromagnetic properties of cementitious composites damaged from ASR gels is definitely needed.

2.5 Summary and Further Comments

NDE technologies for damage detection of civil infrastructure are essential to SHM. They are especially important for detection and quantification of deterioration mechanisms in concrete structures (e.g. ASR). Ultrasonic testing and microwave NDE methods are covered in the literature review of this chapter.

Several other important research areas pertaining to ASR are not covered in the scope of this literature review. As mentioned previously, mitigation or prevention of ASR gel expansion is a major research topic. In addition, models of the chemical reaction mechanisms, of ASR gel expansion, and of the deterioration of the cementitious composites have been extensively studied [68, 69, 70, 71]. These allow researchers to simulate and study various aspects of ASR the prediction of the pessimum expansion, stress fields due to cracking of concrete structures, and the reaction kinetics. Swelling of ASR gels in combination with other forms of damages such as cyclic freezing and thawing of water within the pores of a concrete matrix and delayed ettringite formation (DEF) has also been investigated [72, 73].

Chapter 3

Specimen Preparation and Experiment Methodology

As mentioned previously, accelerated production of ASR-afflicted specimen is a necessary component for NDE research on the reaction. Several methods, some of which are modified versions of others, are available to use. In this study, ASTM C1260 "Standard Test Method for Potential Alkali Reactivity of Aggregates (Mortar-Bar Method)" is used to determine aggregate reactivity and to manufacture ASR-afflicted mortar bars.

Multiphysical inspection of ASR-afflicted and control mortar bars is proposed through three nondestructive means: a continuous wave imaging radar (CWIR) with a center frequency of 10 GHz and a bandwidth of 1.5 GHz for SAR imaging, a Proceq Pundit® Lab ultrasonic pulse velocity measurement sensor, and an Agilent® 85070E Performance Coaxial Probe along with an Agilent® E5071C ENA Series Network Analyzer for dielectric measurements. Following the tests, data interpretation and fusion was conducted in order to differentiate the EM and mechanical properties of mortar bars reactive to ASR from those of the mortar bars nonreactive to ASR. Fig. 3-1 shows a short summary of the step-by-step research procedures.

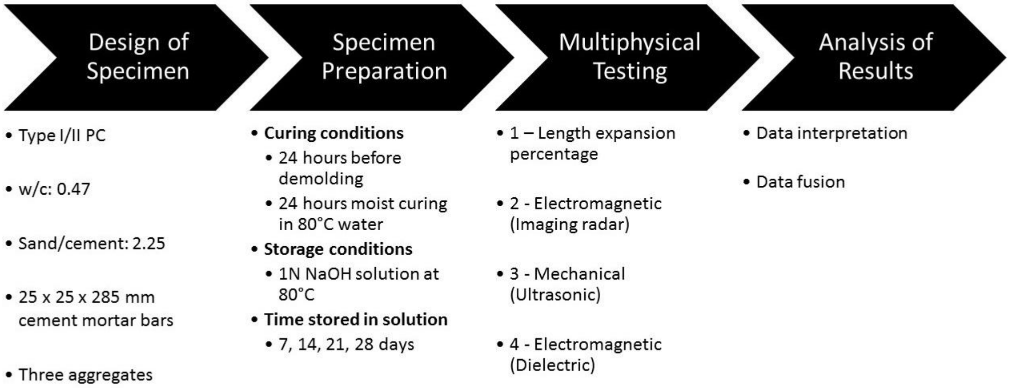

Figure 3-1: Research procedure.

3.1 Specimen Preparation

As mentioned in the literature review, ASTM standards C1260 and C1293 are the most popular. Both are primarily used for the detection of the potential for aggregates prone to ASR. Unlike ASTM standard C1293, C1260 uses smaller mortar bars instead of larger concrete prisms for a testing period of 16 days as opposed to 1 year. In this study, ASTM C1260 was adopted with minor modifications.

Three aggregates, of which two were provided by Grace Construction & Packaging (GCP) Applied Technologies Inc. (Cambridge, MA), were tested in this study. One aggregate was a sand from the university's concrete lab. This aggregate was Quikrete's All-Purpose sand (Quikrete® Companies, Inc.). The material safety data sheet indicates that the sand contains crystalline silica in the form of quartz. The mortar bars made from it will be known as *AG1*, short for "aggregate 1". The two aggregates provided by GCP Applied Technologies Inc. originated from southern parts of the United States. One was a washed sand from the southwest. The aggregate which came from the southwest and the mortar bars made from it will be labeled as *AG2*, short for "aggregate 2". The other aggregate is a sand from the southern part of the country. This aggregate and the mortar bars made from it will be referred to as *AG3*, short for "aggregate 3". Additional information about the aggregates was not provided due to privacy reasons concerning the suppliers.

One batch of mortar, enough for three bars, was composed of 990 grams of fine aggregate and 440 grams of cement for a sand-to-cement ratio (s/c) of 2.25. 206.8 grams of water was added for a water-to-cement ratio (w/c) of 0.47. The cement used was Portland cement Type I/II (Quikrete® Companies, Inc.). The 990 grams of fine aggregates were graded by ASTM C1260, listed in Table 3.1. Mixing of the aggregate, cement, and water was performed by hand. Once mixing was completed, the batch was distributed appropriately into molds, seen in Fig. 3-2. These molds were designed to produce 25 x 25 x 285 mm mortar bars. Dismantle of the mold left a gauge stud embedded at each end of the mortar bar resulting in a 250 mm gauge length. The mixing room (i.e. the university's concrete lab) was approximately 22°C and 64% relative humidity. An example of a pair of mortar bars is shown in Fig. 3-3. After placement in the molds, the mortar bars remained in the mixing room for 24 hours.

Table 3.1: Grading requirements of fine aggregates for ASTM C1260 [8].

Passing	**Retained on**	**Mass (%)**
4.75 mm (No. 4)	2.36 mm (No. 8)	10
2.36 mm (No. 8)	1.18 mm (No. 16)	25
1.18 mm (No. 16)	0.60 mm (No. 30)	25
0.6 mm (No. 30)	0.30 mm (No. 50)	25
0.3 mm (No. 50)	0.15 mm (No. 100)	15

Figure 3-2: Molds used for mortar bars.

Following the initial storage in the mixing room, the molds were dismantled and the mortar bars removed. In a separate lab (i.e. the university's environmental engineering lab), a 28L Cole-Parmer® StableTemp Digital Utility Water Bath, seen in Fig. 3-4 was filled with sufficient tap water to immerse the mortar bars. The bath was set to 80°C. Prior to placing the mortar bars in the water for an additional 24 hours, initial length expansion percentage measurements were made using the Humboldt® Length Comparator with a digital indicator shown in Fig.

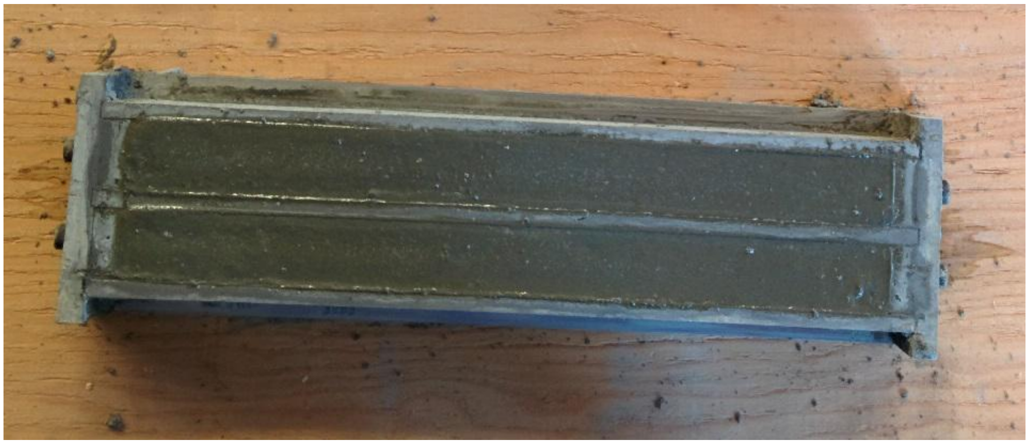

Figure 3-3: Cement mortar mix distributed into mold.

3-5 with a 295 mm reference bar. The mass of each mortar bar was also recorded.

Figure 3-4: Water bath with custom temperature adjustments.

After 24 hours of immersion in 80°C water, the second readings for length expansion percentage and mass of each mortar bar were made. Once the readings for all mortar bars were completed, they were moved to a second water bath. This bath contained an alkali-aggressive 1N NaOH solution heated to 80°C to provide fuel for ASR to occur and thermal energy to accelerate the reaction. For immersion of six mortar bars, 5L (Liters) of the NaOH solution was prepared.

Figure 3-5: Length comparator for measurement of length expansion percentage.

Expansion measurements were made every other day at approximately the same time in a day.

Each set of mortar bars made from three different aggregates (*AG1*, *AG2*, *AG3*) had four periods of time for immersion in the 1N NaOH solution: 7, 14, 21, and 28 days. In addition, each mortar bar was duplicated due to the convenience of the design of the mold. As a result, a total of 24 mortar bars were made: 8 for each aggregate and 6 for each time period. Images of all mortar bars can be found in Appendix A.1. After the multiphysical tests were completed, half of the mortar bars were returned to the water bath in the high alkali solution and the other half were left in ambient conditions to dry. The ones returned to the high alkali solution will henceforth be referred to as wet or *MB1* (i.e. mortar bar set 1). The mortar bars left out in ambient conditions will be referred to as dry or *MB2* (i.e. mortar bar set 2).

3.2 Synthetic Aperture Radar Imaging

After the end of each time period of immersion in the 1N NaOH solution, the mortar bars were removed from the bath and left to dry for 15 minutes. They were subsequently taken to a separate lab for the SAR imaging scans using a continuous wave imaging radar (CWIR) system with a center frequency of 10 GHz, a bandwidth of 1.5 GHz, and HH polarization. This frequency was used due to the wavelength and cost of the antenna. An image of the radar instrument is provided in Fig. 3-6.

Figure 3-6: The microwave imaging radar instrument.

Radar signals were emitted from the radar instrument and the specular returns were subsequently collected and converted into the amplitude values, I, of the SAR image. The amplitude of these specular returns was governed by several mechanisms including reflection off the front face of the mortar bar, diffraction through and around its edges, and multiple reflections through its thickness. Greater amounts of reflected signals and less attenuation were characterized by high amplitudes. A perfect electric conductor or a substance with a high dielectric constant such as water would yield greater amplitudes than other dielectrics such as concrete or Styrofoam. The amplitudes of SAR images were converted into a colormap plot showing a two-dimensional planar view with range (the distance from the antenna to the surface of the mortar bar) and cross-range (the horizontal distance of the synthetic aperture). Each SAR image matrix was resized to dimensions of 480 x 129 using bilinear interpolation.

One mortar bar was scanned at a time by the radar system. The radar was controlled by a two-dimensional positioner that could move vertically or horizontally. Scans were conducted within an anechoic chamber that was custom built with absorbers in order to reduce background noise interference. The mortar bar was placed in two positions on a stand also covered with absorbers. For the vertical orientation, a small absorber was placed on top of the mortar bar to cover the steel gauge stud. For the horizontal orientation, absorbers were placed on the sides to cover each gauge stud. The height of the radar was set at 96 cm from the ground for optimal illumination of the vertically standing mortar bar. It was lowered by 10 cm for the horizontal orientation. Since the radar utilizes stripmap SAR imaging algorithm, the angle at which the antenna pointed at the mortar bar remained the same throughout each scan. Scans were conducted over a cross-range distance of 30 cm ($R_x = 30$ cm) of which the mortar bar would be placed in the center. Range was kept constant for all scans at 40 cm ($R = 40$ cm). Movement of the radar was performed at an interval of 0.3125 cm. Thus, for data collection, radar signals were emitted and received through a periodic time cycle. A sample setup and schematic of the SAR imaging scans in the vertical orientation is shown in Fig. 3-7. One detail to note was that the configuration of these

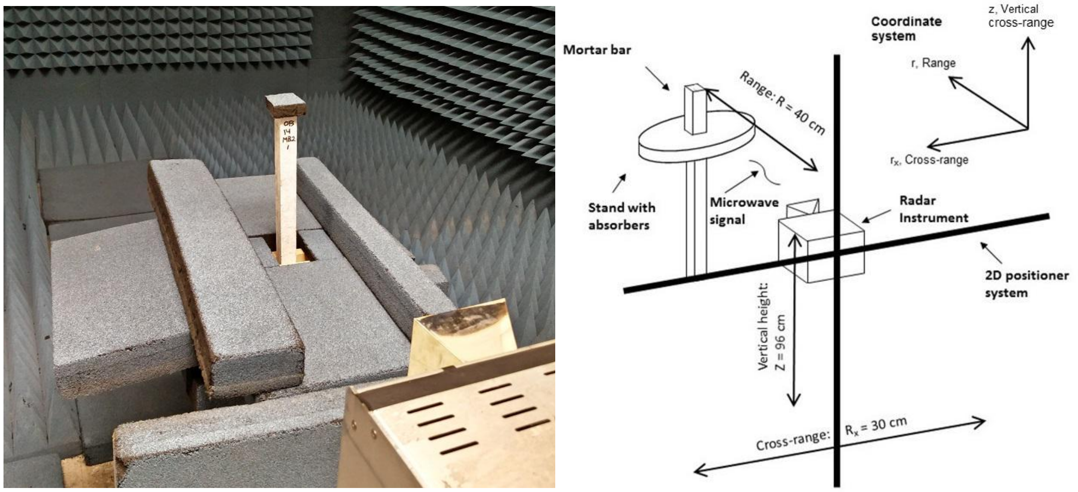

(a) Setup (b) Schematic

Figure 3-7: Setup and schematic of SAR imaging scans of mortar bars in vertical orientation.

absorbers was not absolutely ideal for background noise reduction. Fig. 3-8 shows an example of a scan and plan view schematic of the mortar bar in the horizontal orientation. Each period of SAR imaging was completed with a background scan which encompassed the chamber, the stand, and all the absorbers that were used. This background scan was later used for image subtraction.

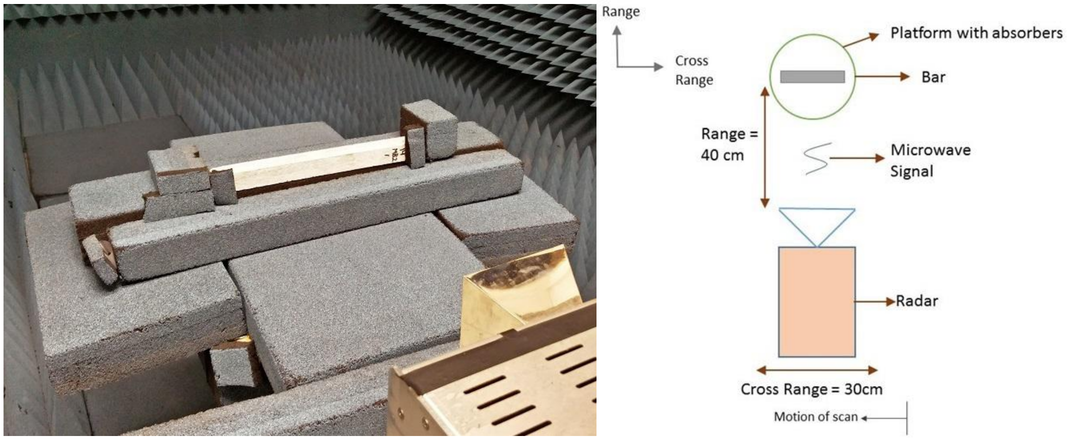

(a) Setup (b) Schematic (plan view)

Figure 3-8: Setup and schematic of SAR imaging scans of mortar bars in horizontal orientation.

3.3 Ultrasonic Testing

Once both vertically and horizontally oriented SAR images were obtained for the mortar bars, they were passed on for UT. The instrument used was the Proceq Pundit® Lab along with its accompanying analysis software, Proceq Pundit® Link. The system consisted of a transmitting transducer and a receiving transducer connected to the Proceq Pundit® Lab. A simplified schematic of the Proceq Pundit® Lab is displayed in Fig. 3-9 [5]. Transmitter voltage and receiver gain were automated for an optimum and stable received signal level. Prior to testing, calibration was performed. Data was collected and saved on a laptop connected to the Proceq Pundit® Lab shown in Fig. 3-10.

Due to lack of availability, the tests were conducted with a 50 mm diameter transducer pair operating at 54 kHz frequency. An important note is that this frequency is much too low for the size of the mortar bars. The requirements for ASTM C597 "Standard Test Method for Pulse Velocity Through Concrete" were

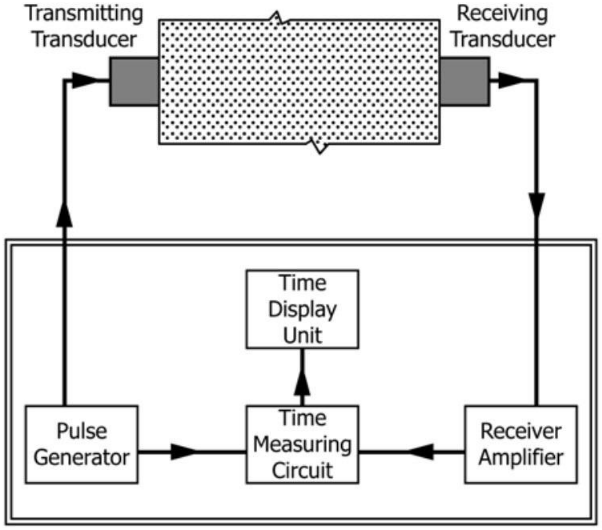

Figure 3-9: Components of ultrasonic pulse velocity measurement device [5].

not met. This standard specifies that "the least dimension of the test object must exceed the wavelength of the ultrasonic vibrations" [5]. Either the cross-section of the mortar bars or the transducer frequency needed to be larger. Despite this failure to meet the ASTM standard, the ultrasonic pulse velocities (UPV) could still be used to estimate the mechanical properties of the mortar bars.

The direct transmission method was adopted for UT. The mortar bars were tested along three surface locations: top, middle, and bottom. Fig. 3-11 demonstrates the testing scheme. After completing measurements on one pair of faces, the process was repeated for the remaining two locations. To ensure optimal contact between the transducer and the surface of the mortar bar, coupling gel was applied. Multiple measurements of UPV were taken at each location and later averaged.

In a separate test at a later time, the wet (*MB1*) 14-day and 28-day mortar bars were removed and their masses were monitored over the course of several

Figure 3-10: Proceq Pundit® Lab with 54 kHz frequency transducer pair.

days. The UPV of the 28 day mortar bars were also recorded for each mass measurement. The focus in this test was to study the effect of moisture loss and the lingering effects of swelling of ASR gels on UPV. At this point, the mortar bars had been stored in room temperature tap water (25° C) for a few months because of the financial and time costs of continued maintenance of the NaOH solution. ASR, therefore, was not expected to persist because of the lack of alkali ions to supply the reaction, but the damage left from the previous storage period in the NaOH solution was studied.

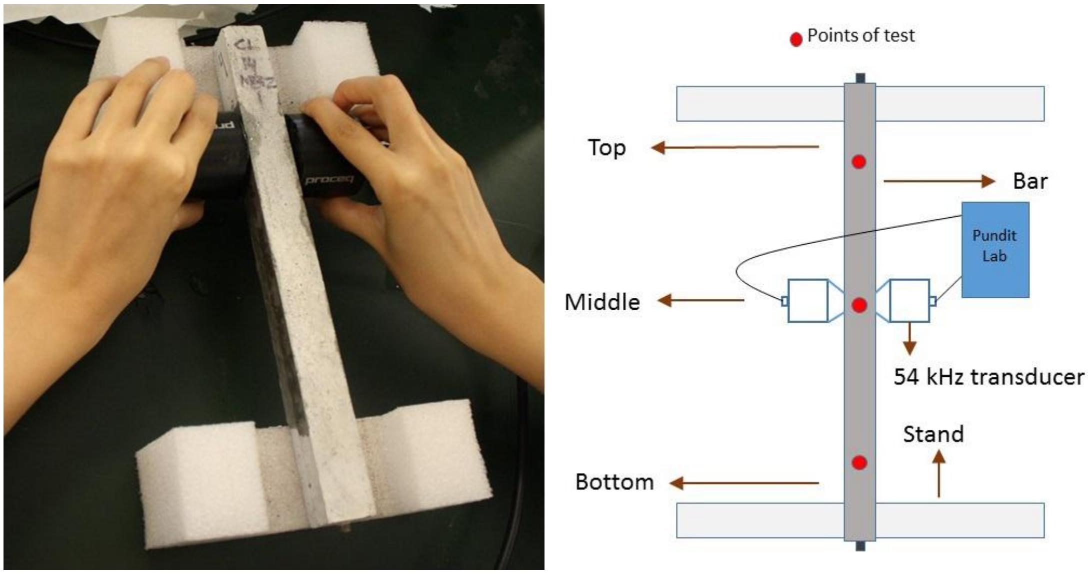

(a) Setup (b) Schematic

Figure 3-11: Setup and schematic of ultrasonic testing.

3.4 Dielectric Measurement

After UT was completed, the mortar bars were wiped clean of the coupling gel and allowed to dry before beginning the dielectric measurement (1 hour). Each mortar bar was given approximately the same amount of drying time. Similar to the SAR imaging radar, measurements of dielectric properties rely on the emission of EM waves within the microwave frequency band and the detection of their subsequent reflections off a material. In this study, an open-ended Agilent® 85070E Performance Coaxial Probe was used in conjunction with a coaxial cable and an E5071C Agilent® ENA Series Network Analyzer that consisted of a signal source, a receiver, and a display (Fig. 3-14). Since only one port of the network analyzer was utilized, incident and reflected signals were transmitted within the same port. Transmitted waves were excluded from this study because they were not measured. The process by which the network analyzer measured dieletric properties of a material is summarized below from Solak [6].

1. Proper contact shown in Fig. 3-12 is made with the coaxial probe onto the surface of the material being tested. The shape of the electric fields at the end of the probe are transformed as they penetrate into the specimen.

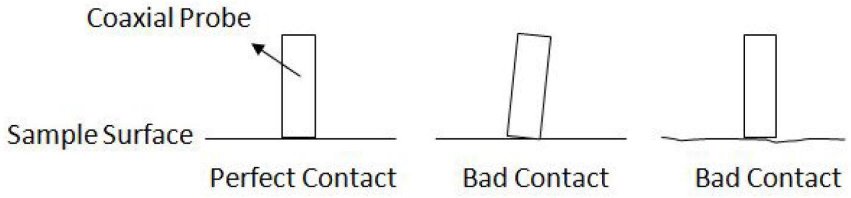

Figure 3-12: Possible contact conditions while conducting measurements using a coaxial probe [6].

2. The signal source from the network analyzer launches a signal at a set frequency which is routed to the material by way of the coaxial cable and probe.

3. The receiver detects the reflected signal (S_{11}) from the material at the set frequency and records its magnitude and phase. The S_{11} measurements are then interpreted for dielectric constant ϵ_r'.

4. The source jumps to the next frequency and steps 2 and 3 are repeated. These processes were completed with 0.04 GHz increments from 0.5 GHz to 4.5 GHz.

Prior to performing each experiment, calibration of the tip of the probe was performed to correct for directivity, tracking, and source match errors possibly present in the reflection measurement. Three known standard materials used for

Figure 3-13: Shorting kit for calibration for dielectric measurement.

calibration were air, water, and a short kit shown in Fig. 3-13. The presence of three other sources of error were known to affect results: air gaps, cable stability, and environmental factors. Several measures were taken to accommodate for these possible sources of error. Measurements were performed in a relatively stable environment to eliminate additional interference from factors such as sudden changes in room temperature or relative humidity. In addition, gaps between the probe and surface were visually inspected to ensure there was as close of a perfect contact as possible. Locations on the surface of the mortar bar that exhibited significant cracking were avoided to prevent the influence of air on the measurements. The cable was also allowed to stabilize and was prevented from flexing as measurements were made. These measurements were conducted on five locations of each mortar bar. The points of contact were situated on the smoother underside of the mortar bars, opposite from the front surface exposed to air during

Figure 3-14: E5071C Agilent® ENA Series Network Analyzer.

the period of curing. Fig. 3-15 shows the measurement scheme.

In a separate test, the dielectric measurement of products from ASR, a majority of which were presumably ASR gels, was conducted. They were obtained from a random occurrence of ASR gels leaching out of the mortar bars shown in Fig. 3-16. ASR gels covered the entire water bath while imbibing any available free water. They were tested with the probe at three different moisture states. ASR gels at the fully saturated state were tested immediately after removal from moist conditions. They were then left in a room temperature environment with controlled relative humidity at approximately 50% for 24 hours and tested at the partially saturated state. After a week in these conditions and quick drying in a microwave, the final measurements were made in the dry state. Prior to the test, the moist ASR gels were pound into a consistent texture. The dried ASR gels were ground up to a texture as close to a powder as possible.

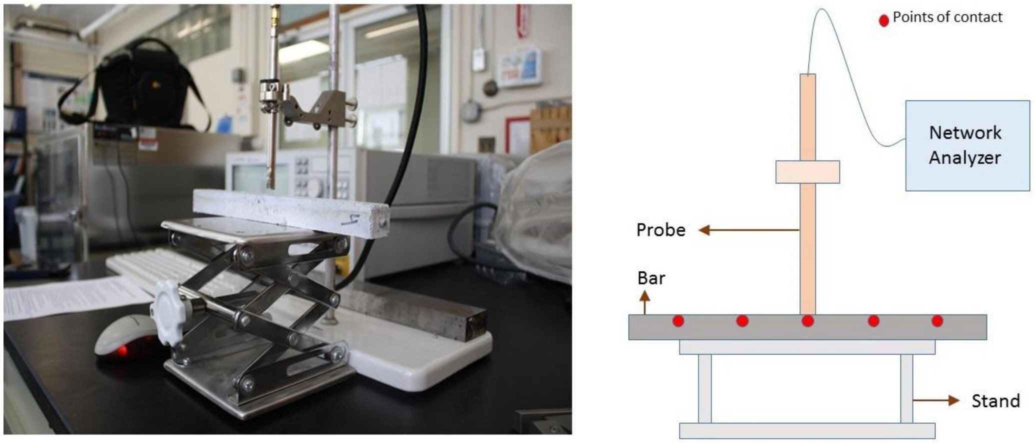

(a) Setup

(b) Schematic

Figure 3-15: Setup and schematic of dielectric measurement.

Figure 3-16: ASR gels leached out of mortar bars.

3.5 Summary

This chapter explained the process of following ASTM standard C1260 to manufacture ASR-afflicted mortar bars for multiphysical testing. The procedure for length expansion percentage measurements was included. In addition, the chapter covered the electromagnetic and mechanical mechanisms by which equipment for the SAR imaging, the ultrasonic testing, and the dielectric measurement operated and their usages in this study.

Chapter 4

Data Interpretation and Fusion

Results from each of the tests were first individually interpreted. These analyses and findings were combined together in order to obtain a comprehensive understanding of ASR gels and their damages on the mortar bars. This thorough data fusion enabled the differentiation between mortar bars made from aggregates reactive and aggregates nonreactive to ASR. Subsequently, the quantification of the degree of damage from ASR gels was achieved. Data interpretation was completed in the following order of the test from first to last: expansion measurements, SAR imaging, ultrasonic testing, and dielectric measurement. Data fusion was reserved as the final step. Findings are summarized at the end of the chapter.

4.1 Length Expansion Percentage

First, the reactivity of each aggregate used in the study was determined. This task, along with the manufacturing of ASR-afflicted mortar bars, was accomplished by following the guidelines set by ASTM standard C1260. Mortar bars that exhibited length expansion percentages less than 0.10% at 16 days after casting were indicative of **innocuous behavior**. Those that were greater than 0.20% were indicative of **potentially deleterious behavior** due to ASR. Length expansion percentages in between 0.10% and 0.20% would **require additional testing to determine the potential for reactivity**. Length expansion percentage was calculated from Eq. (4.1) [8].

$$L(\%) = \frac{L_x - L_i}{G} \times 100(\%) \tag{4.1}$$

L is the change in length at x age (days) in percentage (i.e. length expansion percentage), L_x is the length measurement when compared to a 295 mm reference bar (i.e. comparator reading after calibration with the reference bar), L_i is the initial length measurement (24 hours after the initial casting time) when compared to a 295 mm reference bar, and G is the nominal gauge length of 250 mm.

Fig. 4-1 shows the length expansion percentages of one set of mortar bars stored for 14 days in the NaOH solution and another for 28 days. As seen from these graphs, both sets of *AG2* and *AG3* mortar bars clearly passed the threshold of 0.2 expansion percentage (indicated by the horizontal, magenta line) at 16 days after casting. Their length expansion percentages continued at a decreasing rate well past the day of the tests due to the imbibing of water and subsequent swelling of ASR gels. The damage on the mortar bars would persist until they were taken out of the NaOH solution inside a water bath. The curves for *AG2* and *AG3* at both time periods were compared to the length expansion percentages of mortar bars made from the reactive aggregates found in literature (the dark green solid and light green dashed lines) [74, 75, 76]. The *AG2* and *AG3* mortar bars expanded similarly to those reported in other studies. They all were characterized by two stages of expansion: an initial rapid state followed by a plateauing expansion rate. The initial expansion was primarily due to two mechanisms. First, the drastic change from an environment of room temperature to one heated to 80°C caused significant thermal expansion. Second, the easy transport of abundant alkali ions throughout the pores of a newly cast mortar bars facilitated the occurrence of ASR. The second stage's decrease in expansion rate was attributed to three factors: 1) The supply of reactants needed for the reaction was not as plentiful as ASR consumed the alkali ions and reactive silica. 2) Cement hydration occurring alongside also slowed down the reaction rate. The products from both these reactions (ASR gels, C-S-H gels, etc.) filled the existing pores and some of the newly created cracks, therefore, inhibiting the easy transport of alkali ions. 3) ASR induced cracking occurred mainly within the aggregate and slowly spread out to the mortar bar.

Models of length expansion percentage for the *AG2* and *AG3* 28-day mortar bars were developed in Eqs. (4.2) and (4.3). These models only apply to 25 x 25 x 285 mm mortar bars made from the *AG2* and *AG3* aggregates and continuously soaked in a 1N NaOH solution at 80°C. A change from these conditions may result in different length expansion percentages.

$$L_{AG2}(t) = -3.075t^{-0.1024} + 3.021 \tag{4.2}$$

$$L_{AG3}(t) = 6.079t^{0.03751} - 6.146 \tag{4.3}$$

where L_{AG2} and L_{AG3} are the length expansion percentages of the 28-day mortar bars made from the reactive aggregates and t is the time after casting of the mortar bars (days).

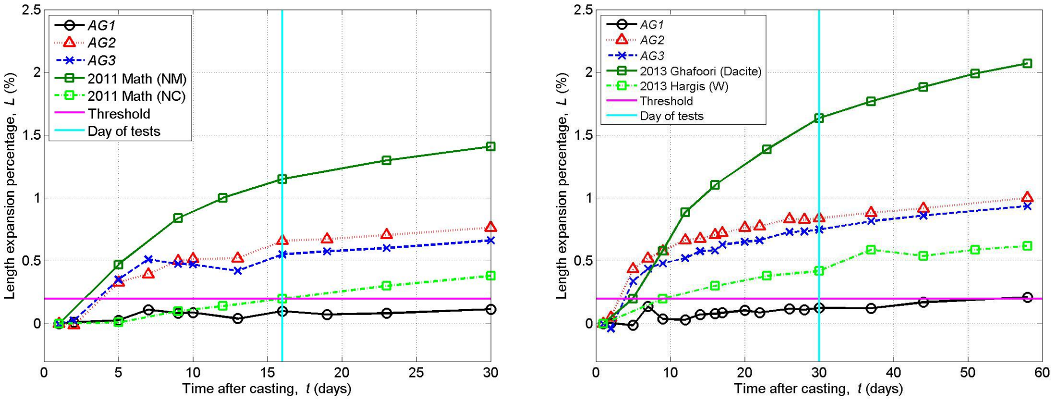

(a) 14-day *MB1*

(b) 28-day *MB1*

Figure 4-1: Length expansion percentages of two mortar bar sets.

Fig. 4-2 shows the length expansion percentages of the mortar bars that were left to dry after the day of the tests. Without a supply of water to absorb and replace the losses due to evaporation, ASR gels, along with the mortar bars, were not able to expand and even showed signs of shrinkage. This behavior can be physically observed in Fig. 4-3 where comparison of a wet 28-day mortar bar (*MB1*) made from the *AG2* aggregate and a dry 28-day mortar bar (*MB2*) made from the same *AG2* aggregate shows a significant difference in amount and width of cracks. Models were not made for these expansions because of the change from a moist, alkali-aggressive storage condition to a drier and lower temperature environment.

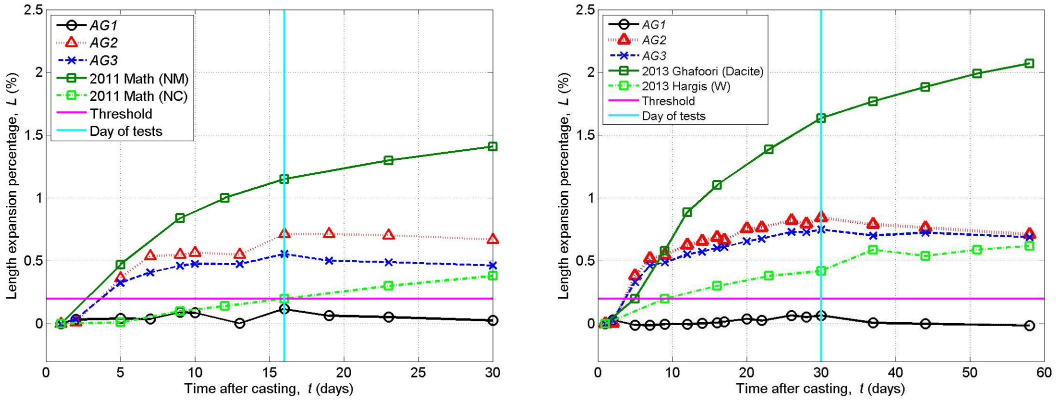

(a) 14-day *MB2*

(b) 28-day *MB2*

Figure 4-2: Length expansion percentages of two mortar bar sets that were left to dry after tests.

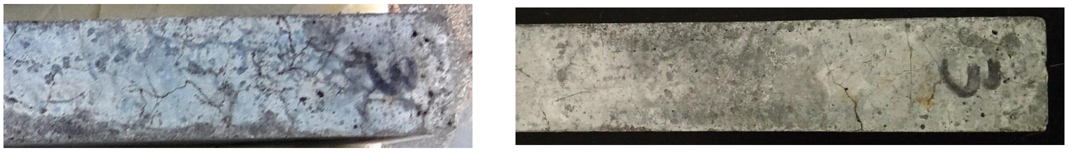

(a) *MB1* - "wet"

(b) *MB2* - "dry"

Figure 4-3: 28-day mortar bars made from *AG2* aggregate.

From these results, it was evident that the *AG2* and *AG3* aggregates were reactive to ASR. The expansions for the remaining mortar bars shown in Appendix A.2 further supported this finding. The mortar bars made from these aggregates were the experimental group. If used in the casting of concrete structures, these aggregates could potentially be dangerous since they would be prone to causing expansive behavior.

On the other hand, the mortar bars made from the *AG1* aggregate were characterized by low length expansion percentages. At no point before the date of tests in any of the expansion curves did the *AG1* mortar bars exceed the threshold of 0.2%. This finding confirmed the innocuous behavior of the *AG1* aggregate. Therefore, the mortar bars made from it were the control group. Some expansion, albeit very minimal, occurred because of the high temperature, moist environment and because of cement hydration. Through visual inspection of Fig. A-4a, the mortar bars made from the *AG2* and *AG3* aggregates even had a covering of white, ASR gels that exuded onto the surface, whereas the mortar bars made from the *AG1* aggregate were spotless.

From the length expansion percentages, the potential reactivity for each of the three aggregates was determined. The degree of damage that ASR gels imposed on the mortar bars were interpreted through the length expansion percentages. The southwestern sand (*AG2*) and the southern sand (*AG3*) were deemed reactive because the mortar bars made from them expanded far beyond 0.2% at 16 days after casting. The sand from the concrete lab (*AG1*) was considered innocuous because its mortar bars expanded below the 0.2% threshold throughout the various time periods of length monitoring. In conclusion, this study contained 16 mortar bars made from two reactive aggregates serving as the experimental group and 8 mortar bars made from a nonreactive aggregate to be used as the control group.

4.2 Synthetic Aperture Radar Imaging

As described in Chapters 2 and 3, the elements of the SAR image matrix represented the amplitude, I, that indicates the strength of the specular return of radar signals as the mortar bars as they interacted with the emitted radar signals. These images were displayed as colormap plots of which the scale was chosen from 0 to 400 for the vertically oriented scans and 0 to 300 for the horizontally oriented scans. To generate cleaner results less influenced by background noise, image subtraction between the SAR image of the mortar bar and the background was done before any qualitative or quantitative analysis was conducted. The entire collection of these subtracted SAR images are placed in Appendix A.4. Initial qualitative inspection of the SAR images did not reveal much difference among the mortar bars. As a result, analytic techniques were required to distinguish the mortar bars made from the two reactive aggregates with those from the non-reactive aggregate. Furthermore, this numerical analysis enabled the temporal quantification of damage in the mortar bars from ASR gels expansion using SAR imaging. Three means were used: maximum amplitude slice, average amplitude slice, and total SAR amplitude. The objective was to look for the influence of ASR gels, in particular, the imbibing of free water. The reflection of additional radar signals due to the high dielectric constant of free water in ASR gels was hypothesized to yield greater amplitudes in the mortar bars made from the reactive aggregates. The correlation between dielectric constant and SAR amplitudes was demonstrated in a separate study in which a steel bar of the same size (a perfect electric conductor with theoretical dielectric constant of infinity) and a similar sized bar made of wood with a relatively low dielectric constant of ~2 were scanned in vertical orientations at 40 cm range [7]. The SAR images are shown in Appendix A.3. The amplitudes from the perfect electric conductor (steel bar) were much greater than those of the wood bar.

Results for maximum amplitude slice were divided into two parts: cross-range amplitude slice and range amplitude slice. The maximum cross-range amplitude slice plotted the highest value from each row of the SAR image matrix $((I_{max})_{r_x})$ with its corresponding cross-range location. For cross-range amplitude slice, 129 amplitude values were plotted with 129 equally spaced points along the 30 cm cross-range. The principle was similar for the maximum range amplitude slice. The highest value from each column of the SAR image $((I_{max})_r)$ was plotted with its corresponding range location. The range slice consisted of 480 points. The collection of both maximum cross-range and range amplitude slices can be seen in Appendices A.5 and A.6, respectively.

Comparison of the cross-range and range amplitude slices at the same time period was first conducted in order to observe the differences between the mortar bars made from the reactive aggregates and their nonreactive counterparts. An example of each slice in the vertical orientation is shown in Fig. 4-4. In these slices, the peaks, along with the nearby high amplitudes around them, occurred approximately in the middle of the 30 cm cross-range and at 40 cm range (some misalignment in the range and cross-range direction could be attributed to slightly inaccurate placement of the mortar bar).

For nearly all range and cross-range amplitude slices for mortar bars scanned vertically and stored in the NaOH solution for 14 days and beyond, each peak of the mortar bars made from the reactive aggregates was greater than that of the *AG1* mortar bars made from the nonreactive aggregate. The only exception came

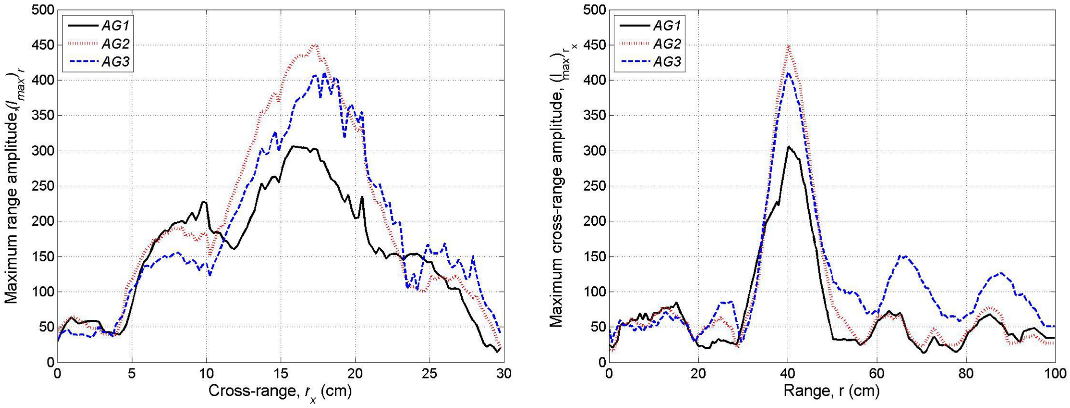

(a) Cross-range slice

(b) Range slice

Figure 4-4: 28-day, *MB1* maximum amplitude slices.

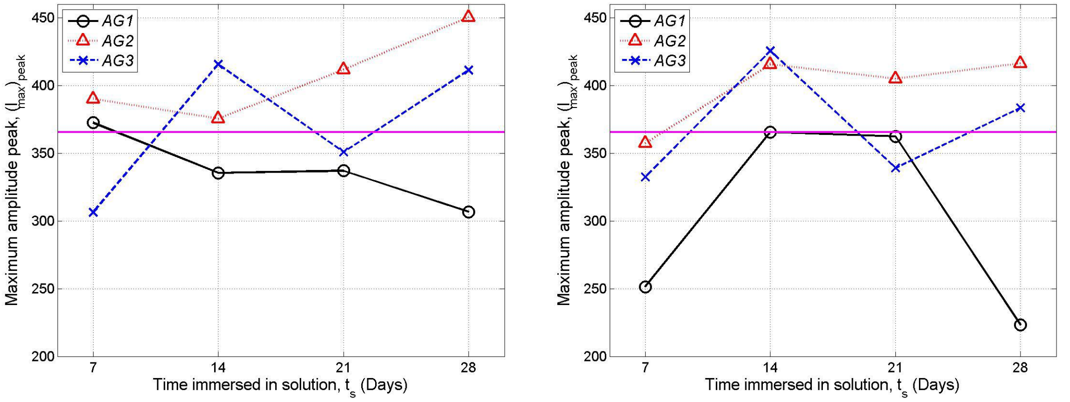

(a) *MB1*

(b) *MB2*

Figure 4-5: Comparison of maximum amplitude peaks for vertically oriented mortar bars.

from the 21-day *AG3* mortar bar. In Fig. 4-5, this consistent difference where the 14-day and beyond *AG2* and *AG3* mortar bars had higher maximum amplitude peaks supported the hypothesis that the intake of water into ASR gels would result in stronger reflection of radar signals. The maximum peak of the mortar bars made from the nonreactive aggregate, stored in the NaOH solution for 14 days and beyond, did not surpass a value of 365.6 in this radar measurement.

The effect of the moist ASR gels was persistent and even remained weeks after

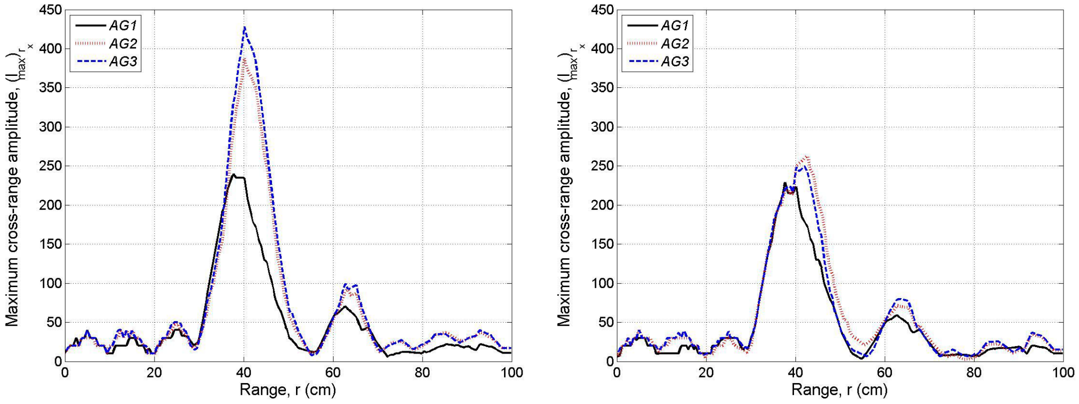

(a) *MB1* (Wet) (b) *MB2* (Dry)

Figure 4-6: Maximum amplitude range slices of 14-day mortar bars two weeks after testing.

the mortar bars were initially subjected to the multiphysical tests. Fig. 4-6 shows the range amplitude slices of the 14-day mortar bars after they had been scanned a second time two weeks later. Recall that, after the testing period, half of the mortar bars were returned to the NaOH solution (*MB1*) and half were left to dry in room temperature conditions (*MB2*). In these slices, the effect of water absorption by ASR gels in the mortar bars made from the reactive aggregates was still prominent. The mortar bar made from the nonreactive aggregate hardly varied in amplitude regardless of its storage in moist or dry conditions indicating the lack of any additional mechanisms by which free water could be retained.

The 7-day mortar bars did not exhibit any difference in maximum amplitudes because of the maturation of ASR gels. At this young age, the amount of water imbibed by ASR gels was not enough to influence the amplitudes. Hence, the 7-day range and cross-range amplitude slices did not exhibit any consistent difference among the mortar bars made from the three aggregates. ASR gels after this 7-day period would be referred to as "matured" because of their influence on the SAR amplitudes.

To confirm the results from the maximum amplitude slices, average amplitude slices were also used. Average amplitude slices utilize a similar principle to maximum amplitude slices but with two changes. Instead of selecting the highest amplitude, an average of the values was obtained for each row or column ($(\left(I_{avg}\right)_{r_x}$ or $\left(I_{avg}\right)_{r})$ of the SAR image matrix. In addition, the window of the analysis was limited from the entire matrix to a cross-range between 5 cm and 25 cm and a range between 30 cm and 50 cm in order to focus the analysis on the mortar bar. This reduction was possible because the location of the mortar bar was known within the SAR image. The collection of these slices can be seen in Appendices A.7 and A.8. Like the maximum amplitude slices, the average amplitude slices were shifted higher for the mortar bars made from the reactive aggregates due to the absorption of free water by ASR gels.

The last approach, total SAR amplitude I_{total}, accomplished quantification of damage from ASR gels at various time periods. Total SAR amplitude accumulated the amplitudes over 50 in the SAR image matrix. This threshold was chosen to exclude the influence from the background. Fig. 4-7 shows that the total SAR amplitude of SAR images for the mortar bars made from the reactive aggregates were mostly greater than that of the mortar bars made from the nonreactive aggregate. One exception for the *AG3*, *MB1*, 7-day mortar bar can be attributed to the maturity of ASR gels. Since this method incorporated the entire SAR image matrix, the results were representative of the whole mortar bar. In this study, total SAR amplitude even further supported the hypothesis that matured ASR gels would lead to stronger specular returns of radar signals due to the high dielectric constant of imbibed free water.

Because of their similarity with relation to time, each of the total SAR amplitudes was divided by the length expansion percentage recorded on the day when the mortar bars made from the reactive aggregates were taken out for the multi-physical tests. By considering the effects of ASR gels for the mortar bars stored for a time period of 14 days and beyond in Fig. 4-8, these ratios between total SAR amplitude and length expansion percentage, $\frac{I_{total}}{L}$, yielded a descending linear relationship with time that was distinct for each aggregate. The ratio between total SAR amplitude and length expansion percentage for the *AG2* and *AG3* mortar bars are represented by the following equation:

$$\frac{I_{total}}{L}(t_s) = a\,(t_s) + b \tag{4.4}$$

where $\frac{I_{total}}{L}$ is the ratio between total SAR amplitude and length expansion percentage, t_s is the time that the mortar bars were stored in the NaOH solution (days), and a and b are experimental constants listed in Table 4.1. An average for each of the constants was calculated to represent both mortar bar sets. The values for the 7-day mortar bars were ignored in order to consider the effects of damage from ASR gels once they had had enough time to develop. Physically, these linear relationships indicated that the increase and subsequent decrease of the total SAR amplitudes over time was slower than those of the length expansion percentages. Using Eq. (4.4) in conjunction with Eq. (4.1), the length expansion percentage and total SAR amplitude for a mortar bar made with the *AG2* and

Table 4.1: Values for experimental constants of Eq. (4.4).

$\times 10^4$	**AG2, *MB1***	**AG2, *MB2***	**AG3, *MB1***	**AG3, *MB2***
a	-1.065	-1.151	-4.432	-4.842
a_{avg}	-1.108		-4.637	
b	153.2	152.1	244.2	257.8
b_{avg}	152.7		251.0	

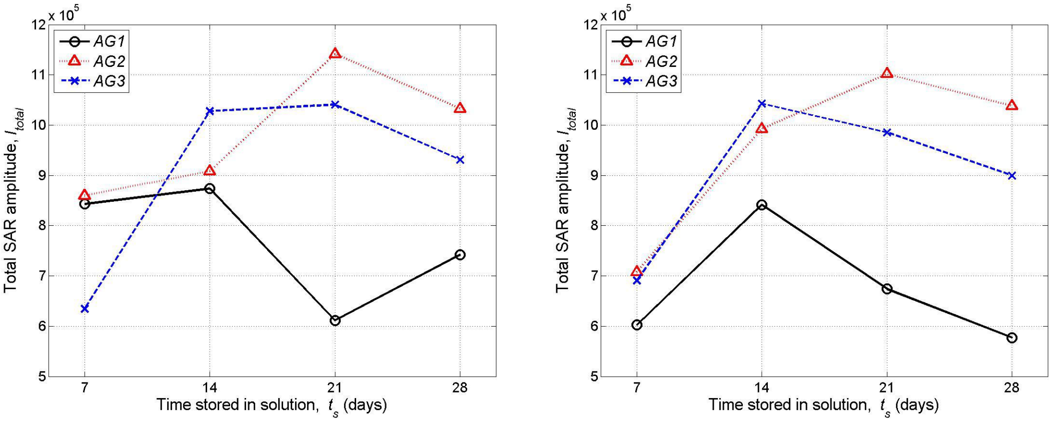

(a) *MB1*

(b) *MB2*

Figure 4-7: Total SAR amplitudes for vertically oriented mortar bars.

AG3 aggregate could be determined if the time stored in the NaOH solution were known beyond 14 days. With this linear relationship developed, the quantification of damage from ASR gels on the mortar bars made from the two reactive aggregates can be accomplished. This modeling was not performed for the mortar bars made from the nonreactive aggregate because of their inconsistency in total SAR amplitude with respect to time. Furthermore, their minimal expansions were insignificant for the ratio calculations, when compared with the ones of the reactive aggregates.

Analysis for the SAR images of the mortar bars in the horizontal orientation was completed with the same procedure: maximum amplitude slices, average amplitude slices, and then total SAR amplitude. Results did not exhibit the same

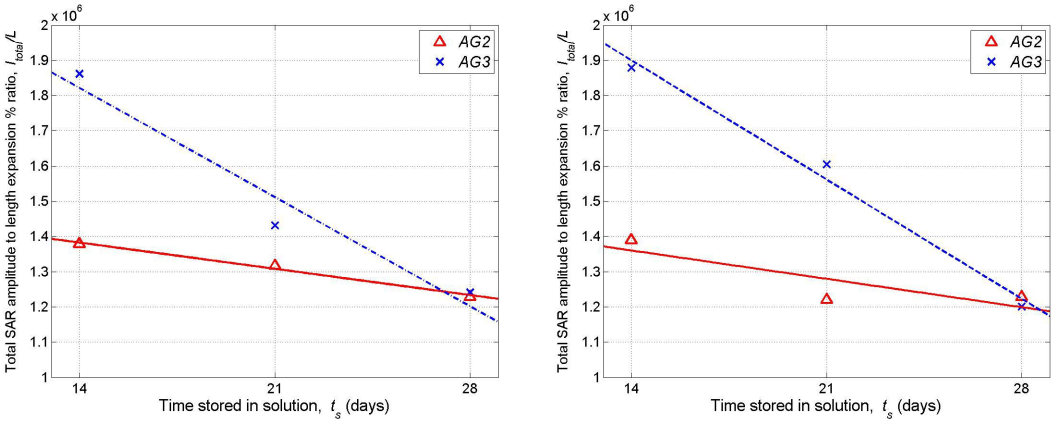

(a) *MB1* (b) *MB2*

Figure 4-8: Total SAR amplitude to length expansion percentage ratios for vertically oriented mortar bars.

consistency as those from the vertically oriented scans. Fig. 4-9 displays the peaks of the mortar bars made from the reactive aggregates varying drastically over the four time periods. Only half of them were greater than those of the mortar bars made from the nonreactive aggregate, and therefore, no conclusion regarding the detection of ASR gels could be made from these results. The setup for the SAR images of the horizontally oriented mortar bars explained this inconsistency. Because of the mortar bar's low height from the stage platform, it was not sufficiently illuminated with radar signals. This positioning issue, along with the close proximity of the absorbers to the mortar bar, limited the response of specular return. Average amplitude slices were taken over the entire cross-range as opposed to a limited section between 5 cm and 25 cm. Results were not improved either. Total SAR amplitude also did not yield any consistent trends. Fig. 4-10 shows erratic variability of total SAR amplitude for the mortar bars in this orientation. In this study, SAR imaging of the 25 x 25 x 285 mm mortar bars when positioned hori-

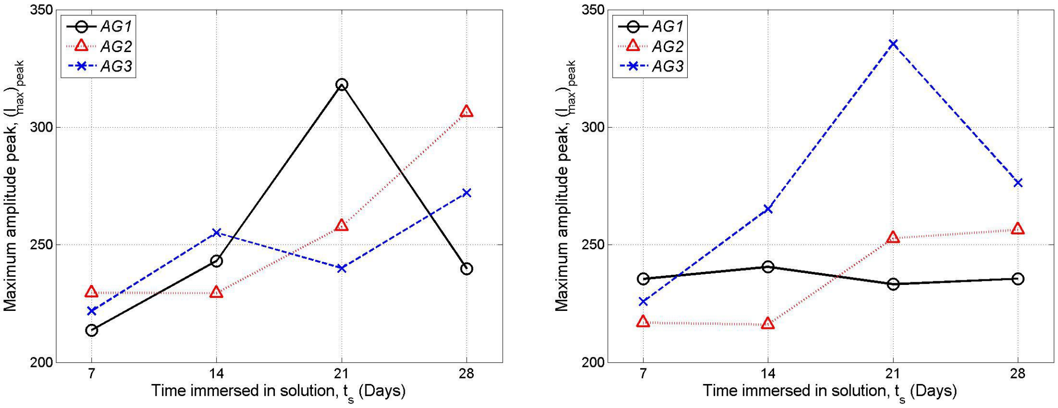

(a) *MB1* (b) *MB2*

Figure 4-9: Comparison of maximum amplitude peaks for horizontally oriented mortar bars.

zontally on the platform of absorbers was not capable in detecting the differences between the mortar bars made from the reactive aggregates and those made from the nonreactive aggregate.

In conclusion, the effect of ASR gels on the mortar bars was observed through SAR imaging. The SAR amplitudes, which were dependent on the dielectric properties of the constituents of the scanned mortar bar, were larger in the mortar bars made from the reactive aggregates because of the high dielectric constant of imbibed free water. This phenomenon was validated by using the analytic techniques of maximum amplitude slices, average amplitude slices, and total SAR amplitude. The capabilities of SAR imaging in differentiating the control group from the experimental group were thus demonstrated. Quantification was achieved through division of total SAR amplitude by length expansion percentage. With representative linear models for mortar bars made from each reactive aggregate, the degree of damage from ASR gels in terms of these two measured quantities

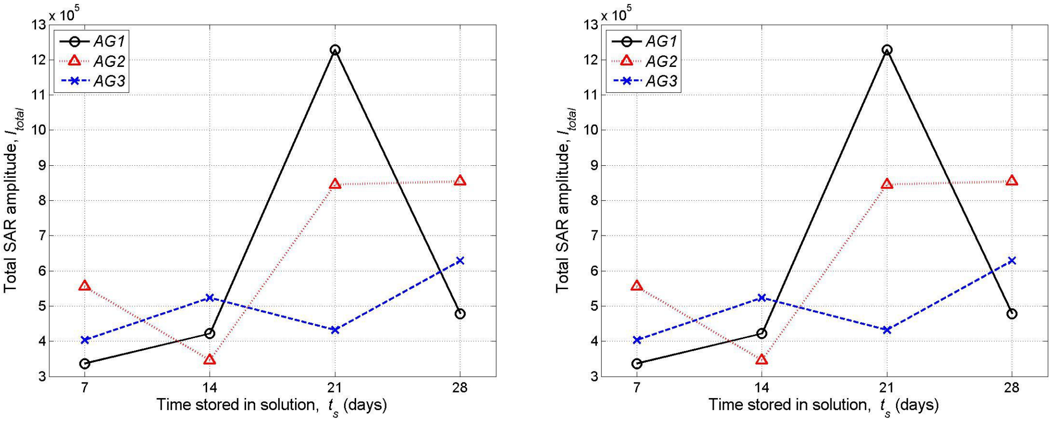

(a) *MB1* (b) *MB2*

Figure 4-10: Total SAR amplitude results for mortar bars in horizontal orientation.

could be determined with respect to time. The descending linear trend of the ratios indicated that the increase and subsequent decrease of total SAR amplitude over time was slower than those of the length expansion percentage. The same analysis was repeated for SAR images of the mortar bars in the horizontal orientation; however, results were not as consistent because of the ineffective illumination of radar signals on the mortar bars. Therefore, SAR imaging of mortar bars in the horizontal orientation to study damage from ASR gels was found to be ineffective and was not recommended.

4.3 Ultrasonic Testing

Ultrasonic testing was used to estimate the mechanical strength of the mortar bars. As mentioned in Section 3.3, the frequency of the transducer pair was too low to meet ASTM C597 guidelines (i.e., wavelength of transmitted wave was larger than the shortest dimension of the mortar bar). As a result, small features and damages such as microcracks would not be identified. However, the measurements were still sensitive enough to differentiate in terms of ultrasonic pulse velocity (UPV) the mortar bars made from the reactive aggregates from the ones made from the nonreactive aggregate. The presence of damage from ASR gels was hypothesized to deteriorate the mechanical integrity of the mortar bars and lower their UPV's.

The UPV results for each of the six measurement points (three for each of the two pairs of faces) were averaged together to obtain a representative UPV for every mortar bar. They are shown in Fig. 4-11 where v represents UPV. The mortar bars made from the nonreactive aggregate, for almost all cases except one (7-day, *MB2*), exhibited UPV's that were greater than their reactive counterparts. Path travelling time of transmitted ultrasonic signals was increased due to the presence of ASR-induced cracking inside the mortar bars. For the mortar bars made from the reactive aggregates, the time periods that exhibited the most amount of damage was 14 and 21 days. The significant decrease in UPV at these times was illustrated by the large number of cracks seen along the surface. The UPV increased at 28 days in all cases due to cement hydration and ASR products filling the pores that were inherently present and the cracks that were introduced. This damage-recovery trend followed that found by other researchers such as Ahmed *et al.* [3]. If the mortar bars made from the reactive aggregates were stored in the NaOH solution and tested at a later period, they would be expected to exhibit lower UPV values due to the degradation of their mechanical integrity from the damage by the swelling of ASR gels. Cement hydration would

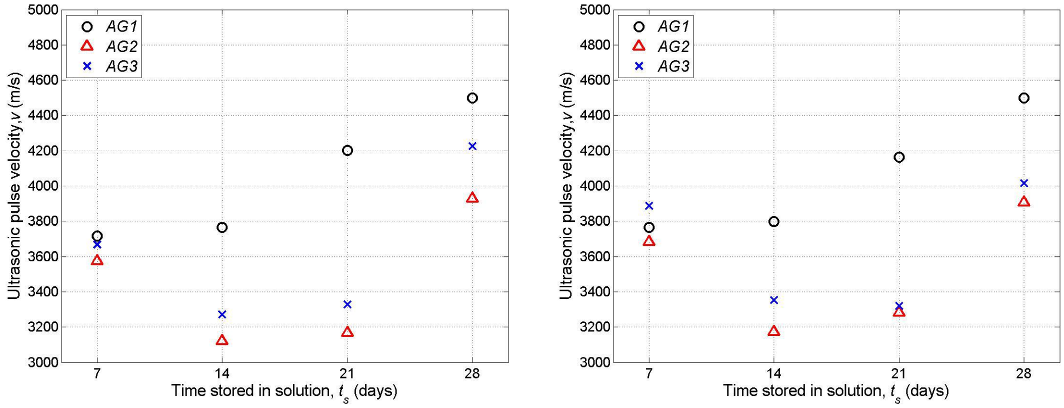

(a) *MB1* (b) *MB2*

Figure 4-11: UPV for all mortar bars at the four testing periods.

recover the UPV at some points but damage would continue in an alkali-aggressive environment. On the other hand, the mortar bars made from the nonreactive aggregate gradually increased in strength until its maximum at the 28th day of storage in the NaOH solution. Longer periods of cement hydration strengthened the mortar bars and raised the UPV.

To link these measurements of mechanical properties with the SAR images, a ratio between total SAR amplitude and UPV was calculated for each time period. The results for the mortar bars made from the reactive aggregates seen in Fig. 4-12 were fitted with a 2nd order polynomial function, Eq. (4.5). Time of storage in the NaOH solution is represented by t_s (days). The constants, a, b, and c, for each curve are provided in Table 4.2. Somewhere in between 14 and 21 days of storage in the NaOH solution, the mortar bars made from the reactive aggregates would return the lowest UPV due to increased damage and cracks from ASR gels. Subsequently, the effect of imbibed water in ASR gels on the SAR image would be maximized within this time frame. At any time earlier, the damage would not be

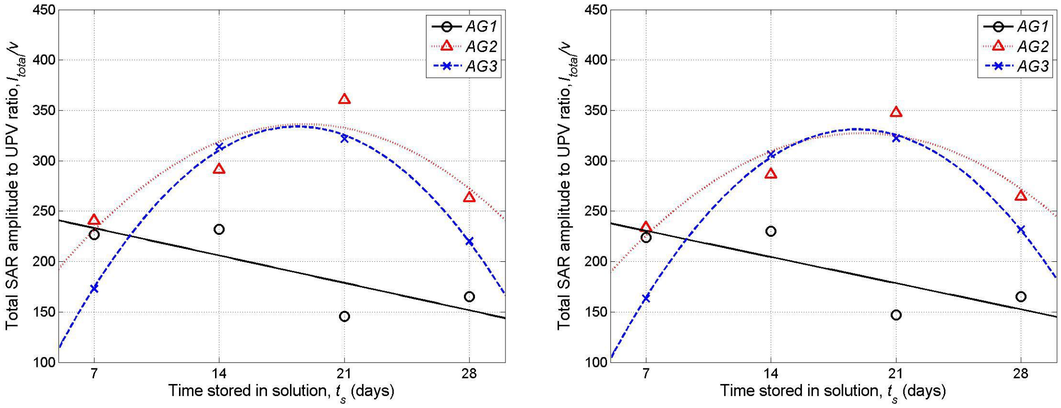

(a) *MB1* (b) *MB2*

Figure 4-12: Ratio between total SAR amplitude and UPV of the mortar bars for the four testing periods.

Table 4.2: Experimental constants for curve fitting of ratio between total SAR amplitude and UPV against time for *AG2* and for *AG3* mortar bars.

	AG2*, *MB1	***AG2*, *MB2***	***AG3*, *MB1***	***AG3*, *MB2***
a	-0.756	-0.695	-1.237	-1.193
a_{avg}	-0.726		-1.215	
b	28.403	26.528	45.440	44.931
b_{avg}	27.466		45.185	
c	69.458	74.186	-83.236	-91.768
c_{avg}	71.822		87.502	

severe enough, and at any time later, cement hydration would have strengthened the mortar bar and closed up many of the cracks. The ratios of the mortar bars made from the nonreactive aggregate, also shown in Fig. 4-12, were fitted with a decreasing linear function, Eq. (4.6), to depict the gradual decrease of total SAR amplitude with time and increase of UPV due to cement hydration. Table 4.3 provides the constants for Eq. (4.6).

$$\left[\frac{I_{sum}}{v}\right]_{AG2,AG3}(t_s) = a\,(t_s)^2 + b\,(t_s) + c \tag{4.5}$$

Table 4.3: Experimental constants for curve fitting of ratio between total SAR amplitude and UPV against time for *AG1* mortar bars.

	AG1, MB1	***AG1, MB2***
a	-3.883	-3.712
a_{avg}	-3.7975	
b	260.3	256.4
b_{avg}	258.4	

$$\left[\frac{I_{sum}}{v}\right]_{AG1}(t_s) = a\,(t_s) + b \tag{4.6}$$

In the separate tests mentioned at the end of Section 3.3, the 14-day and 28-day wet mortar bars (*MB1*) were placed in room temperature conditions and their UPV was measured over the course of several days. The purpose for this was to study the effect of moisture loss and lingering damage from ASR gels on UPV. Mass loss is defined by Eq. (4.7)

$$\Delta_m(\%) = \frac{M_s - M_{t_d}}{M_s} \times 100\% \tag{4.7}$$

where Δ_m is the percentage mass loss, M_s is the mass of the fully saturated mortar bar when it was first taken out for the test, and M_{t_d} is the mass of the mortar bar at time t_d. As seen from Fig. 4-13, the rate of mass loss for the mortar bars made from the three aggregates did not deviate much from each other for both 14-day and 28-day sets. ASR was assumed to have ceased because of the lack of alkali ions when the mortar bars were moved to be stored in tap water. If the mortar bars made from the reactive aggregates had not been removed from the alkali-aggressive environment such as the 80°C NaOH solution, the continued

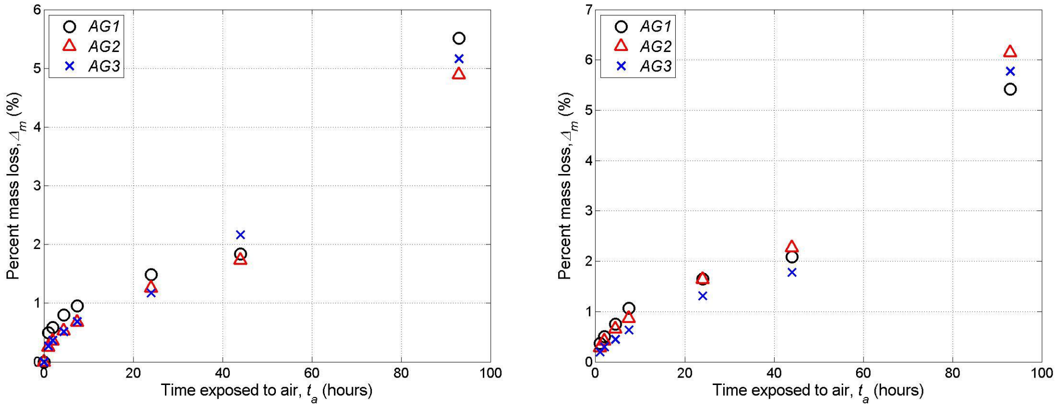

(a) 14-day (b) 28-day

Figure 4-13: Percent mass loss of *MB1* months after multiphysical testing and storage in tap water.

production of ASR gels would have absorbed and bound additional free water resulting in lower moisture mass loss rates.

The UPV's for the drying 28-day mortar bars can be found in Fig. 4-14. With more drying time, the UPV dropped, as expected, because of the added influence of air voids increasing the propagation time of the transmitted acoustic waves. The mortar bars made from the reactive aggregates, though, exhibited lower UPV's than the one made from the nonreactive aggregates. This difference was clearly seen through the curve fitting using the decaying power function of Eq. (4.8). In this equation, v represents UPV (m/s) and t_d is the time that the mortar bar was exposed to air (day). The constants for Eq. (4.8) are shown in Table 4.4.

$$v(t_d) = a\left(t_d\right)^b + c \tag{4.8}$$

The clear separation among the three 28-day mortar bars was due to the presence of cracks in the mortar bars made from the reactive aggregates. Cracks with air

Table 4.4: Constants for Eq. (4.8).

	AG1	***AG2***	***AG3***
a	-694.8	-285.4	-1305
b	0.1660	0.3217	0.08774
c	4198	3540	4584

increased the path travelling time that acoustic waves need to propagate through the mortar bar which led to lower UPV's. Even after months of storage in tap water, cement hydration was unable to fill up the cracks and recover the mechanical integrity of the mortar bars from the lingering damages left behind by ASR gels.

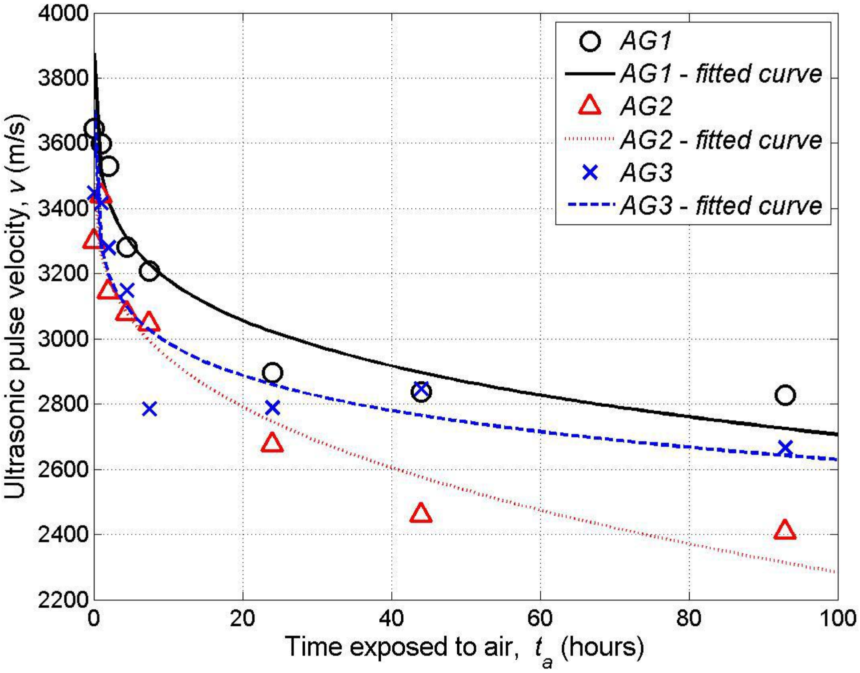

Figure 4-14: Loss of UPV over time for 28-day mortar bars (*MB1*) stored in tap water.

From the ultrasonic testing, the mortar bars made from the reactive aggregates were found to have lower UPV's than the those made from the nonreactive aggregate. This difference was caused by the introduction of cracks from ASR gels. The progression of damage due to ASR gels and recovery due to cement hydration was visible from the results. With mortar bars made from the reactive aggregates, there was a time frame of maximum damage from ASR gels. This period, determined by the peak of the ratio between UPV and total SAR amplitude shown in Fig. 4-12, occurred between the 14-day and 21-day time periods. This ratio with respect to time was plotted and curve fitted by 2^{nd} order polynomials. For the mortar bars made from the nonreactive aggregate, cement hydration led to increases in strength, and therefore, a decaying power function was used to curve fit the ratio over time. The separate tests conducted months after the multiphysical testing confirmed the lingering effects of damage from ASR gels. The mortar bars made from the reactive aggregates were still found to exhibit lower UPV's than their nonreactive counterparts.

4.4 Dielectric Measurement

The final experiment conducted was dielectric measurement using the open-ended coaxial probe and the procedure described in Section 3.4. The purpose of these measurements was to understand the EM properties of the mortar bars and connect them to the amplitudes from SAR images. However, the difference between the measurement schemes should be kept in mind when correlating the results from SAR imaging and dielectric measurement. The CWIR radar system illuminated the entire mortar bar leading to a global measurement of its interaction with radar signals. In addition, the effects from the edges, the entire subsurface, and multiple reflections of the EM waves all contributed to the SAR amplitudes of the mortar bar. In contrast, the dielectric probe was localized in its measurement. It did not capture the interaction between the EM waves and the mortar bar from a holistic perspective, but rather, the primary emphasis was more on surface and near subsurface dielectric measurement. These areas would also experience faster moisture evaporation. Because of the need for proper contact between the probe and the surface, the influence of surface roughness and damages was also magnified. Nonetheless, the dielectric measurements could still be used to understand the mortar bars' electromagnetic properties in the surface and near subsurface regions. The analysis was performed with the assumption that the surface and the near subsurface was relatively dry, save for the imbibed free water from ASR gels.

As mentioned in Section 2.4, the dielectric constant dictated the strength of reflected EM waves from transmitted EM waves into a specimen. Compared to a mortar bar, free water has a high dielectric constant in the frequency range of 0.98 GHz and 4.50 GHz in Fig. 4-15a. It was hypothesized that, due to the absorption of free water by ASR gels, the mortar bars made from the reactive aggregates would have higher dielectric constants than their nonreactive counterparts. These dielectric constants were also believed to follow the fluctuation of the total SAR amplitude of the mortar bars among the four time periods.

Even though loss factor, ϵ_r'', was also obtained through the measurements, the data was not used for any interpretation or modeling in this study. The reason

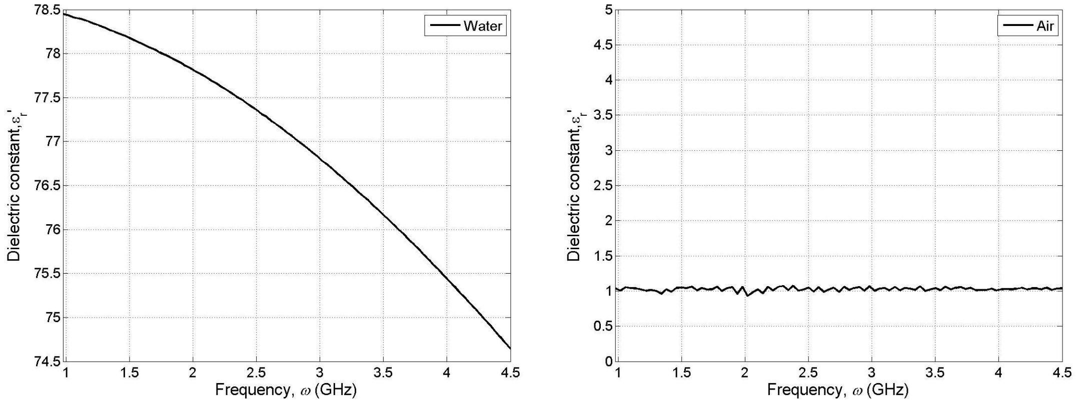

(a) Water (b) Air

Figure 4-15: Dielectric constant of water and air within 0.98 GHz and 4.50 GHz.

for this exclusion was the size of the mortar bars. EM wave penetration through a thick specimen would result in multiple peaks in a SAR image. These peaks would correspond to the delay of the return of the EM waves due to multiple subsurface reflections. Their magnitudes would depend on loss factor which would control the amount of absorption of the EM energy once they entered the specimen. However, the mortar bars in this study were too thin (25 mm) to observe the separation of these peaks which had merged together into one. Other delayed responses resulted in peaks that were too low in amplitude to differentiate them from background noise. For this reason, loss factor was ignored in the analysis.

To obtain a representative dielectric constant curve for each mortar bar, the results at the five measurement locations were averaged together. They were then smoothed using Discrete Wavelet Transform with a level 5 Daubechies mother wavelet. The complete collection of dielectric constant curves for each mortar bar between 0.98 GHz and 4.50 GHz is shown in Appendix A.9. Modeling of the dielectric constant was first performed using Debye's model, Eq. (2.9), repeated

Table 4.5: Parameters for Debye's model.

	Time stored in solution (days)	ϵ_s	ϵ_∞	τ (s)
AG1, MB1	7	3.481	3.021	0.414
	14	5.711	4.650	0.355
	21	5.802	4.947	0.553
	28	6.163	5.244	0.392
AG1, MB2	7	4.864	4.078	0.435
	14	5.204	3.537	0.419
	21	5.412	4.072	0.797
	28	5.862	5.051	0.495
AG2, MB1	7	4.990	3.909	0.384
	14	3.950	3.200	0.383
	21	4.185	3.603	0.497
	28	3.858	3.579	0.396
AG2, MB2	7	5.764	4.840	0.499
	14	3.922	3.207	0.249
	21	5.567	4.897	0.435
	28	5.047	4.479	0.413
AG3, MB1	7	5.095	4.235	0.618
	14	2.814	2.499	0.272
	21	4.804	4.089	0.320
	28	3.815	3.490	0.199
AG3, MB2	7	5.759	4.618	0.458
	14	3.613	3.139	0.196
	21	6.424	5.280	0.601
	28	5.279	4.427	0.375

below. The results for the parameters of the models are shown in Table 4.5 and each are shown in Appendix A.10. With this modeling, the dielectric constant could be predicted at a particular frequency.

$$\epsilon_r'(\omega) = \epsilon_\infty + \frac{\epsilon_s - \epsilon_\infty}{1 + (\omega\tau)^2} \tag{2.9}$$

From observations of ϵ_s and ϵ_∞, the two extremes of the dielectric constant, and of the curves in Appendix A.9, the dielectric constant of the mortar bars made from the nonreactive aggregate were seen to generally increase with age of storage in the NaOH solution. To explain this trend, the cement hydration occurring within these mortar bars should be considered. With a constant supply of water, cement hydration was expected to continue, and this process was evident in the ultrasonic testing as the later aged, 28-day mortar bars were stronger and exhibited higher UPV's. The hydration products were thus able to fill the capillary pores of the cement mortar matrix and expel the air that would affect the dielectric measurement. The presence of air in a mortar bar, shown in Fig. 4-15b, would negatively affect the overall dielectric constant of the mortar bar. The pores of the early-age mortar bars made from the nonreactive aggregate contained more air and less hydration products which in consequence led to lower dielectric constants.

Before analyzing the dielectric constants of the mortar bars made from the reactive aggregates, the EM properties for ASR gels outside of the mortar matrix should be investigated. The collected ASR gels are shown in Fig. 4-16. The moisture content, Ψ (%), of each of the states were calculated using Eq. (4.9).

$$\Psi(\%) = \frac{M_w - M_d}{M_d} \times 100\% \tag{4.9}$$

where M_w is the mass of ASR gels when they contain moisture and M_d is the microwaved, dry mass of ASR gels. The dielectric constant curves are show in Fig. 4-17. As expected, the moist ASR gels were characterized by high dielectric constants due to the presence of free water. Even allowing them to dry for one day yielded dielectric constants that were nearly twice that of materials such as saturated mortar [58]. When they were completely dry, their dielectric constants were significantly lower. Based on the SAR image analysis, the dielectric constants for the mortar bars made from the reactive aggregates were hypothesized to have

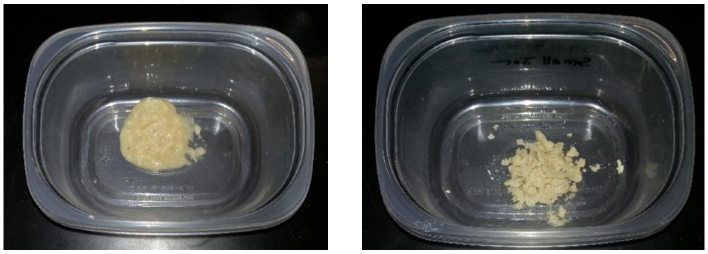

(a) Saturated (Ψ = 6.2%) (b) Partially dry (Ψ = 2.5%)

(c) Dry (Ψ = 0%)

Figure 4-16: ASR gels at three states of moisture.

higher dielectric constants than their nonreactive counterparts.

Looking through the curves in Appendix A.9 and the parameters in Table 4.5, only the 7-day *AG2* and *AG3* mortar bars had dielectric constants greater than those made with the *AG1* aggregate. To explain this difference, the presence of ASR gels should be considered. The 7-day mortar bars, as shown in the length expansion percentages of Fig. A-8 and the images in Fig. A-1, did not suffer significant damages from the swelling of ASR gels. There was some expansion that would have resulted in microcracks near the ASR locations but not enough to produce macrocracks along the surface like the ones on the 14-day, 21-day and 28-day mortar bars. Without these damages, air would not be a major factor in the measurements. The only difference, then, between the mortar bars made from the reactive aggregates and those made from the nonreactive aggregate would be the presence of ASR gels. These gels contributed to the dielectric constants of the

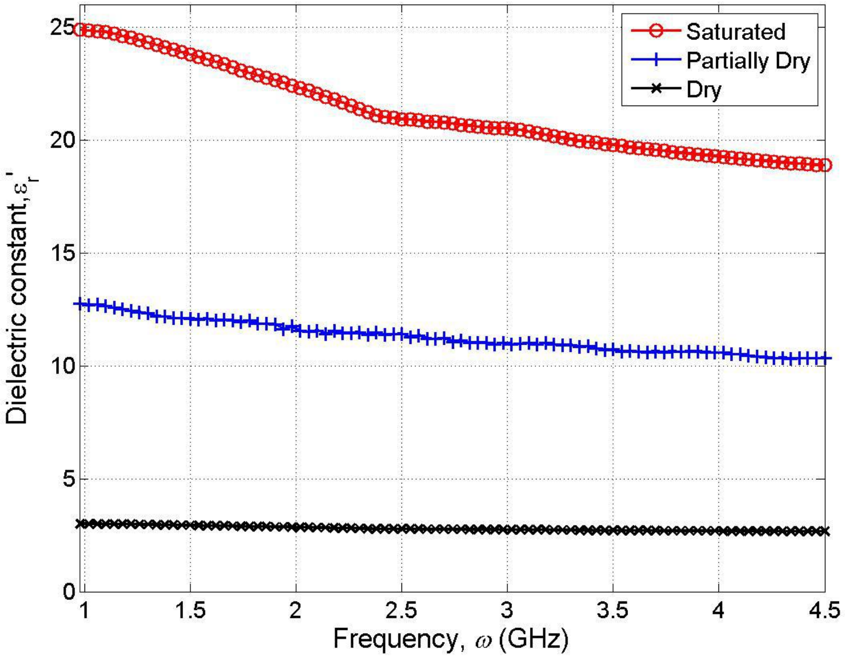

Figure 4-17: Dielectric constants of ASR gels.

7-day mortar bars made from the reactive aggregates in two possible ways. First, they filled the pores of the early age mortar matrix, further expelling the influence of air. Second, their presence slowed down the evaporation of free water. As a result of these two mechanisms, the dielectric constants of the 7-day mortar bars made from the reactive aggregates would be higher than the ones made from the nonreactive aggregate.

Beyond this age, the dielectric constants for the mortar bars made from the reactive aggregates dipped lower than their nonreactive counterparts. This trend contradicted the hypothesis. An explanation considering the influence of the crack damage was proposed. As seen through the images in Appendix A.1 and through the high values of length expansion percentage, the 14-day, 21-day and 28-day mortar bars made from the reactive aggregates were heavily afflicted with the damages such as major surface cracks caused by ASR gels. For the dielectric measurement, locations containing large amounts of damage were avoided. However, additional cracks in the near subsurface could also have been present. These would not be detected immediately with the naked eye and therefore could be unknowingly introduced into the measurement. Furthermore, some mortar bars exhibited an excessive amount of damage, which at certain locations, forced the measurement to be made on a crack which would remove the perfect contact between the probe and the surface. In general (*AG3*, 21-day, *MB2* was the exception), the damage from ASR gels caused the mortar bars made from the reactive aggregates and stored in the NaOH solution for 14, 21 and 28 days to have lower dielectric constants than those made from the nonreactive aggregate.

The increasing and decreasing trends of dielectric constant curves for the mortar bars made from the reactive aggregates were governed by a complex combination of mechanisms that included crack damage evolution, cement hydration, ASR product formation, and free water absorption by ASR gels. The effect of each on the dielectric properties were known and previously explained: crack damage introduces air, cement hydration and ASR product formation expel air from the pores and cracks, and ASR gels imbibe free water. When considering the mortar bar holistically, these mechanisms would compete with one another to raise or lower the dielectric constant. However, a consistent trend was found in which certain mechanisms were distinguishable in their influence on the dielectric constant at particular time periods of storage in the NaOH solution. The consistent drop in dielectric constant from the 7-day to 14-day mortar bars made from the reactive aggregates were due to the evolution of the crack damage from ASR gels. At this time, microcracks had thoroughly propagated throughout the mortar bar and had formed a severe number of macrocracks. As mentioned earlier, this damage introduced a significant amount of air that would reduce dielectric constants. Following this drop, the influence of free water absorbed by ASR gels coupled with their filling of available pores and cracks led to the jump in dielectric constant for the 21-day mortar bars. ASR gels had a more significant impact on the dielectric constants at this time period than the earlier two (7-day and 14-day) because of longer exposure to the NaOH solution and to crack damage. The continuation of the macrocracks opened up more locations for ASR gels to occupy and imbibe free water. In addition, the cracks facilitated the dispersion of reaction products to voids and to areas near the surface. This increase in dielectric constant was found throughout the four sets of mortar bars made from the reactive aggregates. For the 28-day mortar bars made from the reactive aggregates, the dielectric constants fell between those of the 14-day and 21-day sets. At this time period, cement hydration products had been given more time to develop and to recuperate the mortar bars from the damages of the ASR-induced cracking. This recovery not only filled the cracks and pores with hydration products but also limited the transport of ASR gels, moisture, and required reaction components to other regions throughout the mortar bar, especially near surface. This inhibited the production and swelling of ASR gels despite increased time stored in the NaOH solution. With less influence from the more electrically conductive moist ASR gels, the dielectric constants decreased. They did not drop lower than the 14-day mortar bars because less air and more cement hydration products had filled the remaining cracks and pores. At this point, the dielectric constants were determined by competition among the mechanisms of crack damage evolution, cement hydration, ASR, and moisture absorption. To conclude that one would be more dominant than the others would require additional analysis of the individual processes.

In short, the dielectric constants of the mortar bars made from the nonreactive aggregate were generally higher than those made from the reactive aggregates due to the continuation of cement hydration without major damages such as cracks. The 7-day mortar bars made from the reactive aggregates defied this trend because of the filling of pores with ASR gels. The temporal trends in dielectric constant in the older mortar bars (14-day, 21-day, and 28-day) made from the reactive aggregates were characterized by the effects of several mechanisms that competed with each other, namely crack damage evolution, cement hydration, ASR product formation, and absorption of moisture by ASR gels.

4.5 Data Fusion

The integration of the results from each of the tests conducted in this study is the final step of the analysis. Interpreting the data from the experiments together will enable the multiphysical understanding of ASR and its effect on the mortar bars within the four week testing period from both an electromagnetic and a mechanical perspective.

Starting with UPV, the results for the mortar bars made from the nonreactive, *AG1* aggregate were observed to increase with time stored in the NaOH solution due to continued cement hydration. Effects from small amounts of expansion were only slightly noticeable. Mortar bars made from the reactive aggregate showed that UPV dropped significantly between the 14-day and 21-day time periods and recovered subsequently in the 28-day time period due to cement hydration. This reduction and recovery suggested a period of maximum damage from ASR gels.

The results from the two EM tests (SAR imaging and dielectric measurement) also exhibited special characteristics between the time periods from the 14 to 28 days of storage in the NaOH solution. Total SAR amplitude (Fig. 4-7) and dielectric constants (Appendix A.9) of the mortar bars made from the reactive aggregates experienced peaks from the 14 to 21 days of storage in the NaOH solution similar to the valleys in UPV (Fig. 4-11). As explained in the previous sections, dielectric properties were heavily influenced by air and moist ASR gels within the cracks and pores of the mortar bars. In this time frame between 14 and 21 days of storage in the NaOH solution, the mortar bars made from the reactive aggregates experienced the greatest amount of crack damage along with high levels of expansion and absorption of water by ASR gels. Using Eq. (4.5) and the parameters of Table 4.2, this time frame was narrowed down by calculating the peak of the ratio between total SAR amplitude and UPV in between 18 and 19 days of storage in the NaOH solution. Within this range, moist ASR gels had absorbed enough free water and expanded sufficiently to incur the maximum amount of damage that resulted not only in the lowest UPV's but also in the strongest specular returns as they filled in available pores and cracks. Before this peak, the effect of moisture absorption was minimal because of ASR gel maturity, hence the low value for total SAR amplitude for the 7-day mortar bars made from the reactive aggregates. However, as ASR gels occupied the pores of the mortar bar, they expelled air and limited its influence on localized dielectric measurement. From this early age, continued absorption of free water and swelling of ASR gels led to increases in total SAR amplitude, but the further development of surface cracks allowed air to reduce the dielectric constant and the UPV. After the peak between 18 and 19 days, cement hydration products recovered the damage by occupying the pores and cracks. As a result, the production and swelling of ASR gels along with the transport of the reaction components were limited, leading to the increase in UPV but the decrease in both total SAR amplitude and dielectric constant at the 28-day time period. On the other hand, the only recurring pattern the mortar bars made from the nonreactive aggregate showed was the gradual increases in UPV and dielectric constant as cement hydration occurred over the four weeks. Total SAR amplitudes were inconsistent because of the lack of moisture effect from ASR gels.

These multiphysical tests demonstrated the mechanical and EM differences between mortar bars made from a nonreactive and two ASR-reactive aggregates. By distinguishing the mechanical and EM properties of the reactive at each time period of storage in the NaOH solution, the damage from ASR gels was detected and was quantified with respect to time. Using the *AG2*, *MB2* mortar bar, an illustrative summary of the various mechanisms in the mortar bars made from the reactive aggregates that affected the results from the multiphysical tests is shown in Fig. 4-18.

In summary, studying the mechanical and EM properties of the mortar bars made from the reactive aggregates revealed prominent changes and temporal relationships due to ASR gels. Capturing a multiphysical perspective of damage from ASR gels would require an in-depth understanding of the individual mechanisms occurring within the mortar bar.

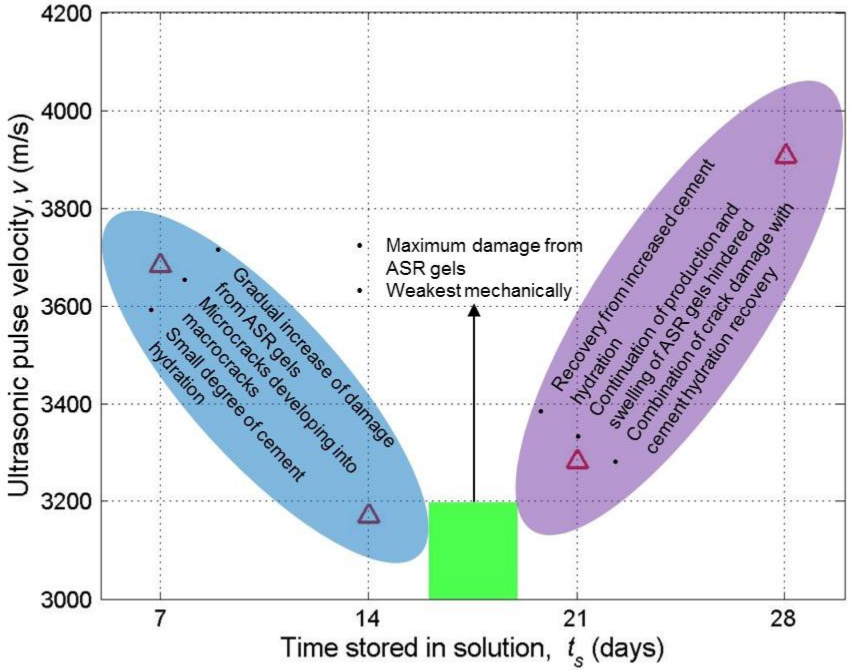

(a) Ultrasonic pulse velocity

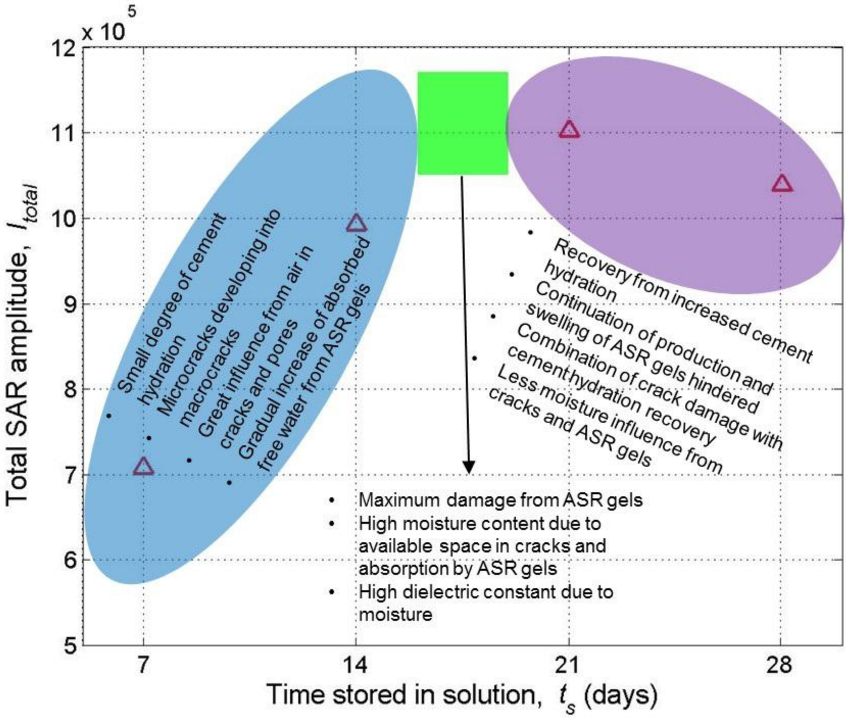

(b) Total SAR amplitude

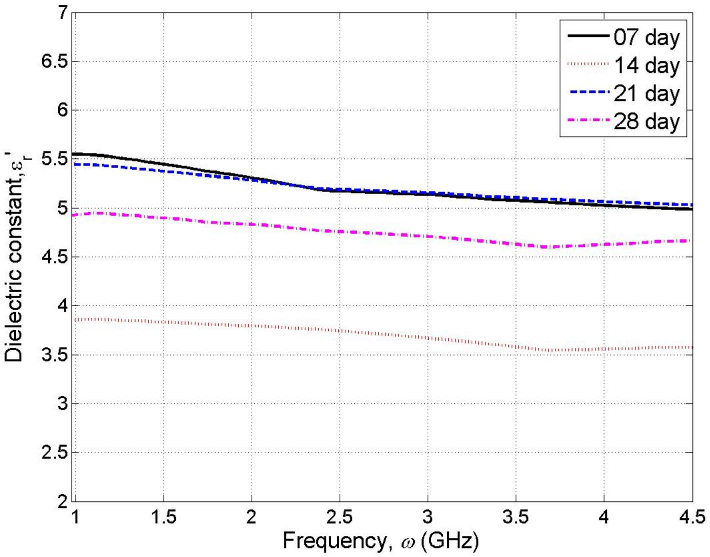

(c) Dielectric constant

Figure 4-18: Multiphysical testing results for *AG2*, *MB2*.

4.6 Summary

In this chapter, the results from synthetic aperture radar (SAR) imaging, ultrasonic testing (UT), and dielectric measurement were presented. They were interpreted in order to understand how ASR gels impose damage on mortar bars. The mortar bars made from the reactive *AG2* and *AG3* aggregates consistently differed from the ones made from the nonreactive *AG1* in SAR image amplitudes, ultrasonic pulse velocities (UPV), and dielectric constants. Trends characterized by singular peaks or valley within the sets of data detailed the mechanical and EM changes experienced by the mortar bars. These changes which were brought about by several mechanisms including crack damage evolution, moisture absorption by ASR gels, and the products from ASR and cement hydration, allowed for the quantification of damage from ASR gels in mortar bars cured in 80° 1N NaOH solution within a four week time frame.

Chapter 5

Conclusions

In this thesis, the mechanical and EM properties of mortar bars with and without damage from ASR gels were studied for detection and quantification purposes. Four sets of 25 x 25 x 285 mm mortar bars were cast from three different aggregates. Each set was stored in 80°C 1N NaOH solution for four separate time periods (7, 14, 21, and 28 days) before being removed and subjected to multiphysical tests. The length expansion percentages of the mortar bars were measured for each time period of storage. The multiphysical tests included synthetic aperture radar imaging using a continuous wave imaging radar system with a center frequency of 10 GHz and a bandwidth of 1.5 GHz, ultrasonic testing using Proceq Pundit® Lab with transducer frequency of 54 kHz, and dielectric measurement using an Agilent® Technologies E5071C ENA Series Network Analyzer with an open-ended coaxial contact probe. Research findings and recommendations for future work are provided in this chapter.

5.1 Research Findings

- **Length expansion percentage**

  From the length expansion percentages, two out of the three aggregates (the ones provided by GCP Applied Technologies) used in this study were found to be reactive to ASR. One was the southwestern sand (*AG2*), while the other was the southern sand (*AG3*). Mortar bars made from these aggregates expanded far beyond the 0.20% threshold set at 14 days of storage in the NaOH solution (Fig. 4-1). Their expansions over 56 days in the NaOH solution were modeled by decaying power functions, Eqs. (4.2) and (4.3). The remaining aggregate from the university's concrete lab (*AG1*) was deemed nonreactive from the results for length expansion percentage. Mortar bars made from this aggregate failed to exceed the 0.20% threshold no matter the amount of time stored in the NaOH solution (Fig. 4-1).

- **Synthetic aperture radar imaging**

  SAR images were analyzed using three methods: maximum amplitude slice, average amplitude slice, and total SAR amplitude. The analysis for the mortar bars made from the reactive aggregates showed that moisture absorption from ASR gels would reflect a greater amount of radar signals and generally lead to higher amplitudes in the SAR image (Fig. 4-5 and Fig. 4-7). For the 7-day mortar bars made from the reactive aggregates, the effect from moisture was less consistent because ASR gels had not imbibed a sufficient amount of free water (Fig. 4-5). Because of the same reason, the mortar bars made from the nonreactive aggregates did not exhibit the same amount of specular return when illuminated with the radar signals. Whether or not they were left in room temperature conditions or the NaOH solution, their maximum amplitude slices did not vary like they would with the mortar bars made from the reactive aggregates (Fig. 4-6). Quantification of the effect of ASR gels on the mortar bars was achieved by using a time dependent linear function with output being the ratio between total SAR amplitude and length expansion percentage on the day of the test. This linear model showed that the increase of total SAR amplitude with time slowed down faster than that of length expansion (Eq. (4.4) and Fig. 4-8). SAR imaging of the mortar bars in the horizontal orientation did not yield consistent results and is not recommended for this study (Figs. 4-9 and 4-10).

- **Ultrasonic testing**

  From ultrasonic testing, the studied parameter was ultrasonic pulse velocity (UPV). The results showed that ASR gel expansion induced cracks which would lower the UPV's of the mortar bars made from the reactive aggregates while cement hydration gradually increased the UPV of the mortar bars made from the nonreactive aggregate (Fig. 4-11). Time dependent ratios between total SAR amplitude and UPV were calculated and modeled by 2^{nd} order polynomials for the mortar bars made from the reactive aggregates (Eq. (4.5)). The peak location between 14 and 21 days suggested a point in which the mortar bars made from the reactive aggregates underwent the maximum amount of crack damage and maximum effect of moisture from ASR gels (Fig. 4-12). A decreasing linear function was used to model the time dependent ratio for the mortar bars made from the nonreactive aggregates to show strengthening through cement hydration (Eq. (4.6)). After storage in room temperature tap water instead of the high alkali solution, the consistent moisture loss in the mortar bars from mortar bars made from all three aggregates showed that the production of ASR gels had ceased (Fig. 4-13). However, the crack damage left behind by the reaction led to differences in UPV between the mortar bars made from the reactive aggregates and the one made from the nonreactive aggregate (Fig. 4-14).

- **Dielectric measurement**

  Only the dielectric constants of the mortar bars were interpreted. Loss factor was excluded because the thinness of the mortar bars (25 mm) did not yield distinct, separate amplitudes within the SAR images that would show the absorption of EM energy as radar signals penetrate through them. In a separate test, the dielectric constant of collected ASR gels increased with moisture content (Fig. 4-17). For the mortar bars, the dielectric constant curves were modeled using the real part for Debye's equation for complex electric permittivity (Eq. (4.5)). The dielectric constants for the mortar bars made from the nonreactive aggregate increased with time stored in the NaOH solution due to cement hydration and ASR gels filling in pores and microcracks created from the minimal expansion (Table 4.5 and Appendix A.9). The mortar bars made from the reactive aggregates stored for the period of 7 days had higher dielectric constants than their nonreactive counterparts because of the filling of pores from both cement hydration and ASR gels (Table 4.5 and Fig. A-55). For the mortar bars made from the reactive aggregates stored in the NaOH solution for 14 days, the high amount of crack damage coupled with low degrees of cement hydration resulted in significant influence from air that decreased the dielectric constant (Table 4.5 and Fig. A-56). At 21 days, the maximum effect from the moisture absorption by ASR gels that filled available cracks and pores led to the highest values for dielectric constants (Table 4.5 and Fig. A-57). For the final period of storage in solution (28 days), the dielectric constants were reduced due to the combination of cement hydration, crack damage evolution, ASR gel formation, and absorption of moisture (Table 4.5 and Fig. A-58).

- **Data fusion**

  Collective interpretation of the results from the multiphysical testing led to detailed descriptions of the mortar bars made from the reactive aggregates at each time period of storage in the NaOH solution. The peak of the ratio between total SAR amplitude and UPV indicated a time range between 18 and 19 days of storage in the NaOH solution where the effects from the crack damage by ASR gels were at a maximum (Fig. 4-18a). The total SAR amplitude and dielectric constant peaked within the same time range indicating the strong effect of moisture from the ASR gels (Figs. 4-18b and

4-18c). The periods of storage before this time range were characterized by higher UPV, lower total SAR amplitudes, and mostly lower dielectric constants due to early age crack damage evolution, cement hydration and ASR gel formation. The periods of storage after this time range also exhibited similar characteristics but for difference reasons. Continued cement hydration recovered the mortar bars from crack damage and hindered the transport and influence of ASR gels and moisture absorption.

5.2 Recommendations for Future Work

The work done for this thesis is part of an initial step towards using both electromagnetic waves in the microwave frequency range and mechanical waves in the ultrasonic frequency range for the detection and quantification of damaged caused by ASR gels. Future advancements in this field certainly can be made. This section provides some recommendations for future studies on ASR and multiphysical NDE.

- In this study, cracks within the mortar bars were a major influence in the measurements. However, in the field, these effects from ASR gels, especially before the formation of macrocracks, would not be detected until damage had become severe enough. Future research could develop a means to restrict the evolution of cracks while maintaining the growth of ASR gels. This approach would enable early detection of ASR prior to the onset of severe damage.

- Experimental design of cementitious composites such as the water-to-cement ratio and of the NaOH solution such as concentration levels can be varied to perform additional parametric studies. The use of deicers, a common source of alkalis in the field, can also be used instead of sodium hydroxide pellets.

- Longer periods of curing in the NaOH solution can reveal more information about the mechanisms affecting the results.

- In the field, ASR gels may occur alongside other forms of degradation such as freeze-thaw damage from the seepage of water into cracks and delayed ettringite formation (DEF). Multiphysical testing could be repeated to study ASR in combination with other mechanisms of deterioration.

- Using 25 x 25 x 285 mm mortar bars was a start for this ASR study. Due to the narrow cross-section and shallow depth in both horizontal and vertical scans, some surface and subsurface details were not capable of being detected by the variation in amplitudes of the SAR image. With a larger specimen such as the prisms from ASTM standard C1293, features such as the propagation of ASR gels and crack damage over specific regions could be identified. In addition, loss factor may be a more important parameter to consider in order to observe the attenuation of EM waves as they pass and reflect off the back of the specimen.

- Improvements in the setup for SAR imaging of the mortar bars in the horizontal orientation can be made especially in regard to placement of the mortar bar and of the absorbers.

- Ultrasonic testing with higher transducer frequency will detect smaller changes such as microcracks and product formation.

- Utilizing a free space measurement system for dielectric properties will provide results from a global perspective which would be more appropriate to compare with the SAR images.

- Multiple assumptions such as homogeneous composition and single polarization were made for the modeling of dielectric constant using Debye's equation. In addition, Debye's model was used for a solid specimen as opposed to a dilute liquid solution or gas for which it would be better suited. To more accurately describe the heterogeneity of the mortar bars and to capture the multiple mechanisms affecting the electrical permittivity, an appropriate dielectric mixing model is necessary. These models can also consider loss factor which was excluded from this study.

- The explanations for the changes in dielectric constants of the mortar bars were derived from a macroscopic perspective. The influence of air from surface cracks, the filling of pores of both cement hydration and ASR gels, and the absorption of moisture were proposed as significant causes for the trends found in the dielectric constants, but they should not be considered as the sole influences. Other factors on the molecular level such as the transformation of free water to bound water and the differences between the minerals of the three aggregates should also be additionally examined.

Appendix A

Appendix - Additional Figures

A.1 Cement Mortar Bars

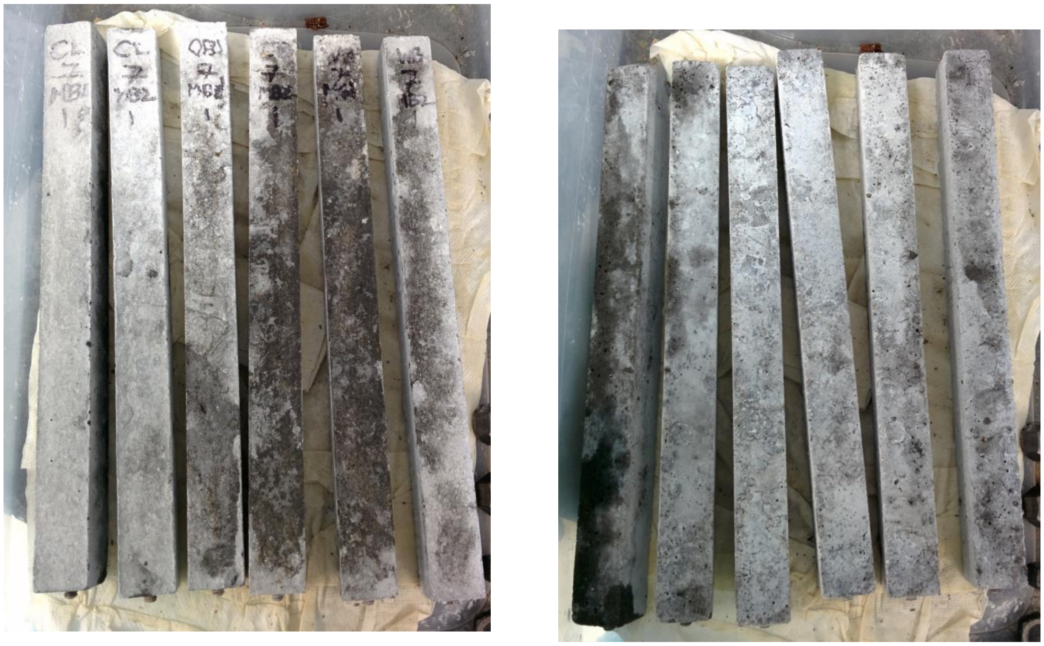

(a) Face exposed to air during molding period.

(b) Face exposed to bottom of mold.

Figure A-1: 7-day mortar bars (left to right - *AG1 MB1*, *AG1 MB2*, *AG2 MB1*, *AG2 MB2*, *AG3 MB1*, *AG3 MB2*).

Figure A-2: 14-day mortar bars (left to right - *AG3 MB1*, *AG3 MB2*, *AG2 MB2*, *AG2 MB1*, *AG1 MB2*, *AG1 MB1*).

(a) Face exposed to a side of mold.

(b) Face exposed to bottom of mold.

Figure A-3: 14-day mortar bars (left to right - *AG1 MB1*, *AG2 MB1*, *AG3 MB1*).

(a) Face exposed to air during molding period.

(b) Face exposed to bottom of mold.

Figure A-4: 21-day mortar bars (left to right - *AG1 MB1*, *AG2 MB1*, *AG3 MB1*, *AG1 MB2*, *AG2 MB2*, *AG3 MB2*).

(a) Face exposed to left side of mold. (b) Face exposed to right side of mold.

Figure A-5: 21-day mortar bars (left to right - *AG1 MB1*, *AG2 MB1*, *AG3 MB1*, *AG1 MB2*, *AG2 MB2*, *AG3 MB2*).

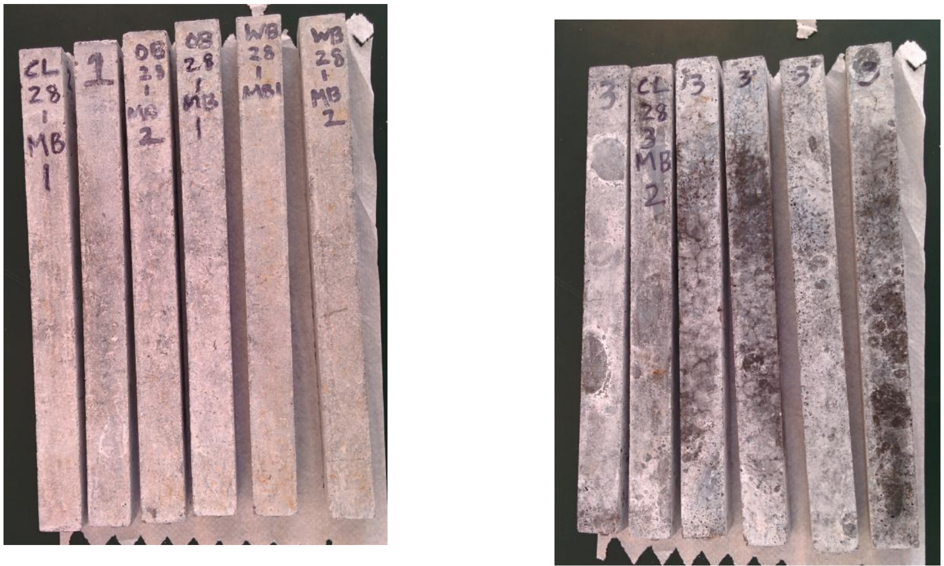

(a) Face exposed to air during molding period. (b) Face exposed to bottom of mold.

Figure A-6: 28-day mortar bars (left to right - *AG1 MB1*, *AG1 MB2*, *AG2 MB1*, *AG2 MB2*, *AG3 MB1*, *AG3 MB2*) (*Note: These pictures were taken when they had been exposed to air for a couple hours; hence, their whiter color and smoother texture.)

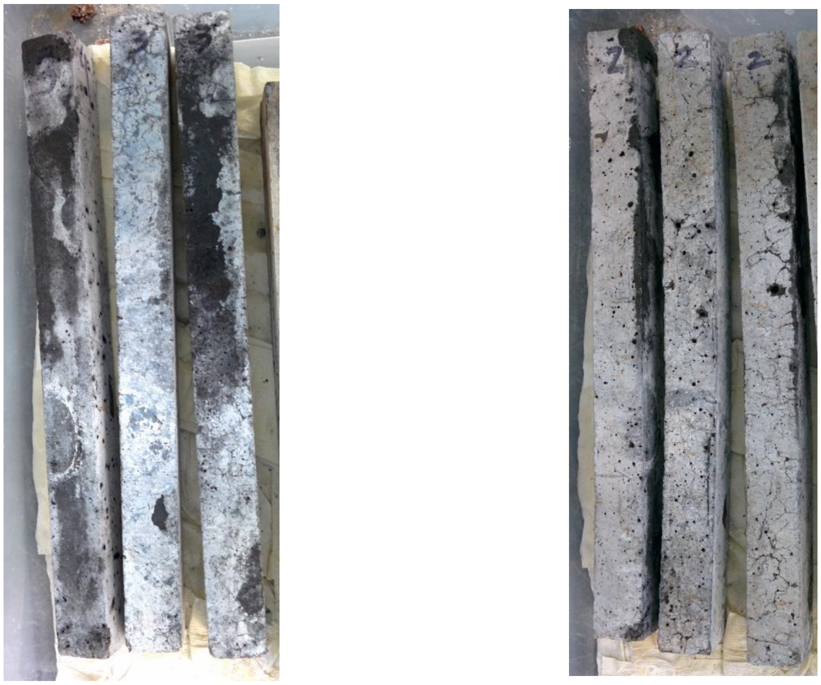

(a) Face exposed to bottom of mold.

(b) Face exposed to a side of mold.

Figure A-7: 28-day mortar bars (left to right - *AG1 MB1*, *AG2 MB1*, *AG3 MB1*) (*Note: These pictures were taken after removal from the water bath, just like the ones stored in the solution for 7, 14, and 21 days.)

A.2 Length Expansion Percentage Plots

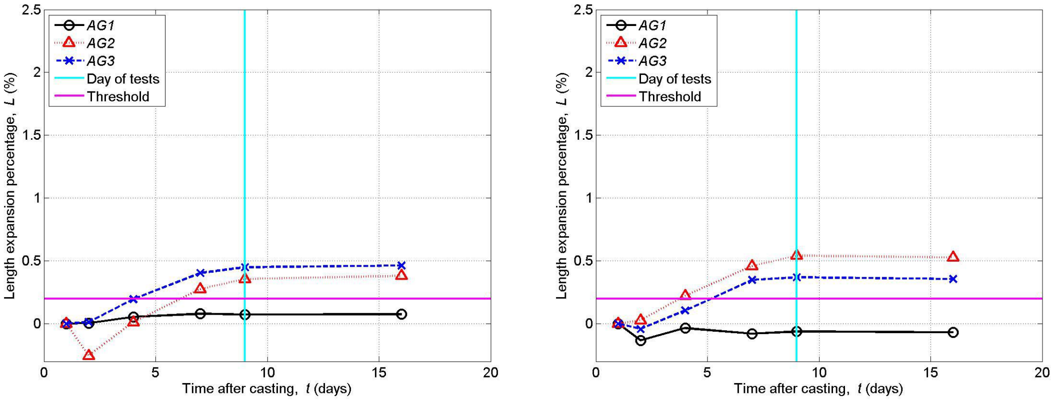

(a) *MB1* (b) *MB2*

Figure A-8: Length expansion of 7-day mortar bar set.

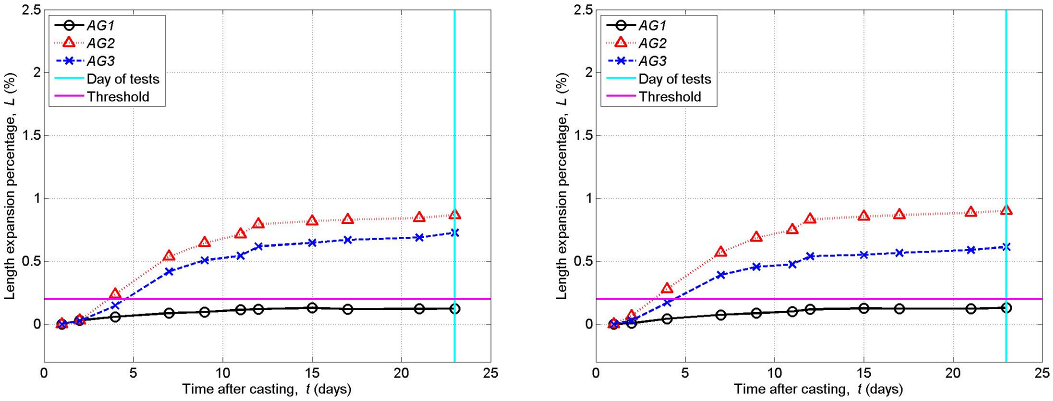

(a) *MB1* (b) *MB2*

Figure A-9: Length expansion of 21-day mortar bar set. (*Note: The monitoring of these bars did not continue after the day of their tests.)

A.3 SAR Images of Steel and Wood Bars

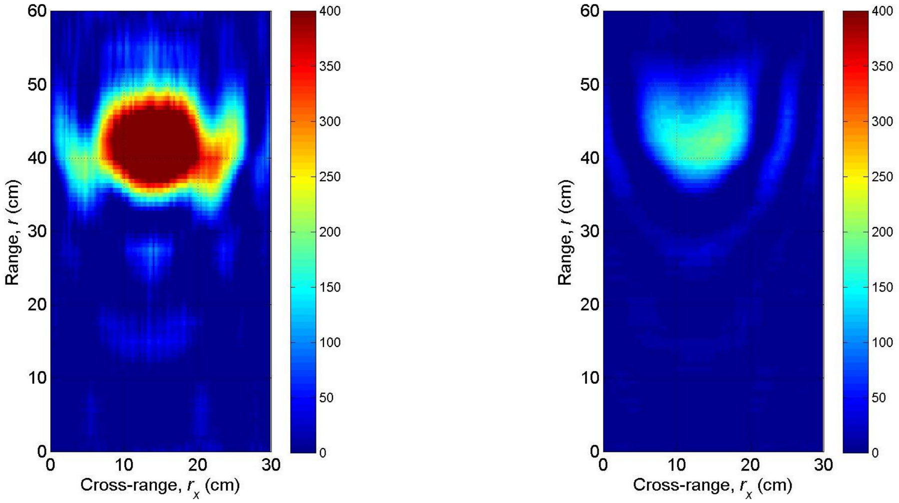

(a) Steel bar

(b) Wood bar

Figure A-10: SAR images of steel and wood bars at 40cm range [7].

A.4 SAR Images

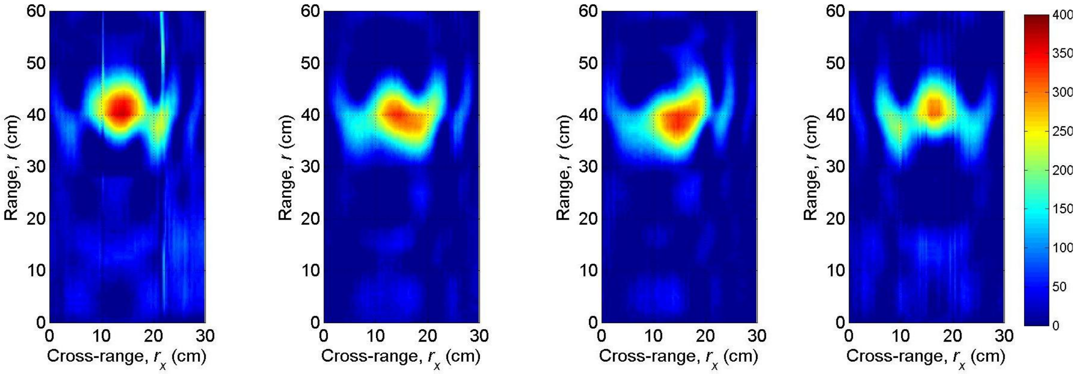

(a) 7-day

(b) 14-day

(c) 21-day

(d) 28-day

Figure A-11: Subtracted SAR image of *AG1*, *MB1* scanned in vertical orientation.

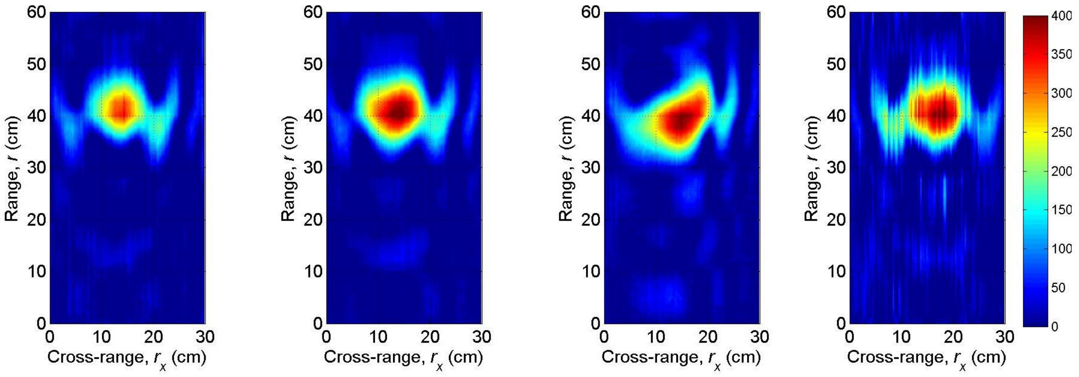

(a) 7-day (b) 14-day (c) 21-day (d) 28-day

Figure A-14: Subtracted SAR image of *AG2*, *MB2* scanned in vertical orientation.

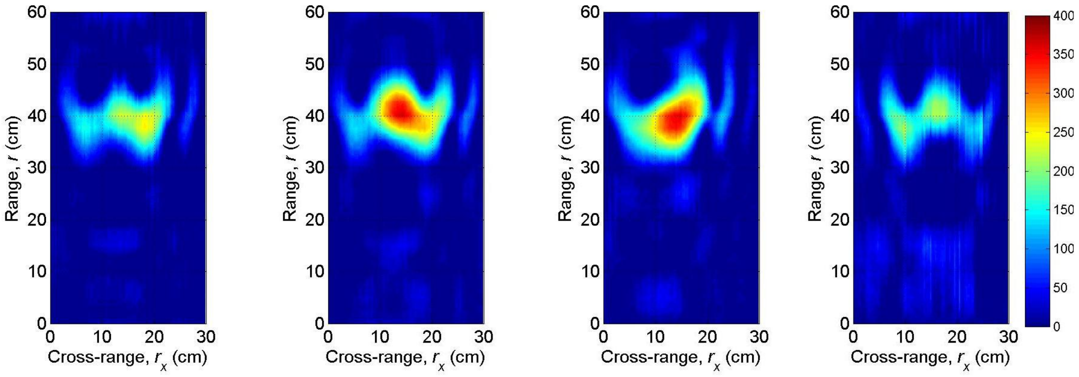

(a) 7-day (b) 14-day (c) 21-day (d) 28-day

Figure A-12: Subtracted SAR image of *AG1*, *MB2* scanned in vertical orientation.

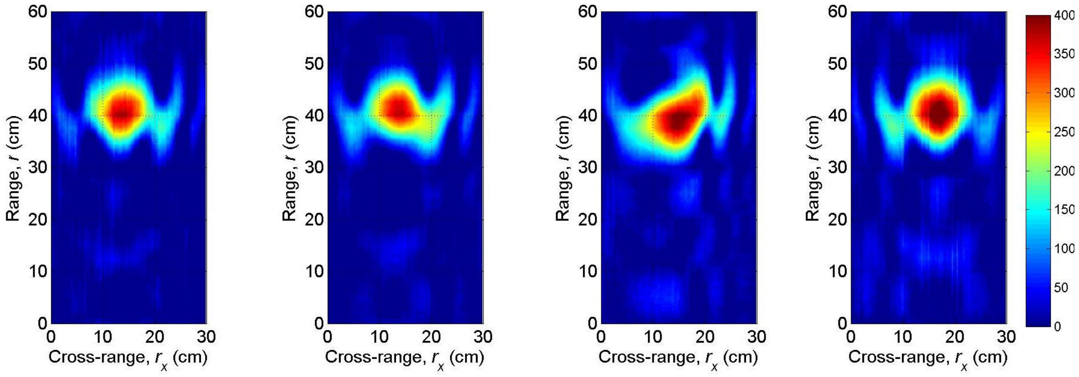

(a) 7-day (b) 14-day (c) 21-day (d) 28-day

Figure A-13: Subtracted SAR image of *AG2*, *MB1* scanned in vertical orientation.

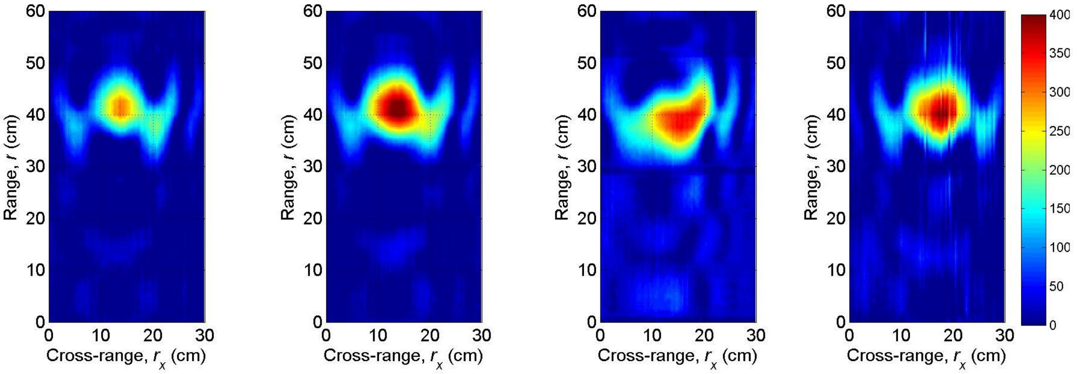

(a) 7-day (b) 14-day (c) 21-day (d) 28-day

Figure A-15: Subtracted SAR image of *AG3*, *MB1* scanned in vertical orientation.

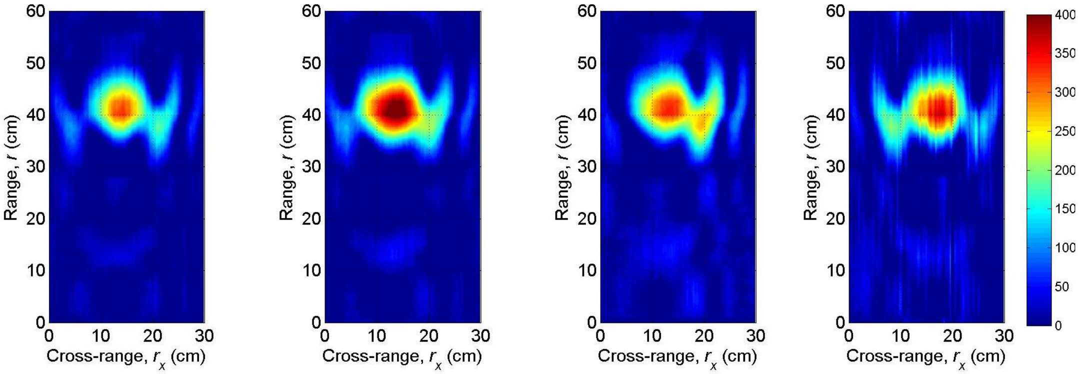

(a) 7-day (b) 14-day (c) 21-day (d) 28-day

Figure A-16: Subtracted SAR image of *AG3*, *MB2* scanned in vertical orientation.

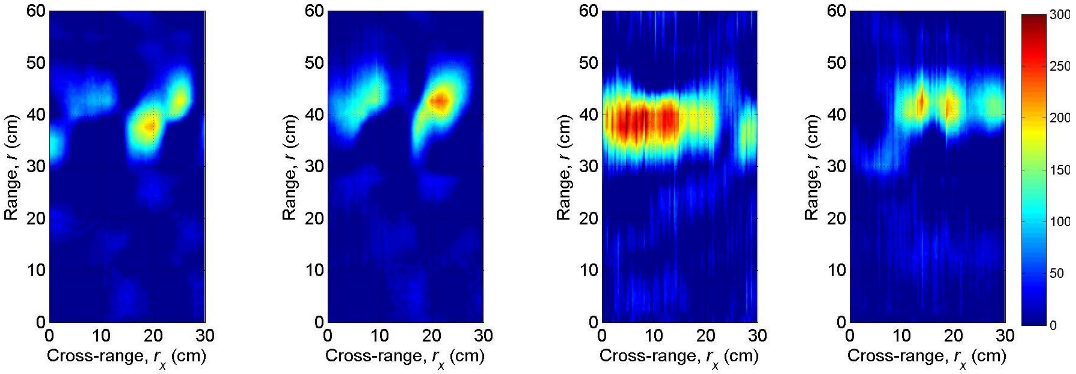

(a) 7-day (b) 14-day (c) 21-day (d) 28-day

Figure A-17: Subtracted SAR image of *AG1*, *MB1* scanned in horizontal orientation.

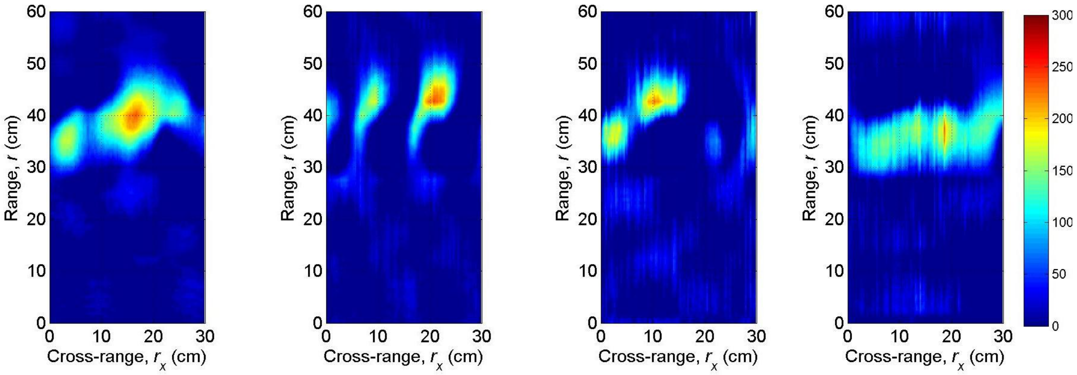

(a) 7-day (b) 14-day (c) 21-day (d) 28-day

Figure A-18: Subtracted SAR image of *AG1*, *MB2* scanned in horizontal orientation.

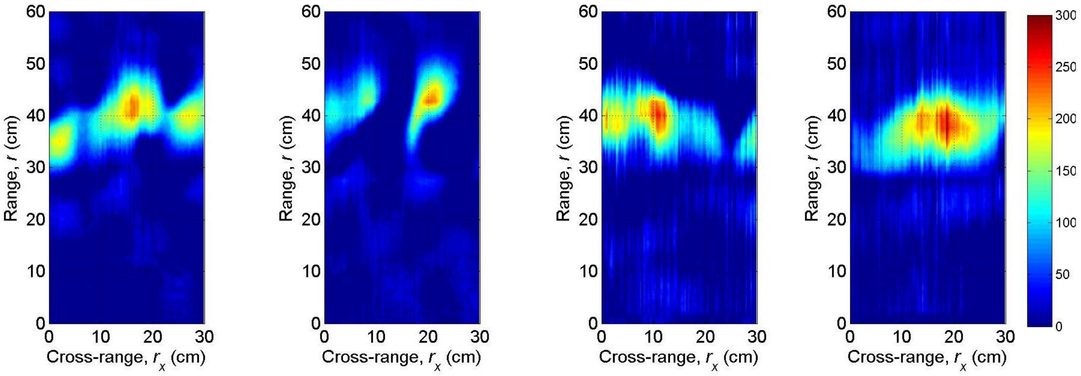

(a) 7-day (b) 14-day (c) 21-day (d) 28-day

Figure A-19: Subtracted SAR image of *AG2*, *MB1* scanned in horizontal orientation.

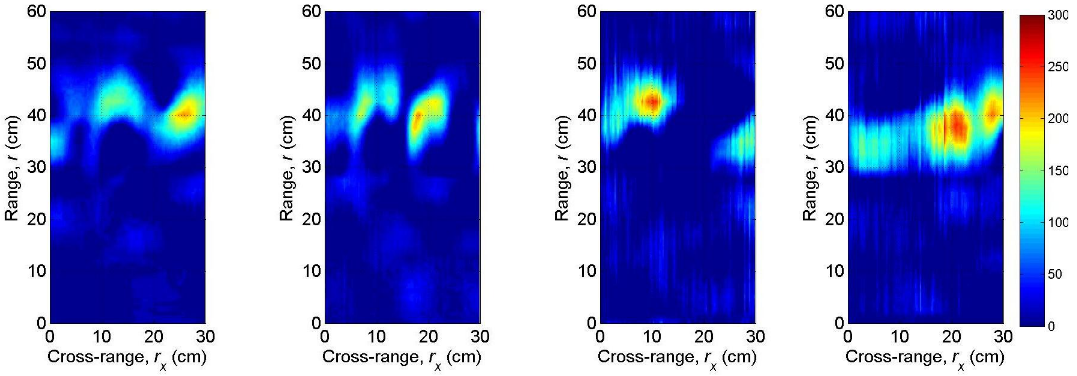

(a) 7-day (b) 14-day (c) 21-day (d) 28-day

Figure A-20: Subtracted SAR image of *AG2*, *MB2* scanned in horizontal orientation.

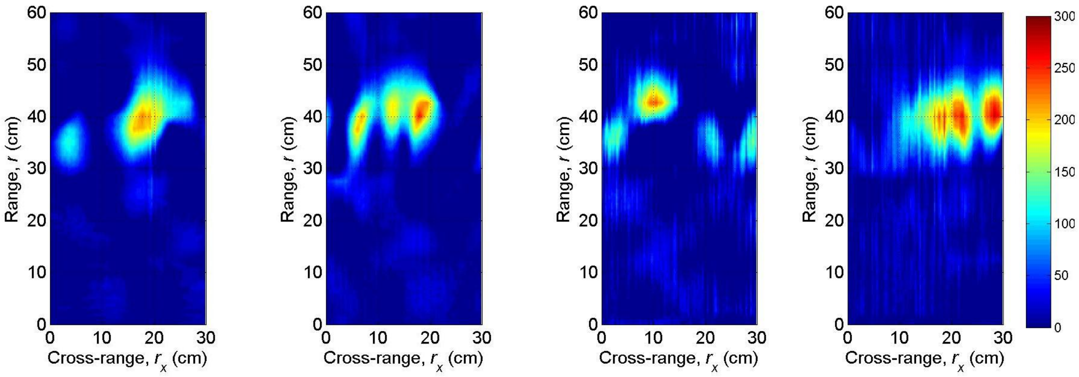

(a) 7-day (b) 14-day (c) 21-day (d) 28-day

Figure A-21: Subtracted SAR image of *AG3*, *MB1* scanned in horizontal orientation.

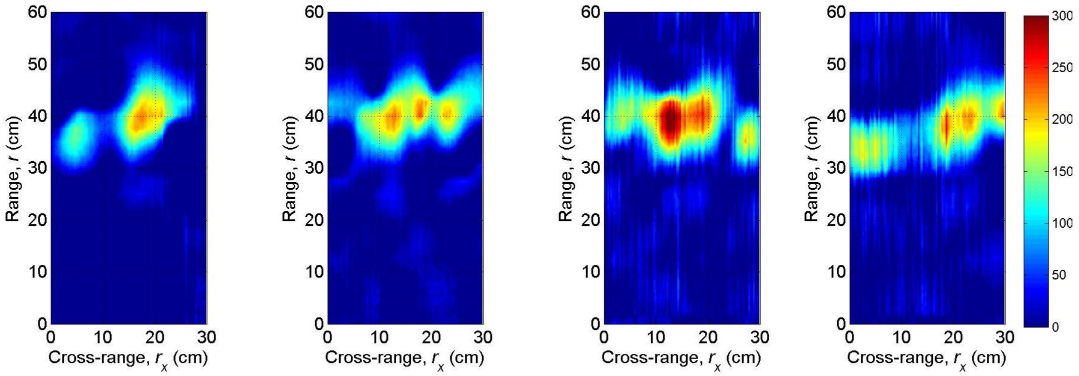

(a) 7-day (b) 14-day (c) 21-day (d) 28-day

Figure A-22: Subtracted SAR image of *AG3*, *MB2* scanned in horizontal orientation.

A.5 Maximum Cross-range Amplitude Slice

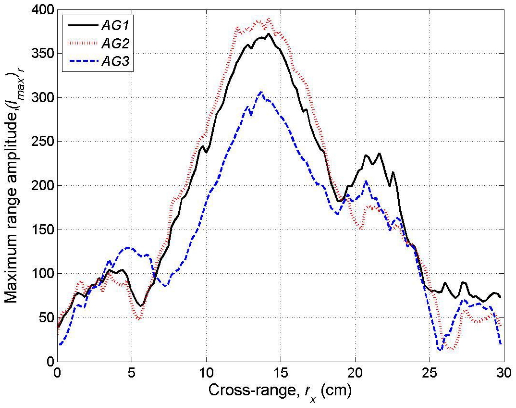

(a) *MB1* (b) *MB2*

Figure A-23: Maximum cross-range amplitude slice of 7-day mortar bars scanned in vertical orientation.

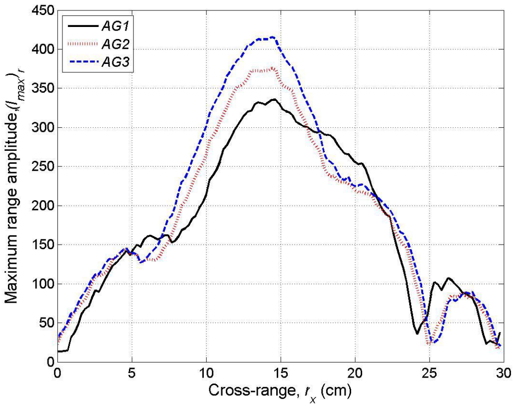

(a) *MB1* (b) *MB2*

Figure A-24: Maximum cross-range amplitude slice of 14-day mortar bars scanned in vertical orientation.

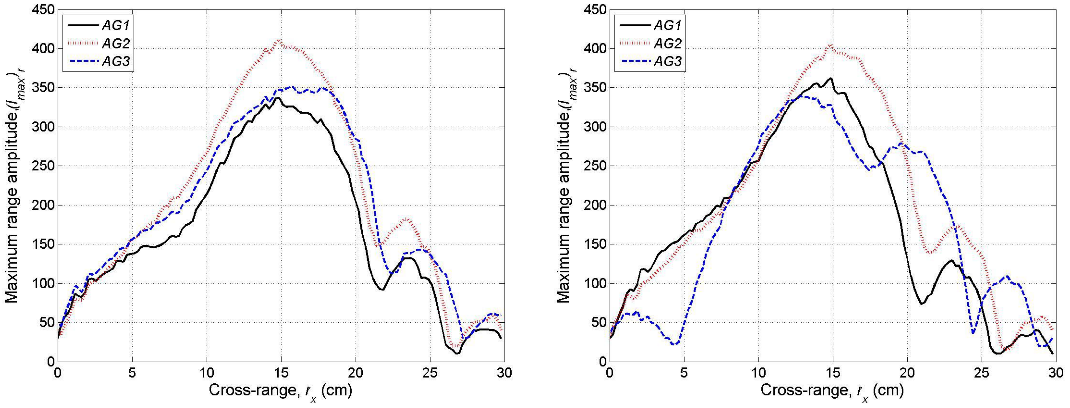

(a) *MB1* (b) *MB2*

Figure A-25: Maximum cross-range amplitude slice of 21-day mortar bars scanned in vertical orientation.

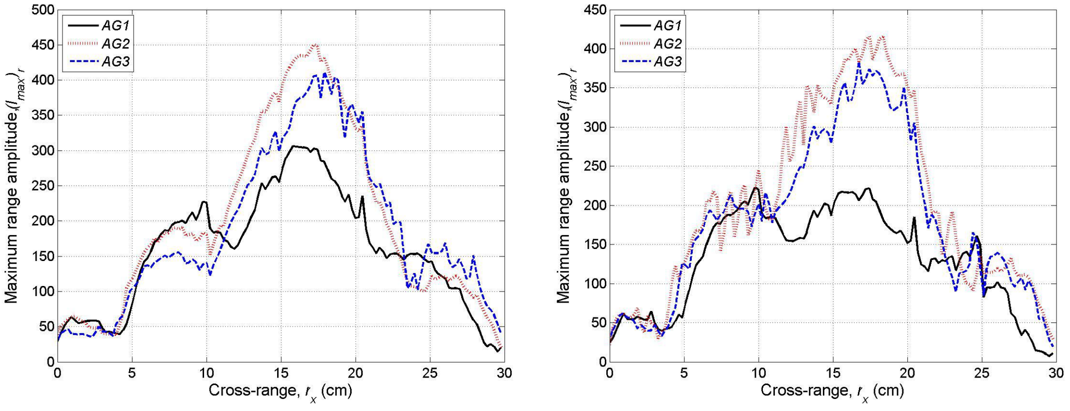

(a) *MB1* (b) *MB2*

Figure A-26: Maximum cross-range amplitude slice of 28-day mortar bars scanned in vertical orientation.

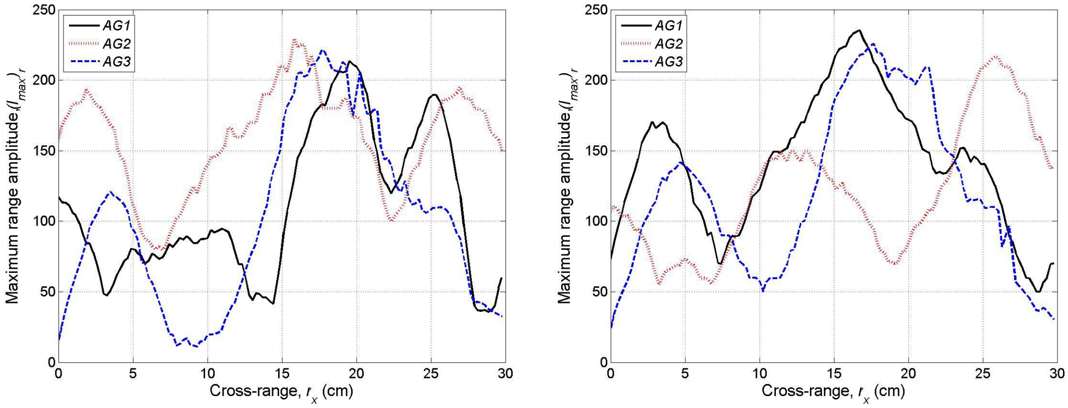

(a) *MB1* (b) *MB2*

Figure A-27: Maximum cross-range amplitude slice of 7-day mortar bars scanned in horizontal orientation.

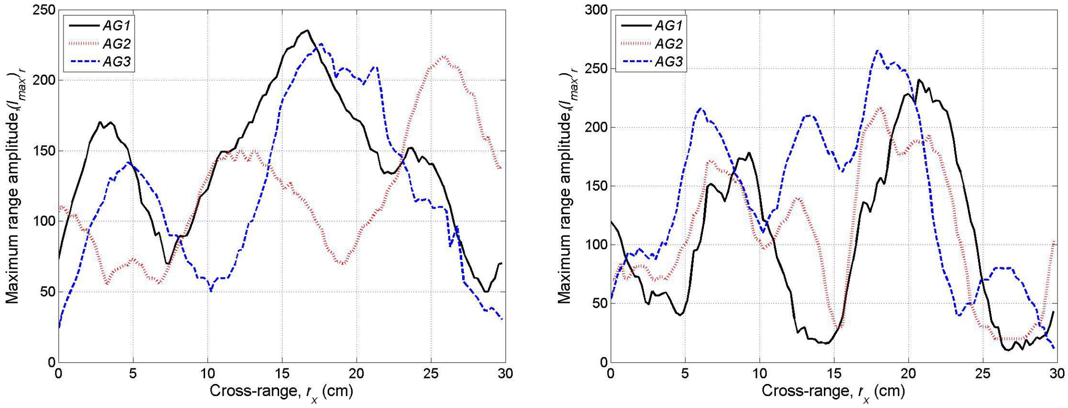

(a) *MB1* (b) *MB2*

Figure A-28: Maximum cross-range amplitude slice of 14-day mortar bars scanned in horizontal orientation.

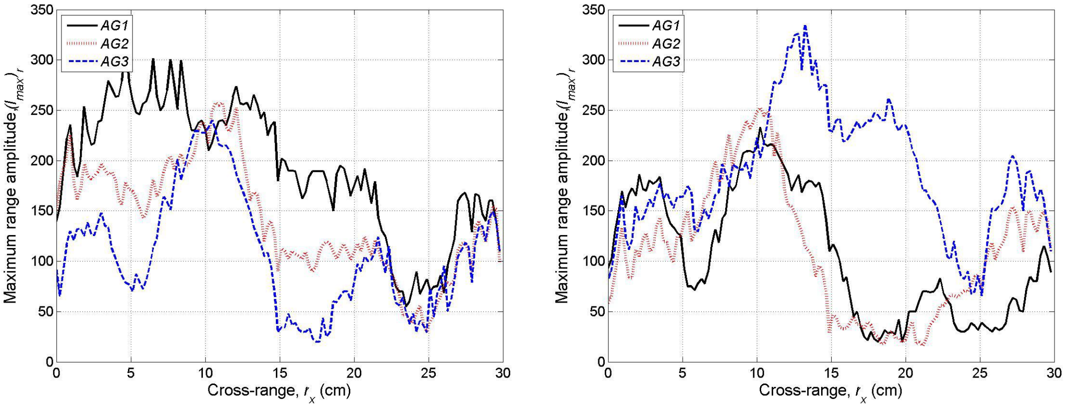

(a) *MB1*

(b) *MB2*

Figure A-29: Maximum cross-range amplitude slice of 21-day mortar bars scanned in horizontal orientation.

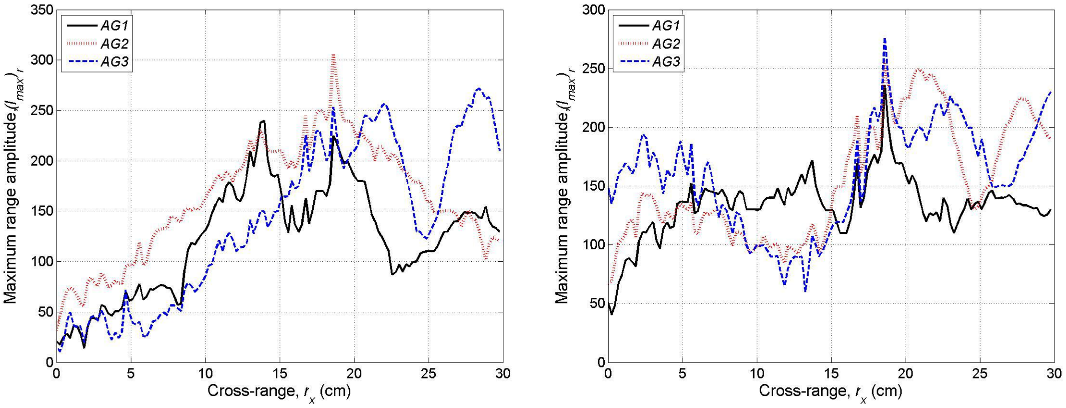

(a) *MB1*

(b) *MB2*

Figure A-30: 28-day mortar bars scanned in horizontal orientation.

A.6 Maximum Range Amplitude Slice

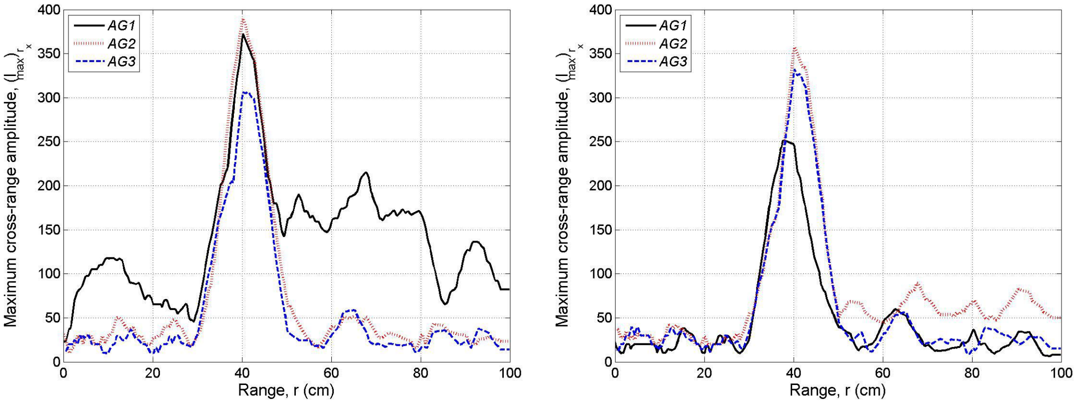

(a) *MB1* (b) *MB2*

Figure A-31: Maximum range amplitude slice of 7-day mortar bars scanned in vertical orientation.

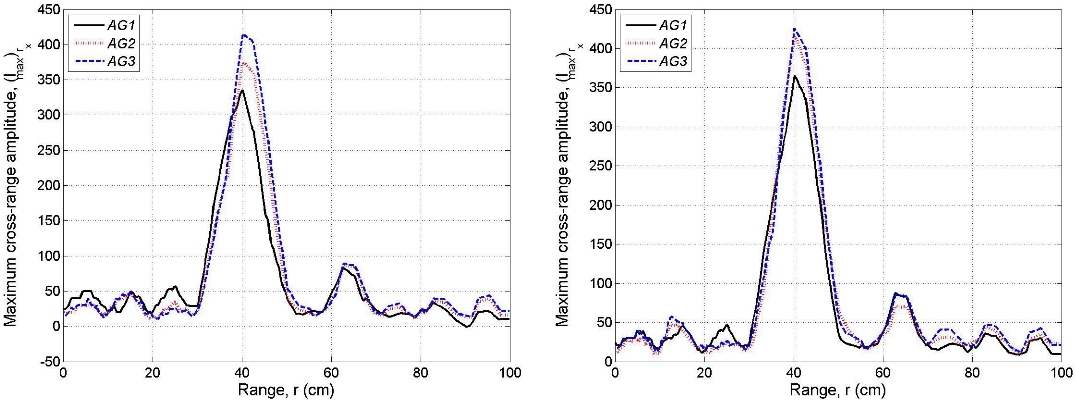

(a) *MB1* (b) *MB2*

Figure A-32: Maximum range amplitude slice of 14-day mortar bars scanned in vertical orientation.

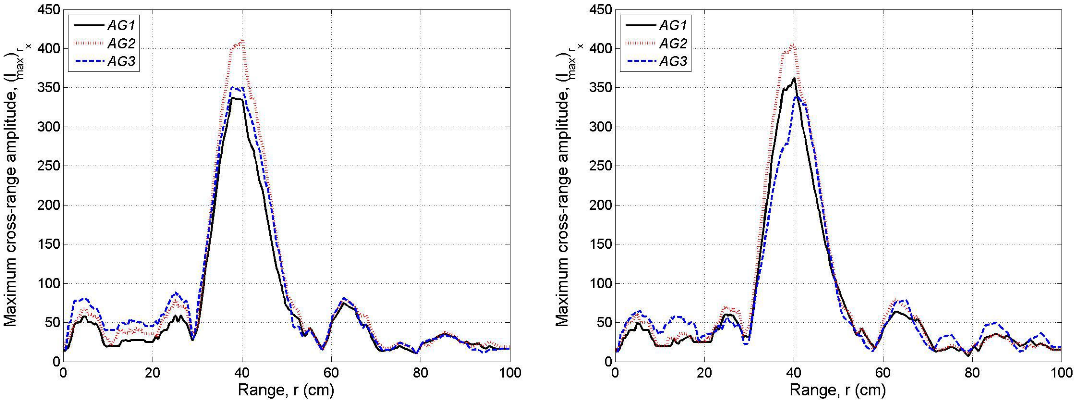

(a) *MB1* (b) *MB2*

Figure A-33: Maximum range amplitude slice of 21-day mortar bars scanned in vertical orientation.

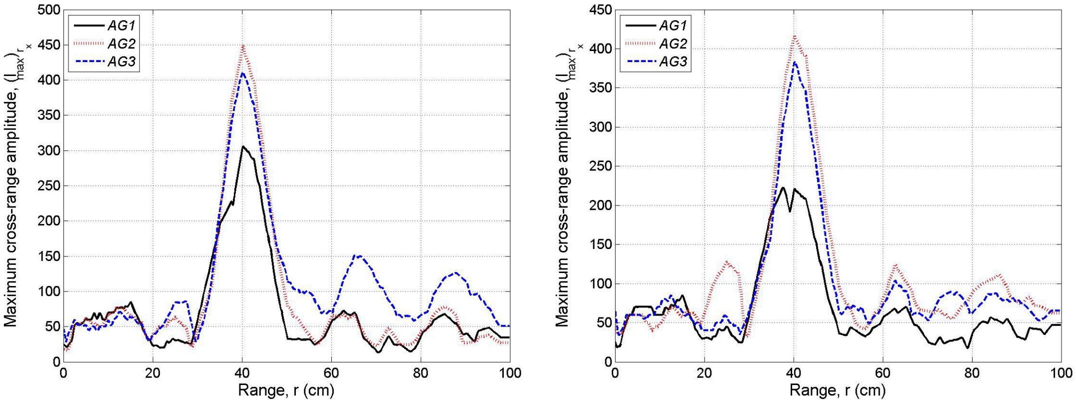

(a) *MB1* (b) *MB2*

Figure A-34: Maximum range amplitude slice of 28-day mortar bars scanned in vertical orientation.

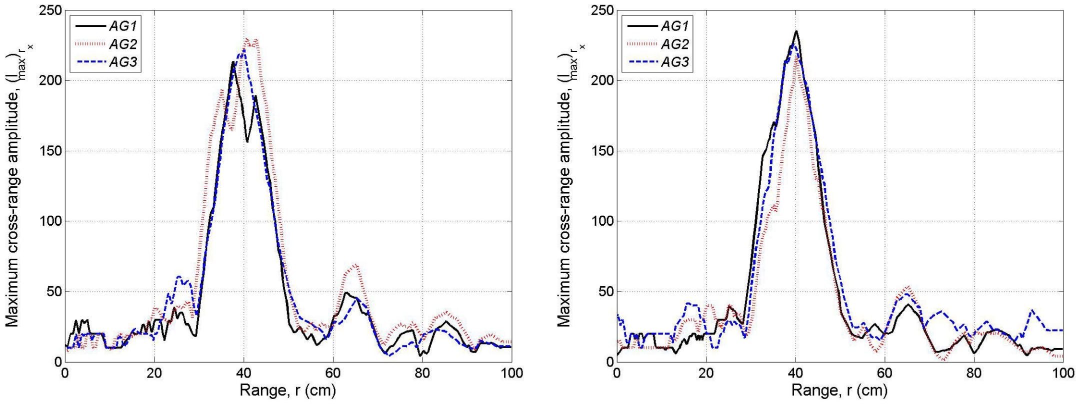

(a) *MB1* (b) *MB2*

Figure A-35: Maximum range amplitude slice of 7-day mortar bars scanned in horizontal orientation.

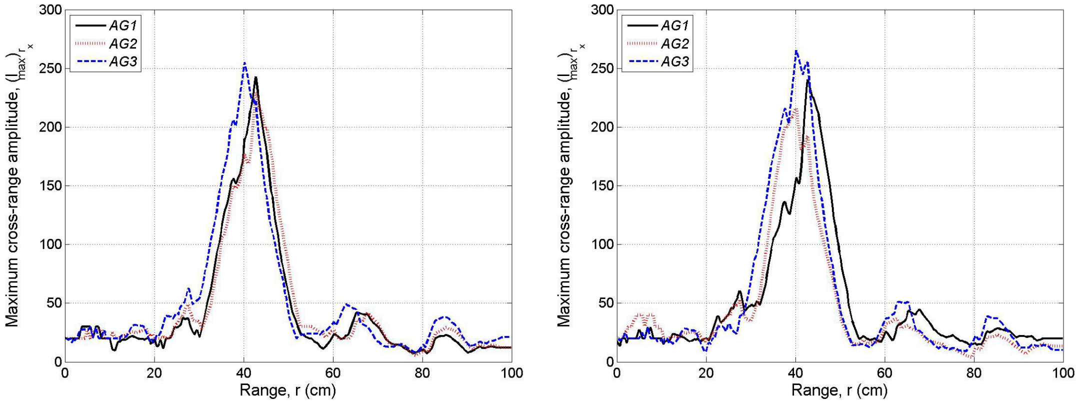

(a) *MB1* (b) *MB2*

Figure A-36: Maximum range amplitude slice of 14-day mortar bars scanned in horizontal orientation.

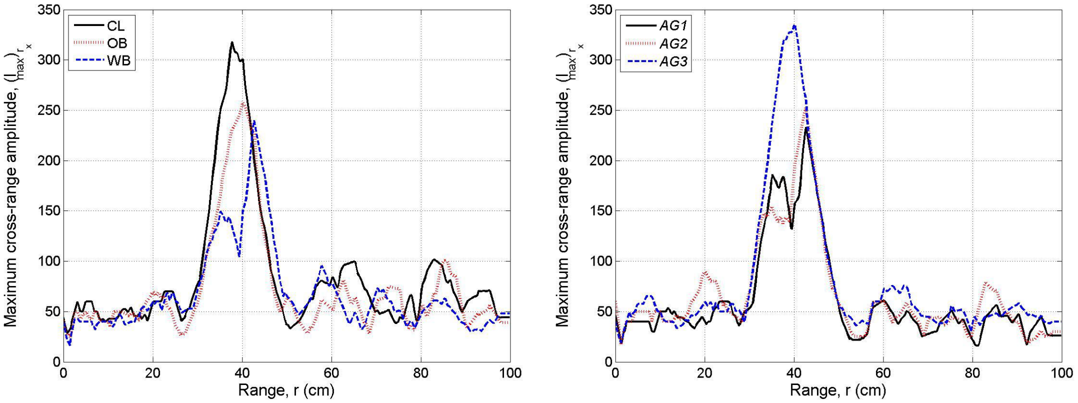

(a) *MB1* (b) *MB2*

Figure A-37: Maximum range amplitude slice of 21-day mortar bars scanned in horizontal orientation.

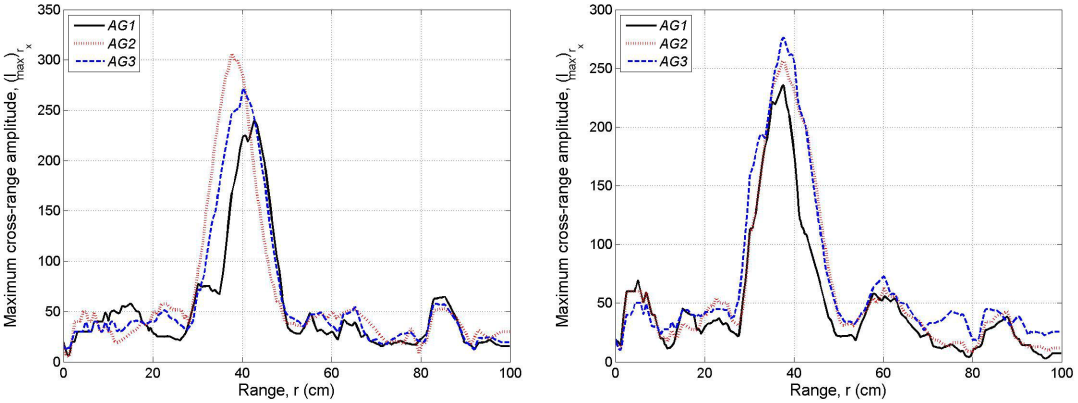

(a) *MB1* (b) *MB2*

Figure A-38: Maximum range amplitude slice of 28-day mortar bars scanned in horizontal orientation.

A.7 Average Cross-range Amplitude Slice

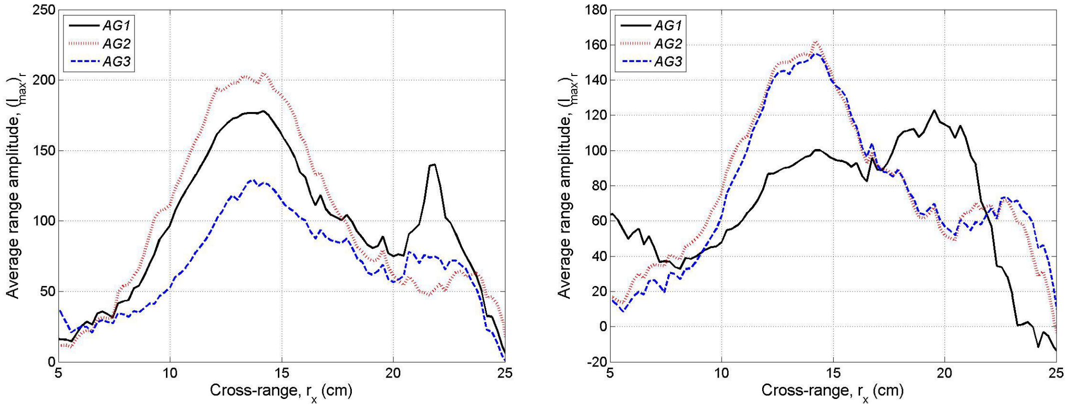

(a) *MB1* (b) *MB2*

Figure A-39: Average cross-range amplitude slice of 7-day mortar bars scanned in vertical orientation.

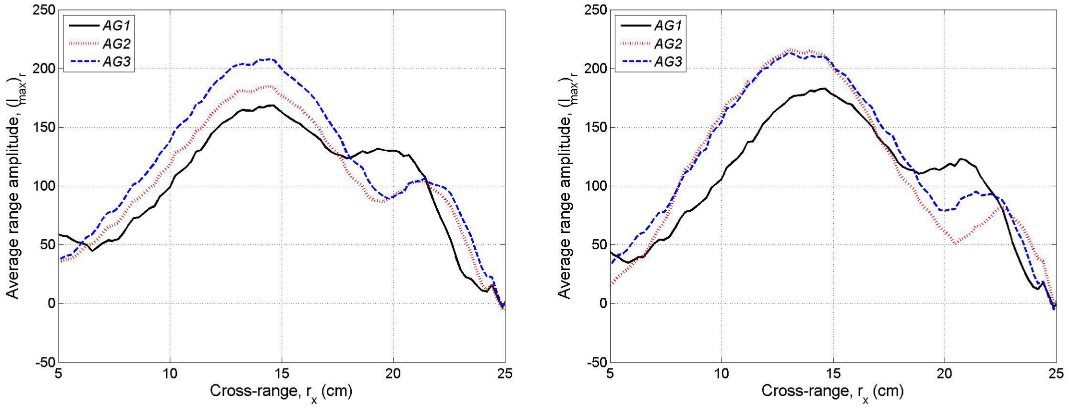

(a) *MB1* (b) *MB2*

Figure A-40: Average cross-range amplitude slice of 14-day mortar bars scanned in vertical orientation.

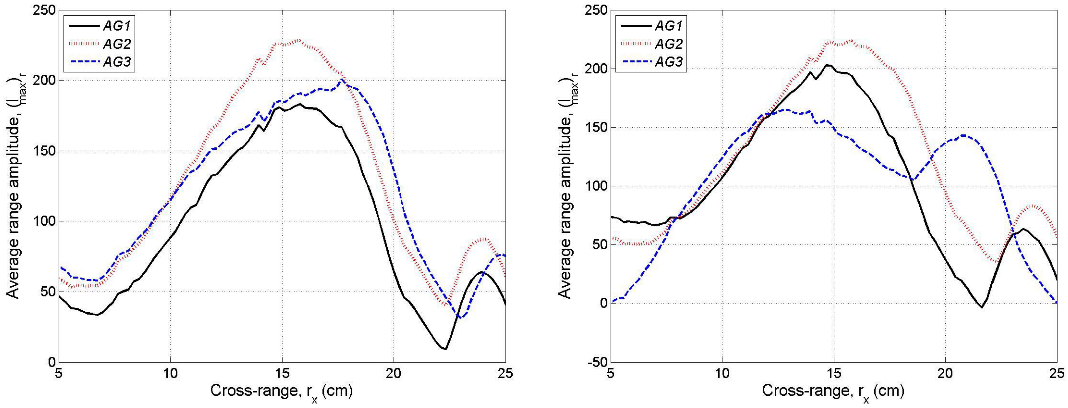

(a) *MB1* (b) *MB2*

Figure A-41: Average cross-range amplitude slice of 21-day mortar bars scanned in vertical orientation.

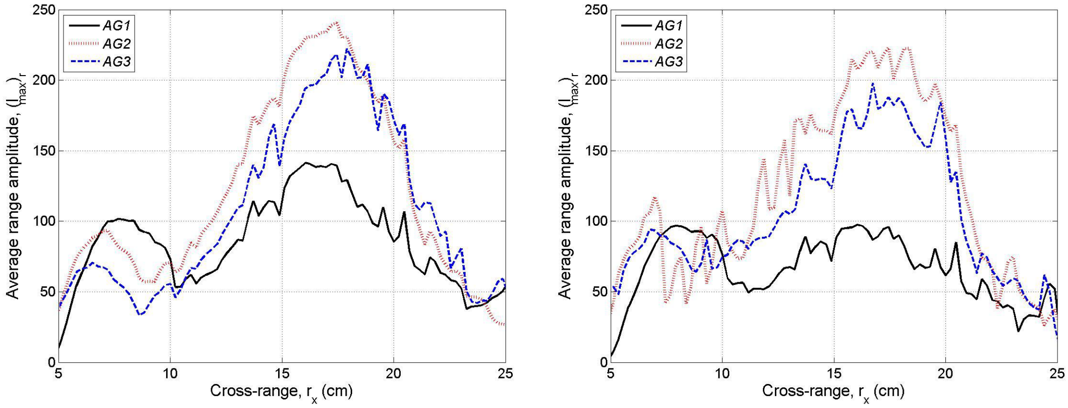

(a) *MB1* (b) *MB2*

Figure A-42: Average cross-range amplitude slice of 28-day mortar bars scanned in vertical orientation.

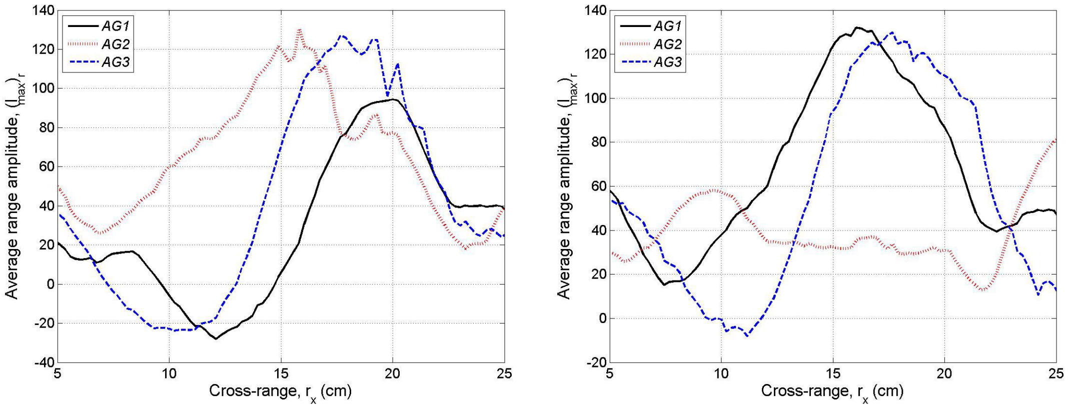

(a) *MB1*

(b) *MB2*

Figure A-43: Average cross-range amplitude slice of 7-day mortar bars scanned in horizontal orientation.

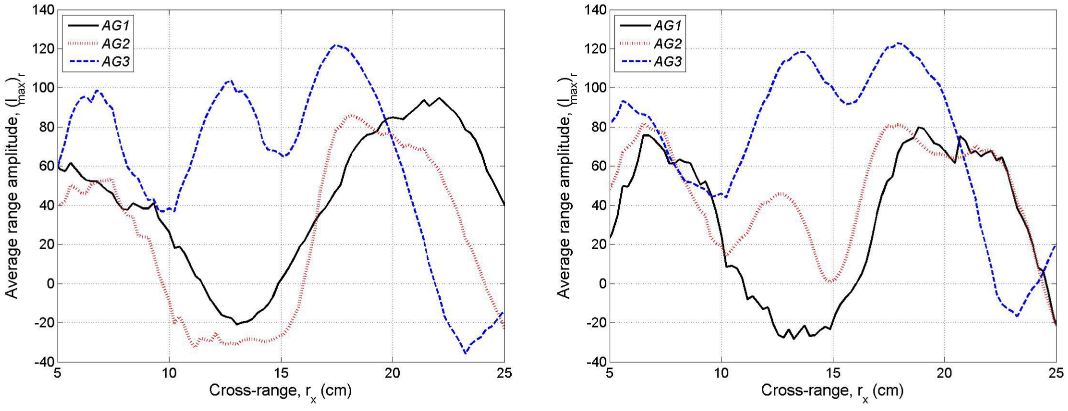

(a) *MB1*

(b) *MB2*

Figure A-44: Average cross-range amplitude slice of 14-day mortar bars scanned in horizontal orientation.

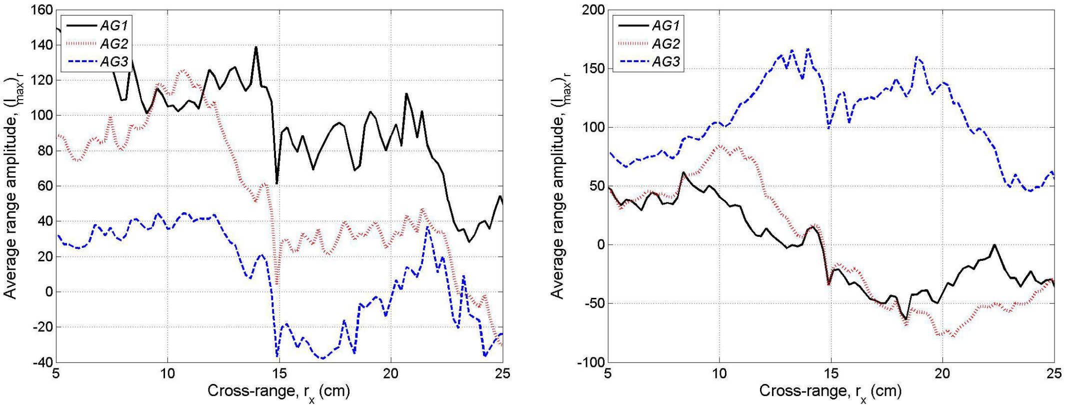

(a) *MB1* (b) *MB2*

Figure A-45: Average cross-range amplitude slice of 21-day mortar bars scanned in horizontal orientation.

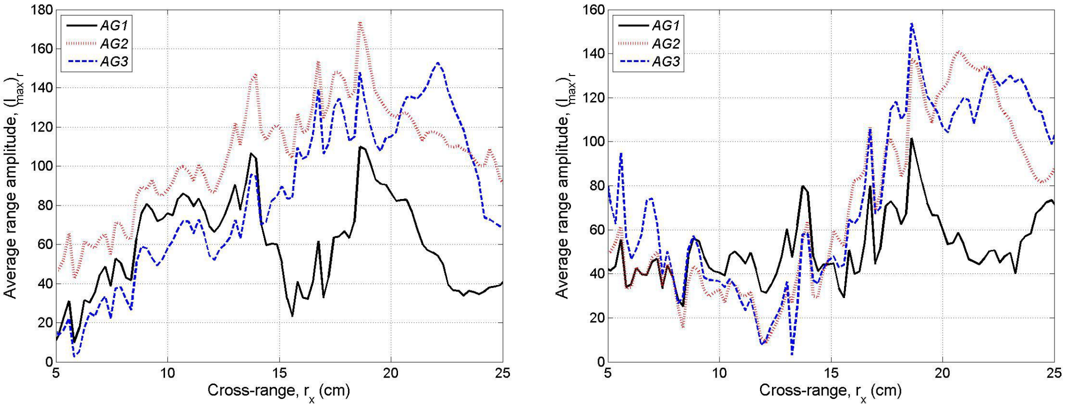

(a) *MB1* (b) *MB2*

Figure A-46: Average cross-range amplitude slice of 28-day mortar bars scanned in horizontal orientation.

A.8 Average Range Amplitude Slice

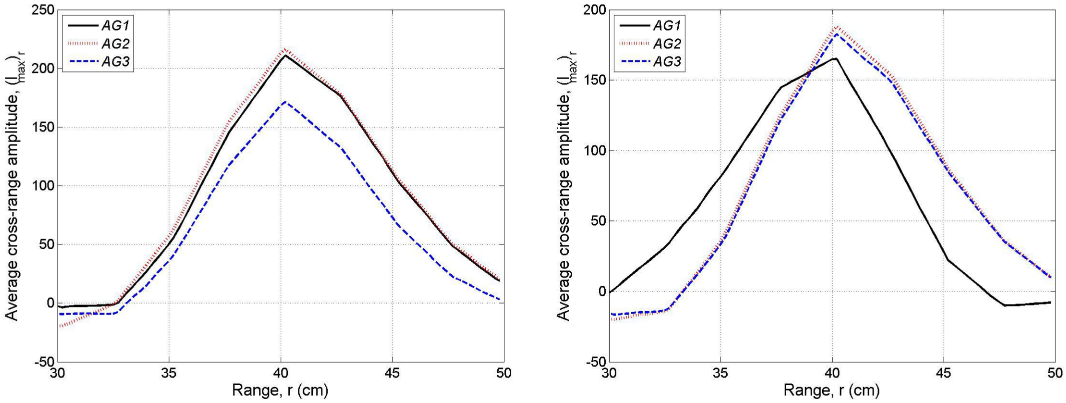

(a) *MB1* (b) *MB2*

Figure A-47: Average range amplitude slice of 7-day mortar bars scanned in vertical orientation.

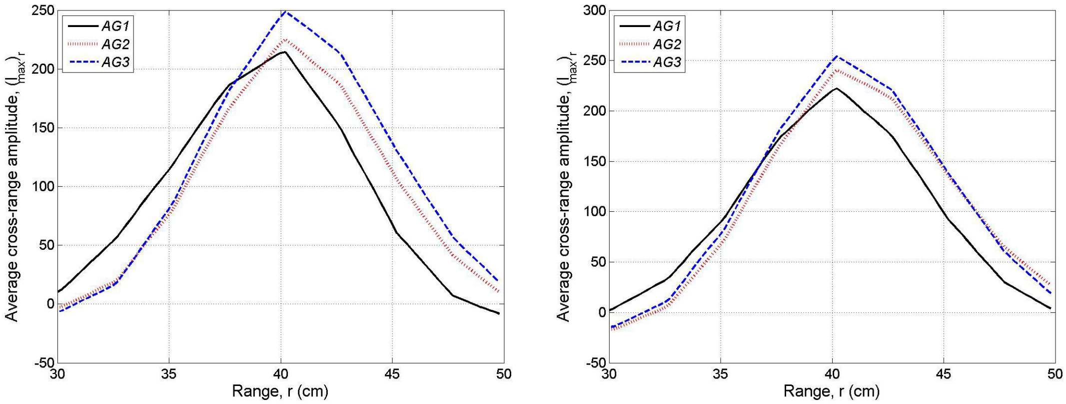

(a) *MB1* (b) *MB2*

Figure A-48: Average range amplitude slice of 14-day mortar bars scanned in vertical orientation.

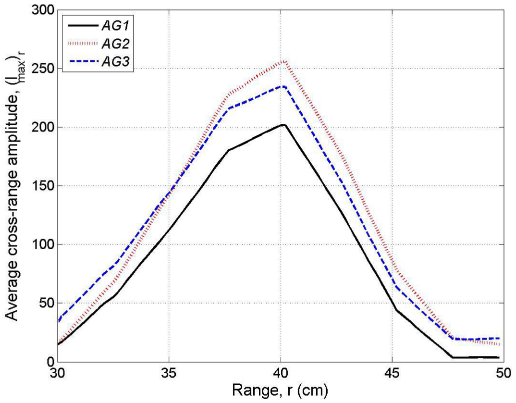

(a) *MB1* (b) *MB2*

Figure A-49: Average range amplitude slice of 21-day mortar bars scanned in vertical orientation.

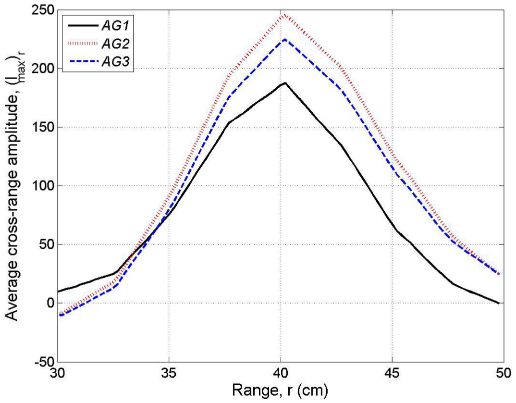

(a) *MB1* (b) *MB2*

Figure A-50: Average range amplitude slice of 28-day mortar bars scanned in vertical orientation.

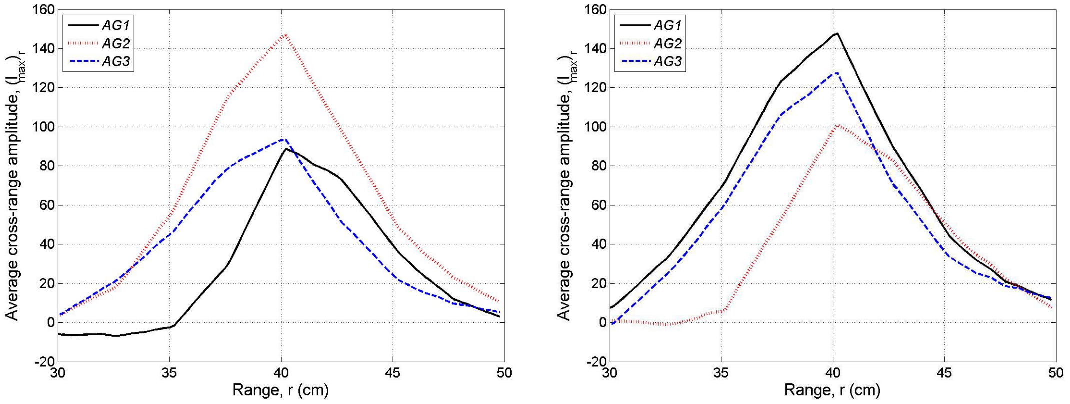

(a) *MB1* (b) *MB2*

Figure A-51: Average range amplitude slice of 7-day mortar bars scanned in horizontal orientation.

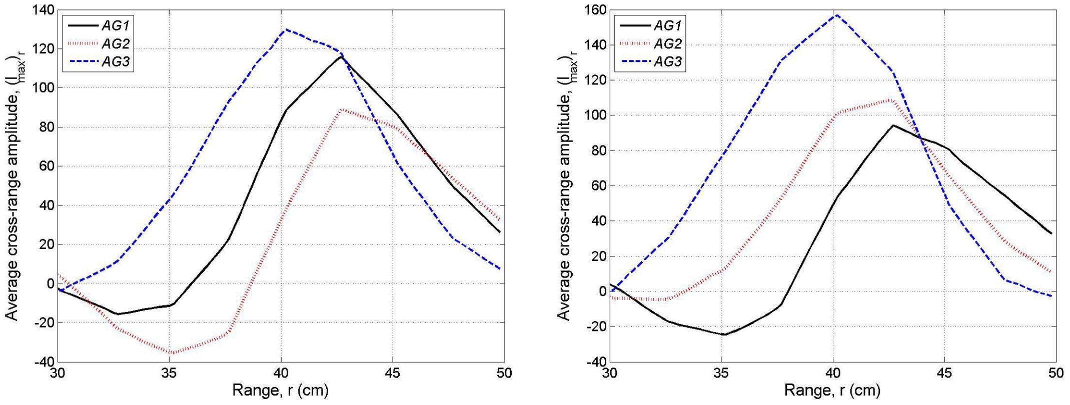

(a) *MB1* (b) *MB2*

Figure A-52: Average range amplitude slice of 14-day mortar bars scanned in horizontal orientation.

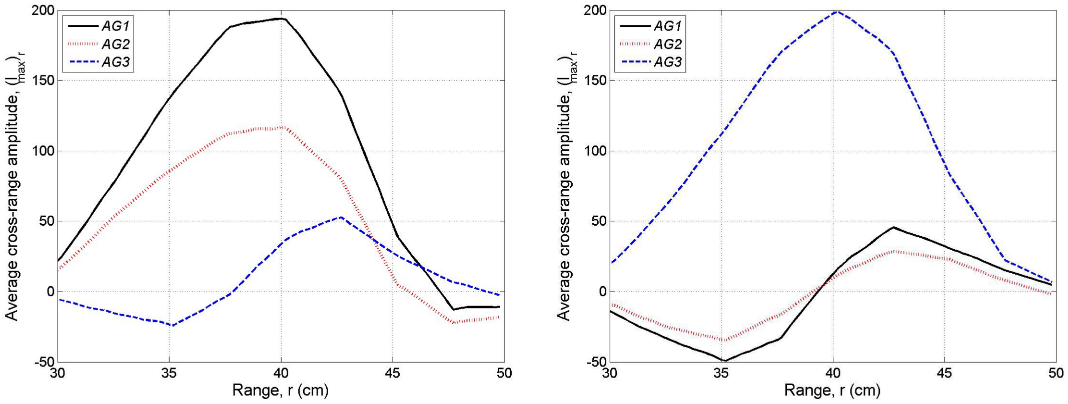

(a) *MB1* (b) *MB2*

Figure A-53: Average range amplitude slice of 21-day mortar bars scanned in horizontal orientation.

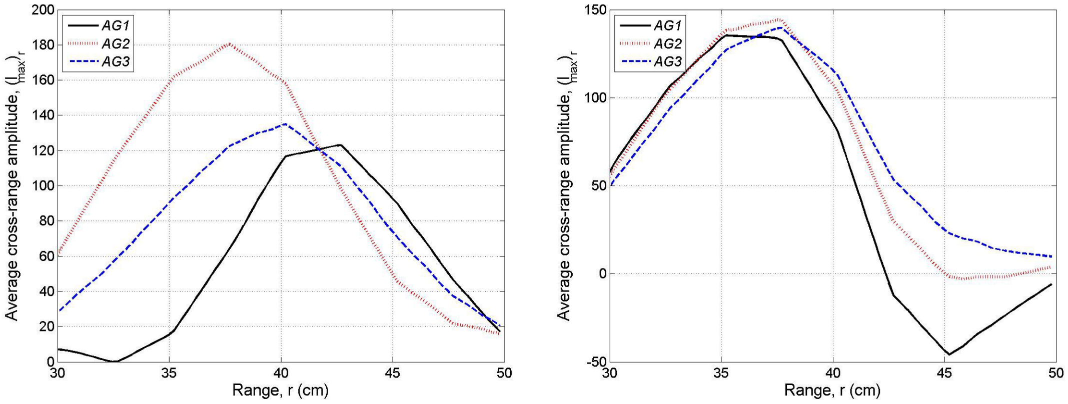

(a) *MB1* (b) *MB2*

Figure A-54: Average range amplitude slice of 28-day mortar bars scanned in horizontal orientation.

A.9 Dielectric Constant Curves within 0.98 GHz and 4.50 GHz

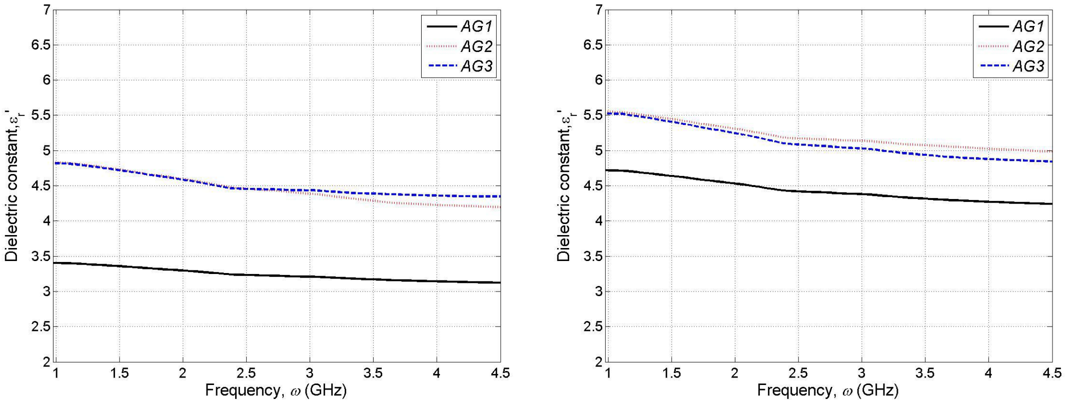

(a) *MB1*　(b) *MB2*

Figure A-55: Dielectric constant curves of 7-day mortar bars.

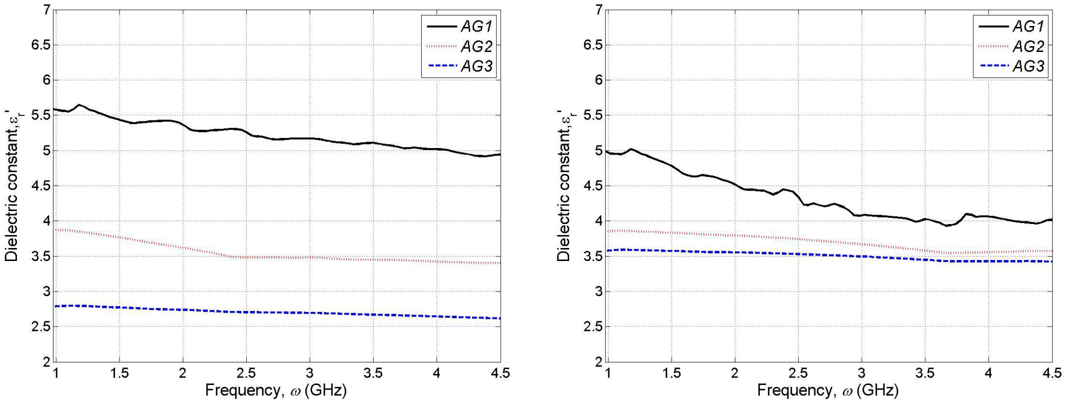

(a) *MB1*　(b) *MB2*

Figure A-56: Dielectric constant curves of 14-day mortar bars.

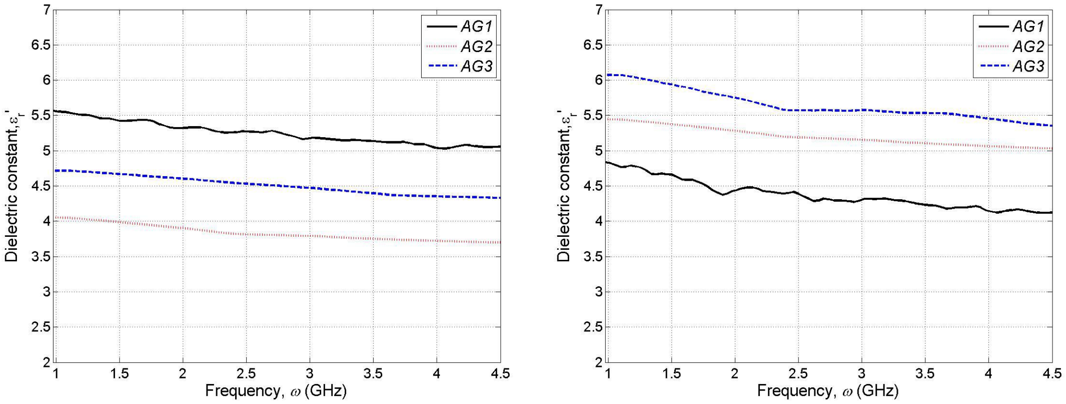

(a) *MB1* (b) *MB2*

Figure A-57: Dielectric constant curves of 21-day mortar bars.

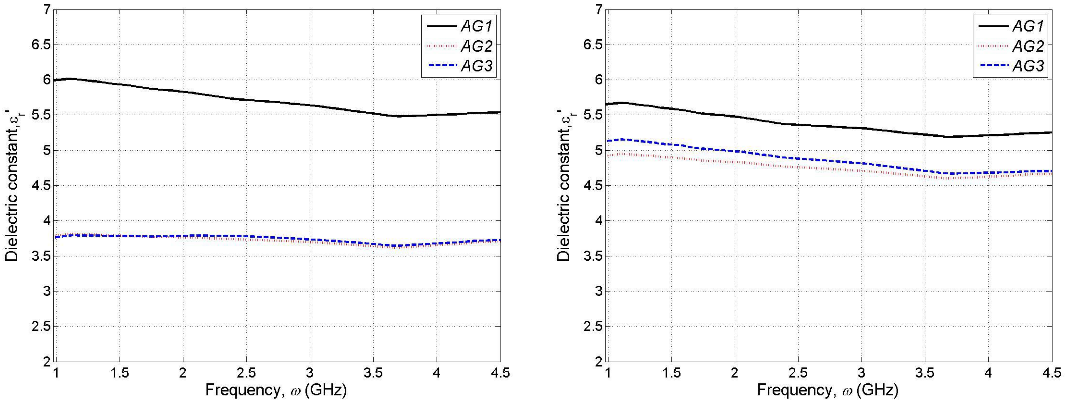

(a) *MB1* (b) *MB2*

Figure A-58: Dielectric constant curves of 28-day mortar bars.

A.10 Dielectric Constant Modeling

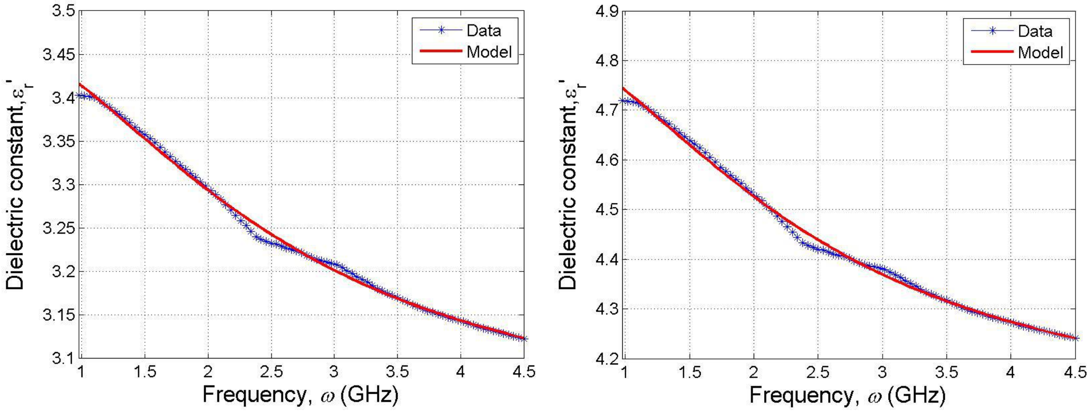

(a) *MB1* (b) *MB2*

Figure A-59: Dielectric constant modeling of *AG1*, 7-day mortar bars.

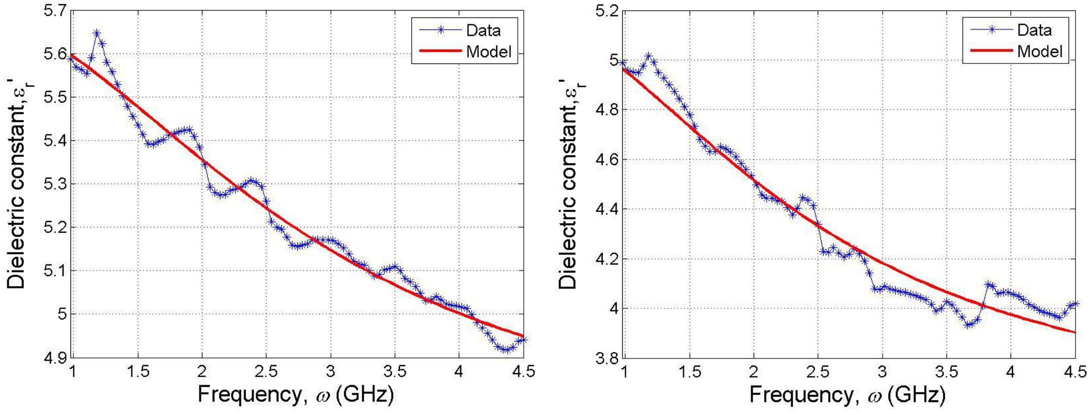

(a) *MB1* (b) *MB2*

Figure A-60: Dielectric constant modeling of *AG1*, 14-day mortar bars.

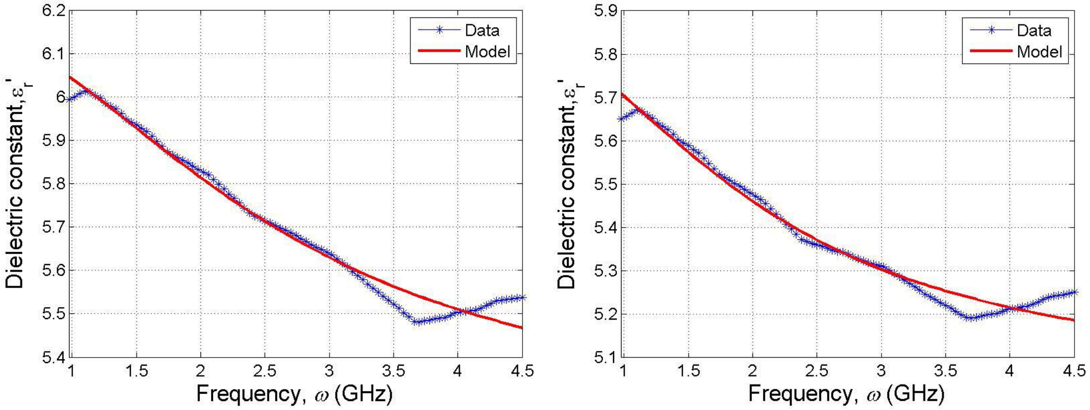

(a) *MB1*　　(b) *MB2*

Figure A-62: Dielectric constant modeling of *AG1*, 28-day mortar bars.

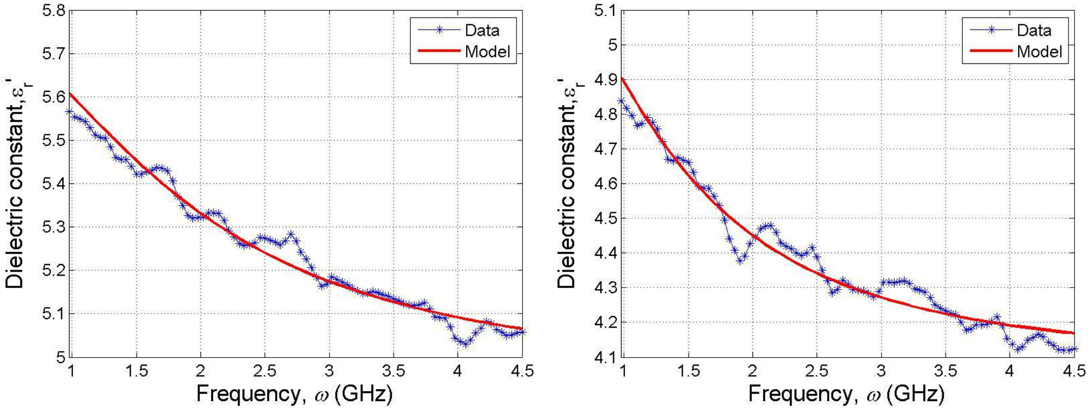

(a) *MB1*　　(b) *MB2*

Figure A-61: Dielectric constant modeling of *AG1*, 21-day mortar bars.

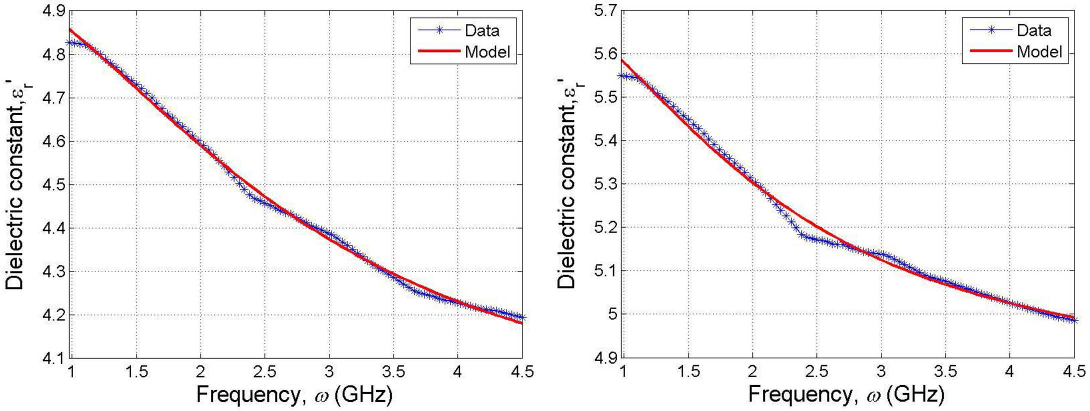

(a) *MB1*　　(b) *MB2*

Figure A-63: Dielectric constant modeling of *AG2*, 7-day mortar bars.

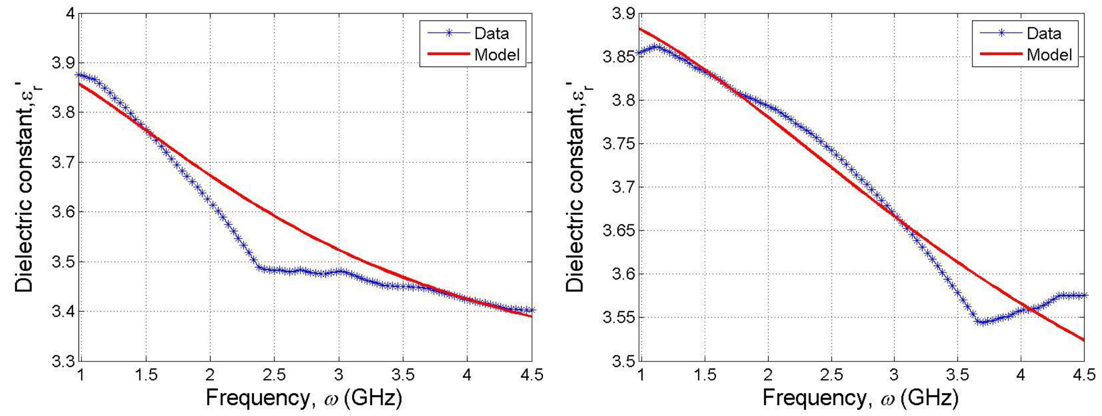

(a) *MB1* (b) *MB2*

Figure A-64: Dielectric constant modeling of *AG2*, 14-day mortar bars.

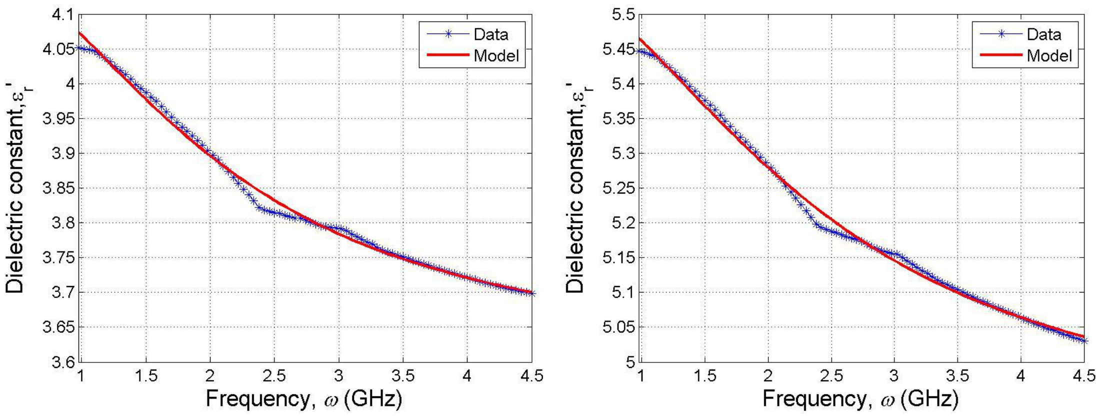

(a) *MB1* (b) *MB2*

Figure A-65: Dielectric constant modeling of *AG2*, 21-day mortar bars.

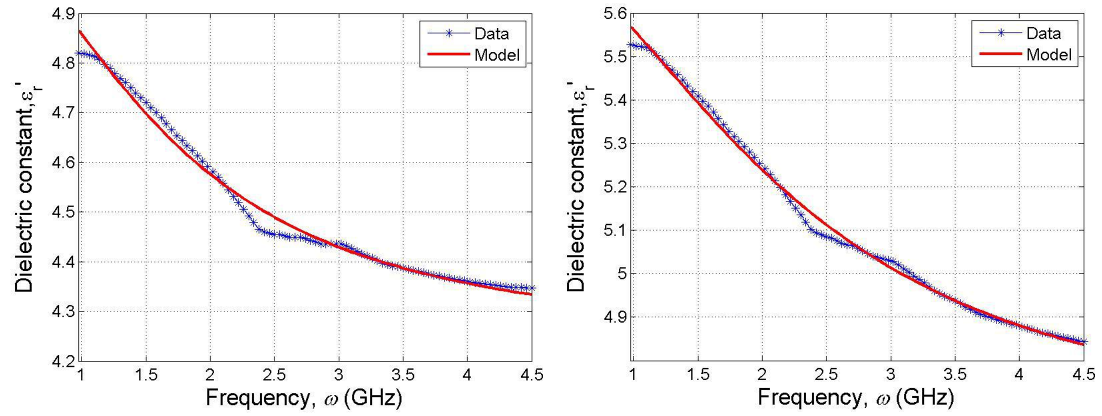

(a) *MB1* (b) *MB2*

Figure A-67: Dielectric constant modeling of *AG3*, 7-day mortar bars.

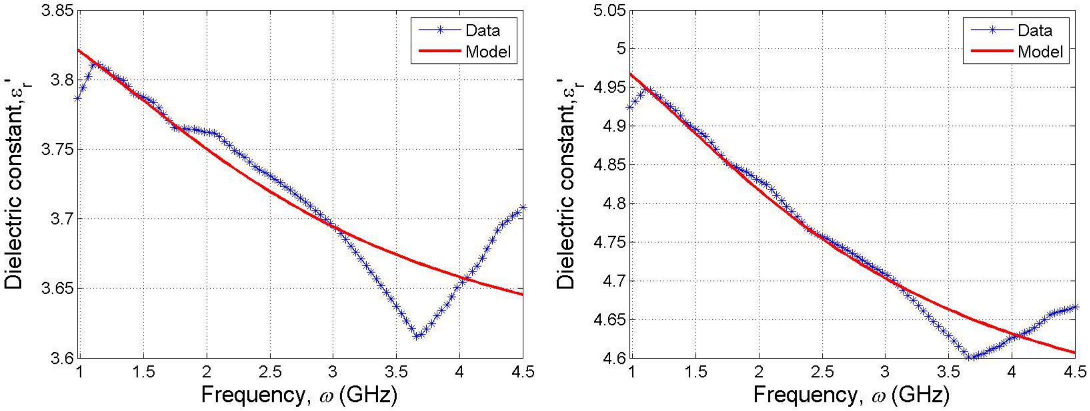

(a) *MB1* (b) *MB2*

Figure A-66: Dielectric constant modeling of *AG2*, 28-day mortar bars.

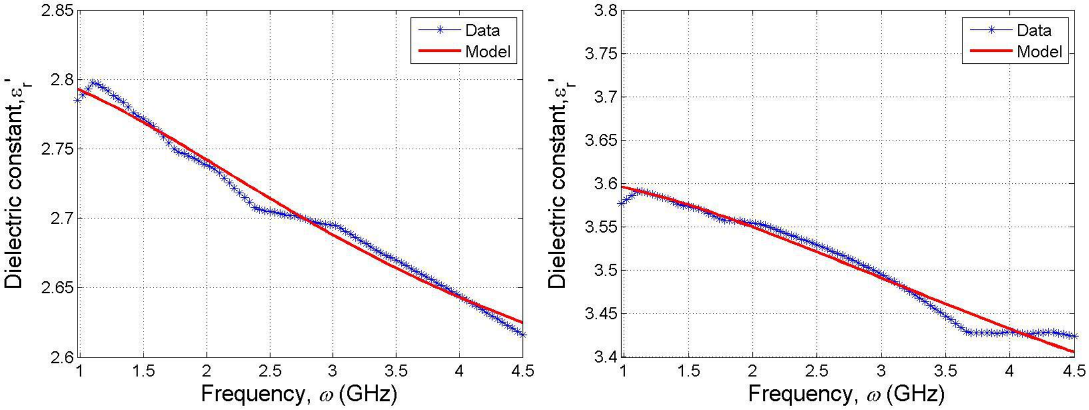

(a) *MB1* (b) *MB2*

Figure A-68: Dielectric constant modeling of *AG3*, 14-day mortar bars.

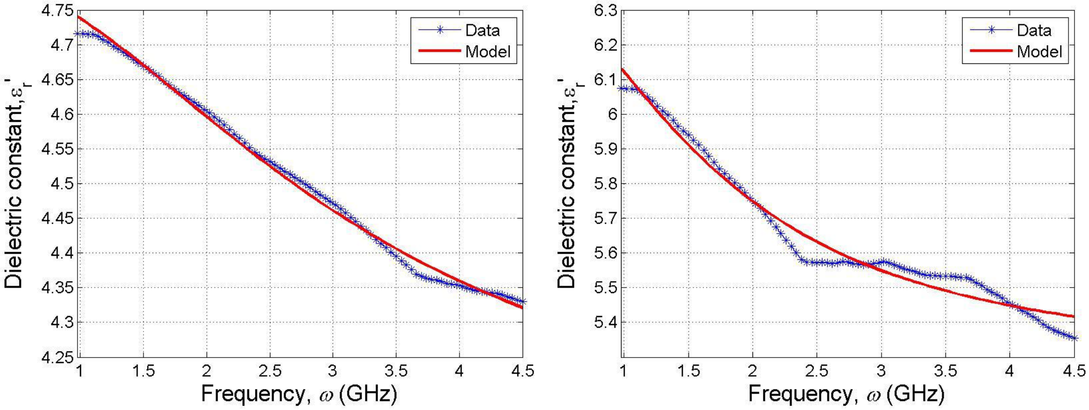

(a) *MB1* (b) *MB2*

Figure A-69: Dielectric constant modeling of *AG3*, 21-day mortar bars.

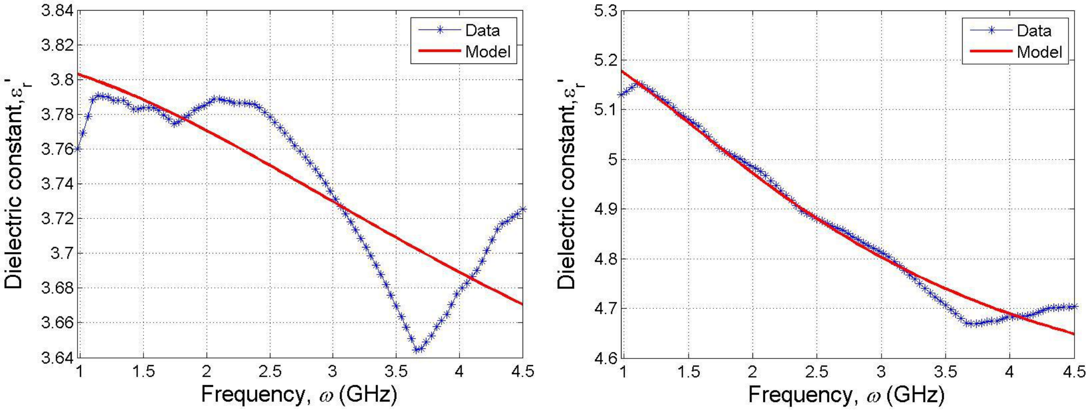

(a) *MB1* (b) *MB2*

Figure A-70: Dielectric constant modeling of *AG3*, 28-day mortar bars.

Bibliography

[1] M. Thomas, B. Fournier, K. Folliard, and Y. Resendez, "Alkali-silica reactivity field identification handbook," tech. rep., 2011.

[2] O. Bayrak, "Structural implications of ASR: State of the art," tech. rep., MPR Associates Inc., 2012.

[3] T. Ahmed, E. Burley, S. Rigden, and A. I. Abu-Tair, "The effect of alkali reactivity on the mechanical properties of concrete," *Construction and Building Materials*, vol. 17, no. 2, pp. 123–144, 2003.

[4] T.-Y. Yu, *Damage Detection of GFRP-Concrete Systems Using Electromagnetic Waves: Theory and Experiment.* LAP LAMBERT Academic Publishing, 2010.

[5] ASTM Standard C597, "Standard test method for pulse velocity through concrete." West Conshohocken, PA.

[6] I. Solak, "Determination of dielectric constants of hydrated cement paste and cement mortar using a contact coaxial probe," Master's thesis, Department of Civil and Environmental Engineering, University of Massachusetts Lowell, 2011.

[7] V. Le, T. Yu, J. O. Twumasi, and Q. Tang, "Sizing and ranging criteria for SAR images of steel and wood specimens," *Proceedings of SPIE*, 2016.

[8] ASTM Standard C1260, *Standard Test Method for Potential Alkali Reactivity of Aggregates (Mortar-Bar Method).* West Conshohocken, PA.

[9] T. E. Stanton, "Expansion of concrete through reaction between cement and aggregate," *Proceedings of the American Society of Civil Engineers*, vol. 66, 1940.

[10] R. Vayda, J. Simons, J. Moroney, O. Bayrak, R. Keating, and T. Roberts, "Seabrook station: Impact of alkali-silica reaction on concrete structures and attachments," tech. rep., MPR Associates Inc., 2012.

[11] S. Kharkovsky, J. T. Case, M. T. Ghasr, R. Zoughi, S. W. Bae, and A. Belarbi, "Application of microwave 3D SAR imaging technique for evaluation of

corrosion in steel rebars embedded in cement-based structures," *AIP Conference Proceedings*, vol. 1430, no. 1, pp. 1516–1523, 2012.

[12] C.-P. Lai, Y.-J. Ren, and T. Y. Yu, "Scanning array radar system for bridge subsurface imaging," *Proceedings of SPIE*, vol. 8347, p. 834713, 2013.

[13] T. Yu, "Distant damage-assessment method for multilayer composite systems using electromagnetic waves," *Journal of Engineering Mechanics (ASCE)*, vol. 137, no. 8, pp. 547–560, 2011.

[14] T. Yu, C.-F. Su, C.-P. Lai, and H. F. Wu, "Wideband subsurface radar for bridge structural health monitoring and nondestructive evaluation," *Proceedings of SPIE*, vol. 8694, p. 86940I, 2013.

[15] S. Chatterji, "Chemistry of alkali–silica reaction and testing of aggregates," *Cement and Concrete Composites*, vol. 27, no. 7, pp. 788–795, 2005.

[16] S. Diamond, R. Barneyback Jr, and L. Struble, "Physics and chemistry of alkali-silica reactions," tech. rep., Purdue Univ., Lafayette, IN (USA), 1981.

[17] D. W. Hobbs, *Alkali-silica reaction in concrete.* Telford, London, 1988.

[18] K. J. Folliard, R. Barborak, T. Drimalas, L. Du, S. Garber, J. Ideker, T. Ley, S. Williams, M. Juenger, B. Fournier, *et al.*, "Preventing ASR/DEF in new concrete," tech. rep., Texas Department of Transportation, 2006.

[19] Š. Šachlová, "Microstructure parameters affecting alkali–silica reactivity of aggregates," *Construction and Building Materials*, vol. 49, pp. 604–610, 2013.

[20] W. E. Touma, D. Fowler, and R. Carrasquillo, "Alkali-silica reaction in portland cement concrete: testing methods and mitigation alternatives," tech. rep., Aggregates Foundation for Technology, Research, and Education, 2001.

[21] B. Fournier, M.-A. Berube, K. J. Folliard, and M. Thomas, "Report on the diagnosis, prognosis, and mitigation of alkali-silica reaction (ASR) in transportation structures," tech. rep., U.S. Department of Transportation: Federal Highway Administration, 2010.

[22] L.-O. Nilsson, "Moisture effects on the alkali-silica reaction," *Proceedings 6th International Conference on AAR in Concrete*, pp. 201–208, 1983.

[23] M. Ozol, "The pessimum proportion as a reference point in modulating alkali-silica reaction," *Proceedings of a Symposium on Alkali–Aggregate Reaction, Preventive Measures*, pp. 113–130, 1975.

[24] T. Ichikawa, "Alkali–silica reaction, pessimum effects and pozzolanic effect," *Cement and Concrete Research*, vol. 39, no. 8, pp. 716–726, 2009.

[25] ASTM Standard C1293, "Test method for determination of length change of concrete due to alkali-silica reaction." West Conshohocken, PA.

[26] ASTM Standard C295, "Standard guide for petrographic examination of aggregates for concrete." West Conshohocken, PA.

[27] P. Rivard and G. Ballivy, "Assessment of the expansion related to alkali-silica reaction by the damage rating index method," *Construction and Building Materials*, vol. 19, no. 2, pp. 83–90, 2005.

[28] P. Rivard and F. Saint-Pierre, "Assessing alkali-silica reaction damage to concrete with non-destructive methods: From the lab to the field," *Construction and Building Materials*, vol. 23, no. 2, pp. 902–909, 2009.

[29] M. Sargolzahi, S. A. Kodjo, P. Rivard, and J. Rhazi, "Effectiveness of non-destructive testing for the evaluation of alkali–silica reaction in concrete," *Construction and Building Materials*, vol. 24, no. 8, pp. 1398–1403, 2010.

[30] K. Kurtis, P. Monteiro, J. Brown, and W. Meyer-Ilse, "High resolution transmission soft x-ray microscopy of deterioration products developed in large concrete dams," *Journal of Microscopy*, vol. 196, pp. 288–298, 1999.

[31] C. Collins, J. Ideker, and K. Kurtis, "Laser scanning confocal microscopy for in situ monitoring of alkali–silica reaction," *Journal of Microscopy*, vol. 213, no. 2, pp. 149–157, 2004.

[32] E. Schmidt, "A non-destructive concrete tester," *Concrete*, vol. 59, no. 8, pp. 34–35, 1951.

[33] J. Krautkrämer and H. Krautkrämer, *Ultrasonic testing of materials.* Springer Science & Business Media, 2013.

[34] K. J. Lesnicki, J.-Y. Kim, K. E. Kurtis, and L. J. Jacobs, "Accelerated determination of ASR susceptibility during concrete prism testing through nonlinear resonance acoustic spectroscopy," tech. rep., U. S. Department of Transportation: Federal Highway Administration, 2013.

[35] P. Gong, M. E. Patton, C. Liu, I. J. Oppenheim, D. W. Greve, J. B. Harley, and W. R. Junker, "Ultrasonic detection of the alkali-silica reaction damage in concrete," in *Ultrasonics Symposium (IUS), 2014 IEEE International*, pp. 361–364, IEEE, 2014.

[36] J. Chen, K. Lesnicki, K. Kurtis, J. Kim, L. Jacobs, D. O. Thompson, and D. E. Chimenti, "NDT techniques for characterizing alkali-silica reaction in standard concrete specimens-a review," in *AIP Conference Proceedings-American Institute of Physics*, no. 1, p. 1275, 2011.

[37] J. Chen, A. R. Jayapalan, J.-Y. Kim, K. E. Kurtis, and L. J. Jacobs, "Nonlinear wave modulation spectroscopy method for ultra-accelerated alkali-silica reaction assessment," *ACI Materials Journal*, vol. 106, no. 4, p. 340, 2009.

[38] K. J. Leśnicki, J.-Y. Kim, K. E. Kurtis, and L. J. Jacobs, "Characterization of ASR damage in concrete using nonlinear impact resonance acoustic spectroscopy technique," *NDT & E International*, vol. 44, no. 8, pp. 721–727, 2011.

[39] F. Moradi-Marani, S. A. Kodjo, P. Rivard, and C.-P. Lamarche, "Nonlinear acoustic technique of time shift for evaluation of alkali-silica reaction damage in concrete structures," *ACI Materials Journal*, vol. 111, no. 5, pp. 581–592, 2014.

[40] D. Lane and H. Ozyildirim, "Use of fly ash, slag, or silica fume to inhibit alkali-silica reactivity," tech. rep., Virginia Transportation Research Council, Charlottesville, VA (United States), 1995.

[41] M. H. Shehata and M. D. Thomas, "The effect of fly ash composition on the expansion of concrete due to alkali–silica reaction," *Cement and Concrete Research*, vol. 30, no. 7, pp. 1063–1072, 2000.

[42] C. Yi and C. Ostertag, "Mechanical approach in mitigating alkali-silica reaction," *Cement and concrete research*, vol. 35, no. 1, pp. 67–75, 2005.

[43] C. Collins, J. Ideker, G. Willis, and K. Kurtis, "Examination of the effects of $LiOH$, $LiCl$, and $LiNO_3$ on alkali–silica reaction," *Cement and Concrete Research*, vol. 34, no. 8, pp. 1403–1415, 2004.

[44] J. A. Farny and S. H. Kosmatka, *Diagnosis and control of alkali-aggregate reactions in concrete.* Portland Cement Association, Skokie, IL, 1997.

[45] M. D. Thomas, B. Fournier, K. J. Folliard, J. H. Ideker, and Y. Resendez, "The use of lithium to prevent or mitigate alkali-silica reactions in concrete pavements and structures," tech. rep., U.S. Department of Transportation: Federal Highway Administration, 2007.

[46] L. Du, E. Lukefahr, and A. Naranjo, "Texas department of transportation fly ash database and the development of chemical composition–based fly ash alkali-silica reaction durability index," *Journal of Materials in Civil Engineering*, vol. 25, no. 1, pp. 70–77, 2012.

[47] H. T. Le, K. Siewert, and H.-M. Ludwig, "Alkali silica reaction in mortar formulated from self-compacting high performance concrete containing rice husk ash," *Construction and Building Materials*, vol. 88, pp. 10–19, 2015.

[48] R. Jones, "The application of ultrasonic to the testing of concrete," *Research, London, England*, vol. 383, pp. 364–368, 1948.

[49] J. Leslie and W. Cheesman, "An ultrasonic method of studying deterioration and cracking in concrete structures," *Journal of the American Concrete Institute*, vol. 21, no. 1, pp. 17–36, 1949.

[50] W. Cheesman and W. Arndt, "Dynamic testing of concrete with the soniscope apparatus," *Highway Research Board Proceedings*, vol. 29, 1950.

[51] R. N. Swamy and M. Al-Asali, "Control of alkali-silica reaction in reinforced concrete beams," *Materials Journal*, vol. 87, no. 1, pp. 38–46, 1990.

[52] R. Swamy, *The Alkali-Silica Reaction in Concrete.* Taylor & Francis, 1991.

[53] A. Annan, "Chapter 1 - electromagnetic principles of ground penetrating radar," in *Ground Penetrating Radar Theory and Applications* (H. M. Jol, ed.), pp. 1 – 40, Amsterdam: Elsevier, 2009.

[54] C. V. Jakowatz, D. E. Wahl, P. H. Eichel, D. C. Ghiglia, and P. A. Thompson, *Spotlight-Mode Synthetic Aperture Radar: A Signal Processing Approach.* Springer Science & Business Media, 2012.

[55] M. Soumekh, *Synthetic aperture radar signal processing.* New York: Wiley, 1999.

[56] T.-Y. Yu, "Determining the optimal parameters in a distant radar nde technique for debonding detection of gfrp-concrete systems," *Proceedings of SPIE*, vol. 7294, p. 72940S, 2009.

[57] A. Yegulalp, "Fast backprojection algorithm for synthetic aperture radar," *Proceedings of the 1999 IEEE Radar Conference*, pp. 60–65, 1999.

[58] H. C. Rhim and O. Buyukozturk, "Electromagnetic properties of concrete at microwave frequency range," *Materials Journal*, vol. 95, no. 3, pp. 262–271, 1998.

[59] S. N. Kharkovsky, M. F. Akay, U. C. Hasar, and C. D. Atis, "Measurement and monitoring of microwave reflection and transmission properties of cement-based specimens," *IEEE Transactions on Instrumentation and Measurement*, vol. 51, no. 6, pp. 1210–1218, 2002.

[60] G. De Loor, "The effect of moisture on the dielectric constant of hardened portland cement paste," *Applied Scientific Research, Section B*, vol. 9, no. 4-5, pp. 297–308, 1961.

[61] J. Hasted and M. Shah, "Microwave absorption by water in building materials," *British Journal of Applied Physics*, vol. 15, no. 7, p. 825, 1964.

[62] H. Liu, "Dielectric modeling of hydrated cement paste panels," Master's thesis, Department of Civil and Environmental Engineering, University of Massachusetts Lowell, 2011.

[63] J. O. Twumasi and T. Yu, "Forward and inverse dielectric modeling of oven-dried cement paste specimens in the frequency range of 1.02 GHz to 4.50 GHz," *Proceedings of SPIE*, vol. 9437, p. 943724, 2015.

[64] P. J. W. Debye, *Polar molecules.* Chemical Catalog Company, Inc., 1929.

[65] K. Donnell, R. Zoughi, and K. Kurtis, “Demonstration of microwave method for detection of alkali–silica reaction (ASR) gel in cement-based materials,” *Cement and Concrete Research*, vol. 44, pp. 1–7, 2013.

[66] K. Donnell, S. Hatfield, R. Zoughi, and K. Kurtis, “Wideband microwave characterization of alkali-silica reaction (ASR) gel in cement-based materials,” *Materials Letters*, vol. 90, pp. 159–161, 2013.

[67] A. Hashemi, M. Horst, K. E. Kurtis, K. M. Donnell, and R. Zoughi, “Comparison of alkali–silica reaction gel behavior in mortar at microwave frequencies,” *IEEE Transactions on Instrumentation and Measurement*, vol. 64, no. 7, pp. 1907–1915, 2015.

[68] J. Pan, Y. Feng, J. Wang, Q. Sun, C. Zhang, and D. Owen, “Modeling of alkali-silica reaction in concrete: a review,” *Frontiers of Structural and Civil Engineering*, vol. 6, no. 1, pp. 1–18, 2012.

[69] C. Comi, P. Monteiro, and R. Pignatelli, “Chemical and mechanical damage in concrete due to swelling of alkali-silica gel,” *Blucher Mechanical Engineering Proceedings*, vol. 1, no. 1, pp. 503–514, 2012.

[70] T. Kim and J. Olek, “Chemical sequence and kinetics of alkali–silica reaction part ii. a thermodynamic model,” *Journal of the American Ceramic Society*, vol. 97, no. 7, pp. 2204–2212, 2014.

[71] L. Sanchez, S. Multon, A. Sellier, M. Cyr, B. Fournier, and M. Jolin, “Comparative study of a chemo–mechanical modeling for alkali silica reaction (asr) with experimental evidences,” *Construction and Building Materials*, vol. 72, pp. 301–315, 2014.

[72] H. Bouzabata, S. Multon, A. Sellier, and H. Houari, “Swellings due to alkali-silica reaction and delayed ettringite formation: Characterisation of expansion isotropy and effect of moisture conditions,” *Cement and Concrete Composites*, vol. 34, no. 3, pp. 349–356, 2012.

[73] T. Katayama, “ASR gel in concrete subject to freeze-thaw cycles-comparison between laboratory and field concretes from Newfoundland, Canada,” *Proceedings of the 13th ICAAR*, pp. 174–183, 2008.

[74] S. Math, “Effect of selected parameters on aggregate reactivity in accelerated mortar bar test method: Aggregate size & deicers,” Master’s thesis, Department of Civil Engineering, Clemson University, 2011.

[75] N. Ghafoori and M. Islam, “Time series analysis for prediction of ASR-induced expansions,” *Construction and Building Materials*, vol. 49, pp. 194–200, 2013.

[76] C. W. Hargis, M. C. Juenger, and P. J. Monteiro, “Aggregate passivation: lithium hydroxide aggregate treatment to suppress alkali-silica reaction,” *ACI Materials Journal*, vol. 110, no. 5, p. 567, 2013.